

AN INVESTIGATION OF COMPACTED GRAPHITE IRON PRODUCTION BY  
MEANS OF THERMAL ANALYSIS TECHNIQUE AND OTHER PROCESS  
CONTROL WINDOWS

A THESIS SUBMITTED TO  
THE GRADUATE SCHOOL OF NATURAL AND APPLIED SCIENCES  
OF  
MIDDLE EAST TECHNICAL UNIVERSITY

BY

OMAR EL-MABROUK

IN PARTIAL FULFILLMENT OF THE REQUIREMENTS  
FOR  
THE DEGREE OF DOCTOR OF PHILOSOPHY  
IN  
METALLURGICAL AND MATERIAL ENGINEERING

JANUARY 2007

Approval of the Graduate School of Natural and Applied Sciences

---

Prof. Dr. Canan Özgen  
Director

I certify that this thesis satisfies all the requirements as a thesis for the degree of Doctor of Philosophy.

---

Prof. Dr. Tayfur Öztürk  
Head of Department

This is to certify that we have read this thesis and that in our opinion it is fully adequate, in scope and quality, as a thesis for the degree of Doctor of Philosophy.

---

Prof. Dr. Ali Kalkanlı  
Supervisor

Examining Committee Members

Prof. Dr. Bilgin Kaftanoğlu	(METU, ME)	_____
Prof. Dr. Ali Kalkanlı	(METU, METE)	_____
Prof. Dr. Haluk Atala	(METU, METE)	_____
Prof. Dr. Ekrem Selçuk	(METU, METE)	_____
Prof. Dr. Tamer Özdemir	(Gazi Univ.,ME)	_____

I hereby declare that all information in this document has been obtained and presented in accordance with academic rules and ethical conduct. I also declare that, as required by these rules and conduct, I have fully cited and referenced all material and results that are not original to this work.

Name, Last name: Omar ELMABROUK

Signature:

## **ABSTRACT**

### **AN INVESTIGATION OF COMPACTED GRAPHITE IRON PRODUCTION BY MEANS OF THERMAL ANALYSIS TECHNIQUE AND OTHER PROCESS CONTROL WINDOWS**

El-mabrouk, Omar

PhD, Metallurgical and Material Engineering Department

Supervisor: Prof. Dr. Ali Kalkanlı

January 2007, 123 pages

Compacted graphite irons have been proved valuable in many applications such as exhaust manifolds, hydraulic valves, and diesel engine blocks, the process of producing compacted graphite irons is not a straight forward process because of its narrow processing windows and its high sensitivity to the section thickness, treatment reaction time, pouring temperatures and charge composition.

In this thesis, compacted graphite was produced with minimum variations through all section thickness and the effect of Mg/S ratio, section thickness, and treatment agents on the graphite morphology, electrical resistivity property and fracture strength at high temperatures was investigated.

The range of Mg/S ratio and the section thickness was from 2/3 to 7/1 and 5 mm to 40 mm respectively. FeSiMg and FeSiMg cermish metal were used as a treatment agent.

Optical metallographic method was implemented to investigate the graphite

morphology change. For being a distinguishable characteristic for compacted graphite iron over ductile iron, thermal conductivity changes at high temperatures ranging from room temperature to 500 °C was examined by a suitable electrical setup in the manner of electrical conductivity changes by measuring the electrical resistance.

On the other hand, due to the higher values of mechanical properties of compacted graphite iron over those of gray iron, tensile strength was also examined by means of tensile test.

The relation between the compacted graphite shape and the alloy properties such as fracture strength and thermal conductivity was investigated. The most important controlling parameters to produce compacted graphite are Mg/S ratio and oxygen activity. The relation between these parameters with both fracture strength and thermal conductivity was established by means of multiple regression analysis technique.

**Keywords:** Compacted graphite iron (CGI), Mg/S ratio, oxygen activity, thermal conductivity, tensile strength, regression analysis .

## ÖZ

### KOMPAKT GRAFİT DÖKME DEMİR ÜRETİMİNİN TERMAL ANALİZ TEKNİĞİ VE DİĞER SÜREÇ KONTROL PENCERELERİ KULLANILARAK İNCELENMESİ

Omar, Elmabrouk

Doktora, Metalurji ve Malzeme Mühendisliği

Tez Yöneticisi: Prof. Dr. Ali Kalkanlı

Ocak 2007, 123 sayfa

Kompakt grafitli dökme demir egzoz manifoldu, hidrolik vanalar ve dizel motor blokları gibi bir çok endüstriyel uygulamada kullanılmaktadır. Üretiminde parça kesit kalınlığı, işlem süreleri, döküm sıcaklığı ve alaşım kompozisyonu gibi pek çok parametrenin gözönüne alınmasını gerektiren kompakt grafitli dökme demirlerin üretim işlemlerindeki aralıkları da çok dardır.

Bu tezin amacı kompakt grafitli dökme demir yapısını üretilen parçanın bütün kesitlerinde çıkartacak üretim parametrelerini belirlemek ve Mg/S oranı, kesit kalınlığı ve yapılan işlem türlerinin oluşan grafit morfolijisi, malzemenin elektriksel direnci ve mukavemetine etkilerini incelemektir.

2/3 ve 7/1 aralığında Mg/S oranına sahip numuneler 5 mm ila 40 mm arasındaki kesitlerde FeSiMg ve FeSiMg cermish metal ile işlem yapılan malzemeler incelenmiştir.

Grafit morfolojisinde meydana gelen değişimler metallografik yöntemlerle incelenmiştir. Kompakt grafitli dökme demir ve küresel grafitli dökme demiri ayırtedebilmek maksadıyla malzemenin elektrik direncini ölçerek elektrik iletkenliği üzerinden ısı iletkenliğindeki değişimleri izleyebilen bir deney sistemi kullanılmıştır.

Diğer bir yandan, kompakt grafitli dökme demirin gri dökme demire kıyasla daha yüksek mukavemete sahip olması nedeniyle yapılan işlemlerin mekanik özelliklere etkisi çekme testiyle incelenmiştir.

Mg/S oranı ve oksijen aktivitesi kompakt grafit üretimi için önemli parameterlerdir . Ayrıca aşırı soğuma gibi en önemli üretim değişkenleriyle kompakt grafit yüzdesini ilişkilendirebilmek için çoklu regresyon analiz yöntemi kullanılarak denklemler çıkartılmaya çalışılmıştır.

Anahtar Kelimeler: Kompakt grafit dökme demir(CGI), Mg/S oranı, oksijen aktivitesi, ısıl iletkenlik, kırılma dayancı, regresyon analizi

To my parents,  
who always support me in all aspects of my life  
to my wife  
for her patience and support in my study  
to my children  
Mustafa, Tesneem and Abdulraoof



## **ACKNOWLEDGEMENTS**

I would like to express my sincerest thanks to Prof. Dr. Ali Kalkanlı, my advisor for his guidance, support and valuable contributions throughout the preparations for this thesis.

My sincere appreciation also extends to Prof. Dr. Ekrem Selçuk for his insightful comments and suggestions.

The technical support provided by Mr Haluk Güldür from Heraeus Elctro-Nite in Türkiye is gratefully acknowledged.

I am grateful to my friends in Middle East Technical University for all the support they gave me throughout my study.

I express my deepest gratitude to my parents, my father Mustafa and my mother Asha for their encouragements throughout my education life, and to my wife Enas for her support and effort, and my children for their patience during my study. Their love, care and encouragement has given me a great inner strength to success. This work is dedicated to them.

The Libyan secretariat of higher education is highly appreciated for its financial support during my study period.

## TABLE OF CONTENTS

ABSTRACT .....	iv
ÖZ .....	vi
DEDICATION .....	viii
ACKNOWLEDGEMENTS .....	ix
TABLE OF CONTENTS .....	x
LIST OF FIGURES .....	xii
LIST OF TABLES .....	xv
CHAPTER	
<b>1. INTRODUCTION</b> .....	1
1.1 Casting Applications .....	4
1.2 Objective of the Study .....	4
<b>2. LITERATURE REVIEW</b> .....	6
2.1 Production of Compacted Graphite Iron .....	6
2.2 Graphite Morphology and Growth .....	8
2.3 Thermodynamic Considerations of Cast Irons .....	21
2.4 Overview of Thermal Analysis .....	23
2.5 Tensile Property of Compacted Graphite Iron .....	25
2.6 Thermal Conductivity .....	25
2.7 Multiple Regression Analysis .....	27
<b>3. EXPERIMENTAL PROCEDURE</b> .....	28
3.1 Work Plan .....	28
3.1.1 Effect of Treatment Agents .....	28
3.1.2 Effect of Mg/S Ratio .....	28
3.1.3 Effect of Section Thickness .....	29

3.1.4 Effect of Oxygen Activity .....	29
3.1.5 Thermal Analysis .....	29
3.2.Characterization of Casting Alloys Produced .....	29
3.2.1 Metallographic Examination.....	30
3.2.2 Tensile Testing. ....	30
3.2.3 Electrical and Thermal Conductivity Measurements.....	30
3.3 Regression Analysis .....	30
3.4 Charge Calculation .....	33
3.5 Melting Procedure .....	34
3.6 Metallographic Examinations .....	35
3.6.1 Sample Preparation and optical Microscopy Studies.....	35
3.6.2 Image Analyzer Study .....	35
3.6.3 Chemical Analysis .....	36
3.7 Oxygen Activity Measurements.....	37
3.8 Thermal Analysis .....	41
3.9 Tensile Strength Measurements .....	42
3.10 Thermal Conductivity Measurements .....	42
3.11 Muliple Regression Analysis .....	47
<b>4. EXPERIMENTAL RESULTS .....</b>	<b>49</b>
4.1 The Effect of Mg/S ratio and the Cooling Rate on the Microstructures of Heats Treated with FeSiMg-Cremish Metal or with FeSiMg .....	49
4.2 The Effect of Oxygen Activity on the Microstructures of Heats Treated with FeSiMg-Cremish Metal or with FeSiMg .....	76
4.3 The Relationship between Microstructure and Solidification Cooling Curves ..	82
4.4 The Effect of Graphite Morphology and Iron Matrix on the the fracture Tensile Strength .....	95
4.5 Electrical Resistance and Thermal Conductivity Measurements at Evated Temperatures.....	98
4.6 Regression Analysis.....	103
4.6.1 Multiple Regression Model for Fracture Strength .....	104
4.6.2 Multiple Regression Analysis for Thermal Conductivity .....	105
<b>5. CONCLUSIONS AND SCOPE OF FUTURE WORK .....</b>	<b>107</b>

5.1 Conclusion .....	107
5.2 Scope of Future Work .....	106
<b>REFERENCES</b> .....	111

## LIST OF FIGURES

### FIGURES

1.1 Phases in Fe-Fe <sub>3</sub> C system .	1
2.1. Classification of Different Methods for Producing Compacted Graphite Irons .	8
2.2 Graphite Structures and Growth .	10
2.3 The Hexagonal Graphite Crystal Structures in Cast Iron. The Relationship of the Graphite Structure to the Graphite Structure, the Spheroidal and Flake Growth Direction .	11
3.1 Step Block with 5, 10, 20 and 40 mm Thick Steps.	32
3.2 Dimensions of the Cast Tensile Test Bar .	32
3.3 Plunger Method Used for CG Iron Production .	38
3.4 METASERV Universal Polishers .	39
3.5 Optical Microscope. .	39
3.6 CLEMEX Image Analyzer System. .	40
3.7 OBFL Spectrometer. .	40
3.8 Heraeus Electro-Nite Celox Foundry Device with Vibrating Lance. .	41
3.9 Schematic of Cast Iron Cooling Curve. .	42
3.10 ALSA Universal Testing Machine. .	43
3.11 The Dimension of the Electrical Resistivity Specimen. .	44
3.12 The Setup Used for Electrical Resistance Measurements. .	45
3.13 The Sketch of the Specimen Fixing Mechanism Used in High Temperature Resistivity Measurements. .	46
4.1 Microstructure of Specimen 1Ad, Magnification ×100, Unetched. .	52

4.2 Microstructure of Specimen 1Ae, Magnification $\times 100$ , Unetched.....	52
4.3 Microstructure of Specimen 1Af, Magnification $\times 100$ , Unetched. ....	53
4.4 Microstructure of Specimen 1Ag, Magnification $\times 100$ , Unetched.....	53
4.5 Microstructure of Specimen 4Ad, Magnification $\times 100$ , Unetched .....	54
4.6 Microstructure of Specimen 4Ae, Magnification $\times 100$ , Unetched.....	54
4.7 Microstructure of Specimen 4Af, Magnification $\times 100$ , Unetched .....	55
4.8 Microstructure of Specimen 4Ag, Magnification $\times 100$ , Unetched .....	55
4.9 Microstructure of Specimen 4Bd, Magnification $\times 500$ , Unetched.....	56
4.10 Microstructure of Specimen 4Be, Magnification $\times 500$ , Unetched. ....	56
4.11 Microstructure of Specimen 4Bf, Magnification $\times 500$ , Unetched.....	57
4.12 Microstructure of Specimen 4Bg, Magnification $\times 500$ , Unetched.....	57
4.13 Microstructure of Specimen 5Ad, Magnification $\times 100$ , Unetched.....	58
4.14 Microstructure of Specimen 5Ae, Magnification $\times 100$ , Unetched.....	58
4.15 Microstructure of Specimen 5Af, Magnification $\times 100$ , Unetched. ....	59
4.16 Microstructure of Specimen 5Ag, Magnification $\times 100$ , Unetched.....	59
4.17 Microstructure of Specimen 5Bd, Magnification $\times 100$ , Unetched.....	65
4.18 Microstructure of Specimen 5Be, Magnification $\times 100$ , Unetched .....	65
4.19 Microstructure of Specimen 5Bf, Magnification $\times 100$ , Unetched.....	66
4.20 Microstructure of Specimen 5Bg, Magnification $\times 100$ , Unetched.....	66
4.21 Microstructure of Specimen 6Bf, Magnification $\times 100$ and 9 min treatment time, 2% Nital etch.....	67
4.22 Microstructure of Specimen 6Bf, Magnification $\times 100$ and 14 min treatment time, 2% Nital etch.....	67
4.23 Microstructure of Specimen 6Bd, Magnification $\times 100$ , Unetched.....	68
4.24 Microstructure of Specimen 6Be, Magnification $\times 100$ , Unetched. ....	68
4.25 Microstructure of Specimen 6Bf, Magnification $\times 100$ , Unetched.....	69
4.26 Microstructure of Specimen 6Bg, Magnification $\times 100$ , Unetched.....	69

4.27 Microstructure of Specimen 7Bd, Magnification $\times 100$ , Unetched.....	70
4.28 Microstructure of Specimen 7Be, Magnification $\times 100$ , Unetched.....	70
4.29 Microstructure of Specimen 7Bf, Magnification $\times 100$ , Unetched.....	71
4.30 Microstructure of Specimen 7Bg, Magnification $\times 100$ , Unetched.....	71
4.31 Microstructure of Specimen 8Ad, Magnification $\times 100$ , Unetched.....	72
4.32 Microstructure of Specimen 8Ae, Magnification $\times 100$ , Unetched.....	72
4.33 Microstructure of Specimen 8Af, Magnification $\times 100$ , Unetched.....	73
4.34 Microstructure of Specimen 8Ag, Magnification $\times 100$ , Unetched.....	73
4.35 Microstructure of Specimen 8Bd, Magnification $\times 100$ , Unetched.....	74
4.36 Microstructure of Specimen 8Be, Magnification $\times 100$ , Unetched.....	74
4.37 Microstructure of Specimen 8Bf, Magnification $\times 100$ , Unetched.....	75
4.38 Microstructure of Specimen 8Bg, Magnification $\times 100$ , Unetched.....	75
4.39 The Effect of the Type of Treatment Material on the Oxygen Activity .....	80
4.40 Cooling Curve of Heat 1A .....	85
4.41 Cooling Curve of Heat 4A .....	86
4.42 Cooling Curve of Heat 4B.....	86
4.43 Cooling Curve of Heat 5B.....	87
4.44 Cooling Curve of 5B Heat.....	87
4.45 Cooling Curve of Heat 6B with 9 Min. Treatment Time.....	88
4.46 Cooling Curve of Heat 6B with 14 Min. Treatment Time.....	88
4.47 Cooling Curve of Heat 6A .....	89
4.48 Cooling Curve of Heat 7B.....	92
4.49 Cooling Curve of Heat 8A .....	92
4.50 Cooling Curve of Heat 8B.....	93
4.51 The Effect Mg/S Ratio of Group A Treatment Material on the Recalescence ..	93
4.52 The Effect Mg/S Ratio of Group B Treatment Material on the Recalescence...	94

4.53 The Relationship between the Mg/S Ratio and the Tensile Strength for Each Type of Treatment Material .....	97
4.54 Variation of Thermal Conductivity of 4Ad, e, f and g with Temperature .	101
4.55 Variation of Thermal Conductivity of 6Ad, e, f and g with Temperature .	101
4.56 Variation of Thermal Conductivity of 8Ad, e, f and g with Temperature .	102



## LIST OF TABLES

### TABLES

1.1. Range of Composition for Typical Unalloyed Cast Irons.....	2
2.1. Maximum Permissible Amounts of Subversive Elements in Ductile Iron .....	17
2.2. Thermal Conductivity Values for Various Cast Irons .....	26
2.3. Results of Thermal Conductivity for Different Grades of Gray Iron .....	27
2.4 Results of Thermal Conductivity for Different Grades of Ductile Iron.....	27
3.1 Aimed Values of Carbon Equivalent, Total Carbon and Silicon .....	33
3.2 Calculated Values of Silicon, Mg/S Ratio and Copper.....	34
3.3 Example for a Charge Used in Experiments .....	34
3.4 Treatment Details .....	36
3.5 Descriptions of Codes .....	37
4.1 The Chemical Composition of Heat 1A.....	50
4.2 The Chemical Composition of Heat 4A.....	50
4.3 The Chemical Composition of Heat 4B.....	51
4.4 The Chemical Composition of Heat 5A.....	60
4.5 The Chemical Composition of Heat 5B.....	60
4.6 The Chemical Composition of Heat 6B .....	61
4.7 The Chemical Composition of Heat 6A.....	62
4.8 The Chemical Composition of Heat 7B.....	62
4.9 The Chemical Composition of Heat 8A.....	63
4.10 The Chemical Composition of Heat 8B.....	64

4.11 Heat Code, Recalescence, Undercooling and Graphite Form .....	94
4.12 Tensile Test and Matrix Structures Results .....	97
4.13 The Electrical Resistance of 4Ad, e, f, and g .....	99
4.14 The Electrical Resistance of 6Ad, e, f, and g .....	100
4.15 The Electrical Resistance of 8Ad, e, f, and g .....	100
4.16 Thermal Conductivity, Tensile Strength, Mg/S Ratio, Undercooling and Oxygen Activity Required to Produce Compacted Graphite Cast Iron .....	103
4.17 Linear Regression Parameters Estimated for Fracture Strength .....	104
4.18 The Predicted Fracture Strength Obtained from the Estimated Parameters ...	105
4.19 Linear Regression Parameters Estimated for Thermal Conductivity .....	106
4.20 The Predicted Thermal Conductivity Obtained from the Estimated Parameters .....	106

## CHAPTER 1

### INTRODUCTION

Cast irons are the ferrous alloys with greater than 2.14 wt % carbon, but typically contain 3-4.5 wt % of C as well as other alloying elements, such as silicon (~3 wt. %) which leads to decomposition of the carbide into iron and graphite as shown in Figure 1.1

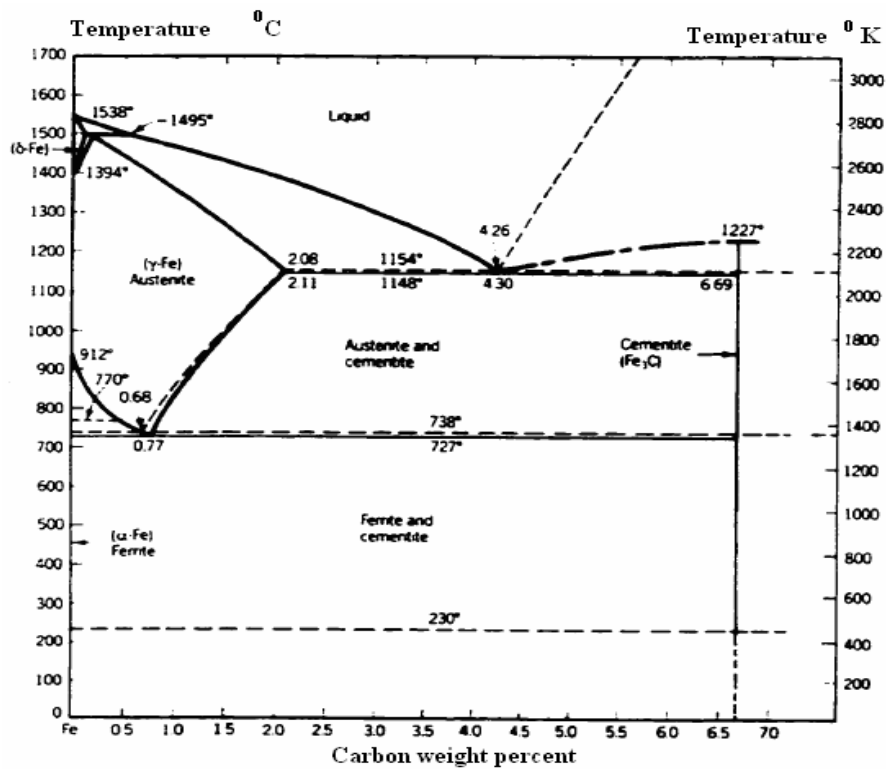


Figure 1.1 Phases in Fe-Fe<sub>3</sub>C system

These alloys have relatively low melting points (1150-1300°C), do not form undesirable surface films when poured, and undergo moderate shrinkage during solidification. Thus, it can be easily melted and amenable to casting. The basic types of cast irons are gray iron, white iron, malleable iron, and compacted graphite iron (CGI).

The various types of cast iron cannot be designated by chemical composition because of similarities between types. Table 1.1 lists typical composition ranges for the most frequently determined elements in the five generic types of cast iron.

Table 1.1. Range of compositions for typical unalloyed cast Irons

	Percent (%)				
Type of Iron	Carbon	Silicon	Manganese	Sulfur	Phosphorous
White	1.8-3.6	0.5-1.9	0.25-0.8	0.06-0.2	0.06-0.2
Malleable (Cast White)	2.2-2.9	0.9-1.9	0.15-1.2	0.02-0.2	0.02-0.2
Gray	2.5-4.0	1.0-3.0	0.2-1.0	0.02-0.25	0.02-1.0
Ductile	3.0-4.0	1.8-2.8	0.1-1.0	0.01-0.03	0.01-0.1
Compacted	2.5-4.0	1.0-3.0	0.2-1.0	0.01-0.03	0.01-0.1

White cast irons are used where wear resistance is most important and surface does

not require ductility, such as extrusion nozzles. Some typical application of ductile cast iron are agricultural – tractor and implement parts, automotive and diesel – crankshafts. Malleable cast iron has similar applications of ductile iron; gray cast iron is used in brake drums, clutch plates. Compacted graphite cast iron is a new type of cast iron that has been added recently, this type of cast iron becomes a suitable material for all the application in which both the high strength and high thermal conductivity are the desired goal and there has been an increasing interest in CG irons in recent years due to the following factors:

- 1 It is easy to optimize the properties of CG irons, and there is more effective use of raw materials than that of ductile irons in production of CG iron (104).
- 2 Due to its high carbon equivalent, CG iron has excellent fluidity (104).
- 3 Solidification shrinkage is low so casting can be produced directly from gray iron with only minor modifications (104).
- 4 As compared to ductile iron there is a significant improvement in the casting yield (clean casting weight / poured weight) with CG iron (104).
- 5 The properties of CG iron as it will be illustrated in next chapter were found to be intermediate between gray and ductile irons (104).

## **1.1 Casting Applications**

Examples that can be given for CG castings are bed plates for large diesel engines, crank cases, gearbox, turbocharger housings, and connecting rods, bearing brakes, pulley for truck servo drivers, sprocket wheels and exhaust manifolds. Because the thermal conductivity is higher than that of ductile irons, CG iron is preferred for castings operating at elevated temperatures and / or under thermal fatigue conditions. An application includes ingot moulds, crank cases, and cylinder heads, exhaust manifolds and break disks.

## **1.2 Objective of the Study**

The overall goal of this project is to determine and to demonstrate the effect of magnesium to sulfur ratio on the compacted graphite morphology and specify an appropriate treatment agent for the production of compacted graphite cast iron for the given section thickness, taking into consideration both the oxygen activity values and thermal analysis as process control tools.

In order to achieve this goal, a plan was put forward on the investigation of the effect of treatment agents, the effect of Mg/S ratio, the effect of section thickness, the effect of oxygen activity on the production of compacted graphite iron. Cooling curves were analyzed; the characterization of the cast iron alloys was done by means of metallographic examination combined with the tensile testing and thermal conductivity measurements. Multiple regression analysis was implemented to

correlate the main features of compacted graphite cast iron, tensile strength and thermal conductivity, with main parameters affecting its production.

## **CHAPTER2**

### **LITERATURE REVIEW**

#### **2.1 Production of Compacted Graphite Iron**

The great limitation in the application of CG irons is due to the need for an exact graphite morphology control upon processing. General specifications tolerate at most 10-20% of nodular graphite particles and no flaky graphite in commercial CG irons, R. Elliott [1]. Cornell and Loper [2] provided a detailed analysis of the CE range for section sizes from 1.27-12.7 mm.

In addition to carbon and silicon, magnesium content should be monitored conscientiously since residual contents out of the 0.005% - 0.008% range could result in an excessively flaky microstructure for the lower Mg values or in an exceedingly nodular one, for higher Mg levels. In this case, the use of lanthanides combined with magnesium can compensate the deficiency in graphite morphology, Cornell and Loper [2, 103].

Several methods have been experimentally implemented to produce CGI. For instance, as reported by Monroe and Bates [3], it is possible to desulfurize the base metal to attain very low values of sulfur and then allow for a rapid solidification.



The addition of controlled amounts of spheroidizing elements such as Mg or Ce can also be used. Finally treating the molten metal with both spheroidizing and anti-spheroidizing elements mainly Ti, at the same time provides optimum results in many applications [103].

Indeed, this appears to be most reliable CGI production method with reliable results. However, one important factor impedes the general application of this treatment: Titanium has a strong carbide, and nitrocarbide formation tendency. TiC and complex Ti nitrocarbides are very hard phases that diminish machining tool lifetime. Whenever possible such phases should be avoided in CGI parts where exacting or heavy machining processes are required.

Nofal et al compiled all possible alternatives for the production of compacted graphite [4,103]. In Figure 2.1 the corresponding classification is shown. From this categorizing it becomes apparent that most of alternatives deal somehow with the addition of nodularizing agents such as magnesium, cerium and rare earths (RE). [103].

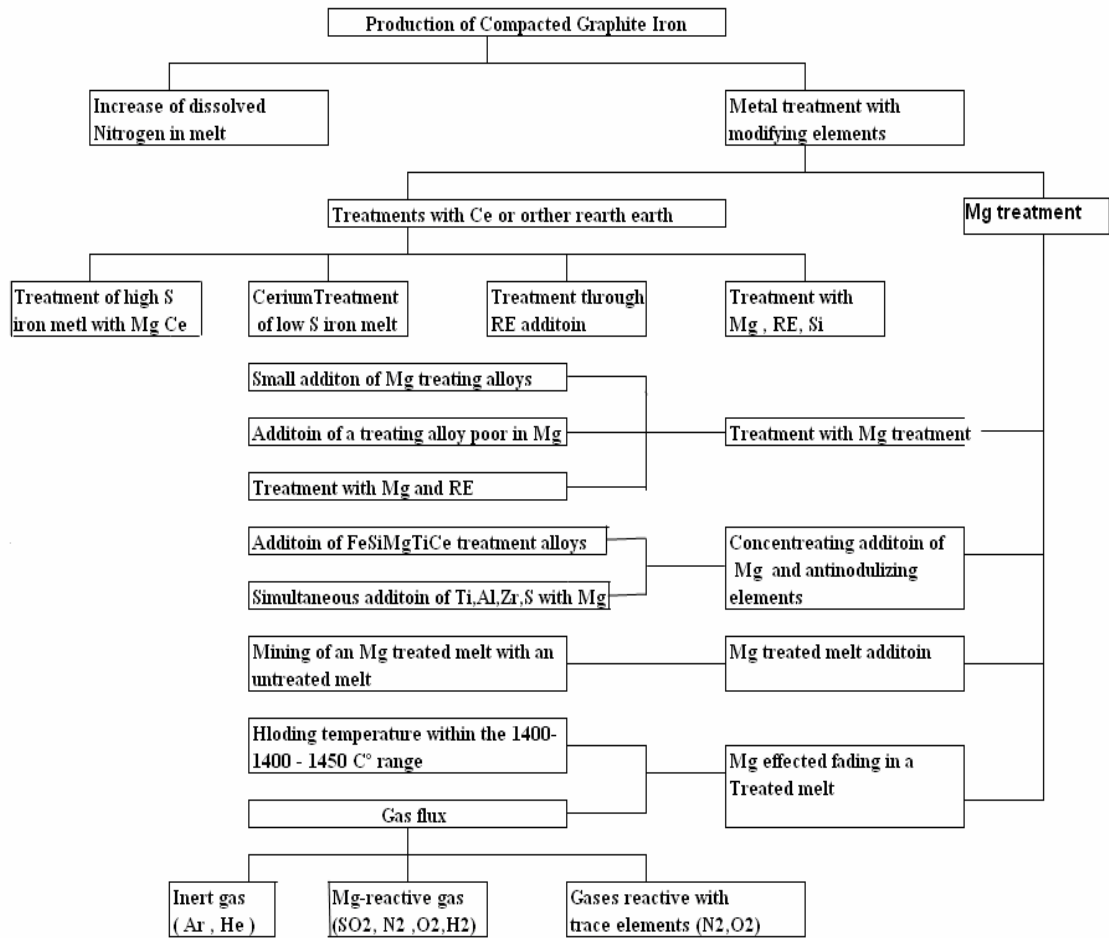


Figure.2.1. Classification of different methods for producing compacted graphite irons, as indicated by Nofal, et al. (4, 103).

## 2.2 Graphite Morphology and Growth

Cast irons are eutectic or near-eutectic iron-carbon-silicon alloys that contain small amounts of sulfur, phosphorus, oxygen, and nitrogen (13, 15, 16, 100). The microstructure of these cast irons is comprised primarily of graphite particles in an iron rich matrix.

Several different graphite morphologies can occur (13, 15-21,100), some of the more common of which were presented in Figure 2.2 are listed below:

1. Type A flake
2. Type B flake (rosette)
3. Type C flake (undercooled)
4. Compacted (quasiflake)
5. Vermicular (wormy)
6. Spheroidal (nodular)

During the solidification of cast iron melts, graphite is nucleated by potent substrates such as graphite particles (22-25, 100) and sulfides (15, 26-29,100), as the melt undercools to temperatures beneath the eutectic temperature. The subsequent growth of the graphite determines the graphite morphology and is influenced by several interrelated factors. These include, the crystal structure of graphite (30-36,100), whether the graphite crystal planes exhibit a faceted or nonfaceted interface with the liquid iron and grow as a divorced or coupled eutectic (39-44,100), the amount the melt is undercooled (20,100) and the composition of the melt (21,100).



a) Type A flake graphite



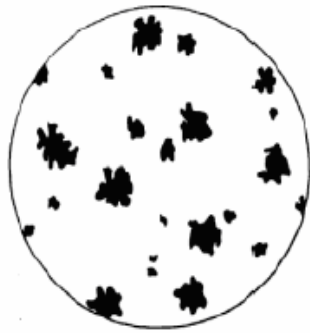
b) type B flake graphite



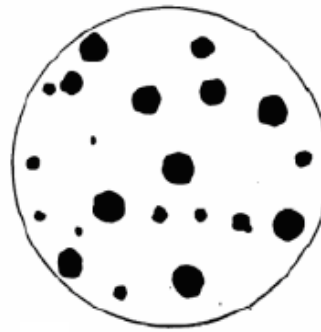
c) Type C flake graphite



d) Compacted graphite



e) Vermicular graphite



f) Spheroidal graphite

Figure. 2.2. Graphite structures and growth

The hexagonal crystal structure of graphite is illustrated in Figure 2.3 (14,100). It is

comprised of close-packed, high-energy basal planes, in which the carbon atoms are strongly bonded, and low-energy prism planes, in which the carbon atoms are weakly bonded (14, 33,100).

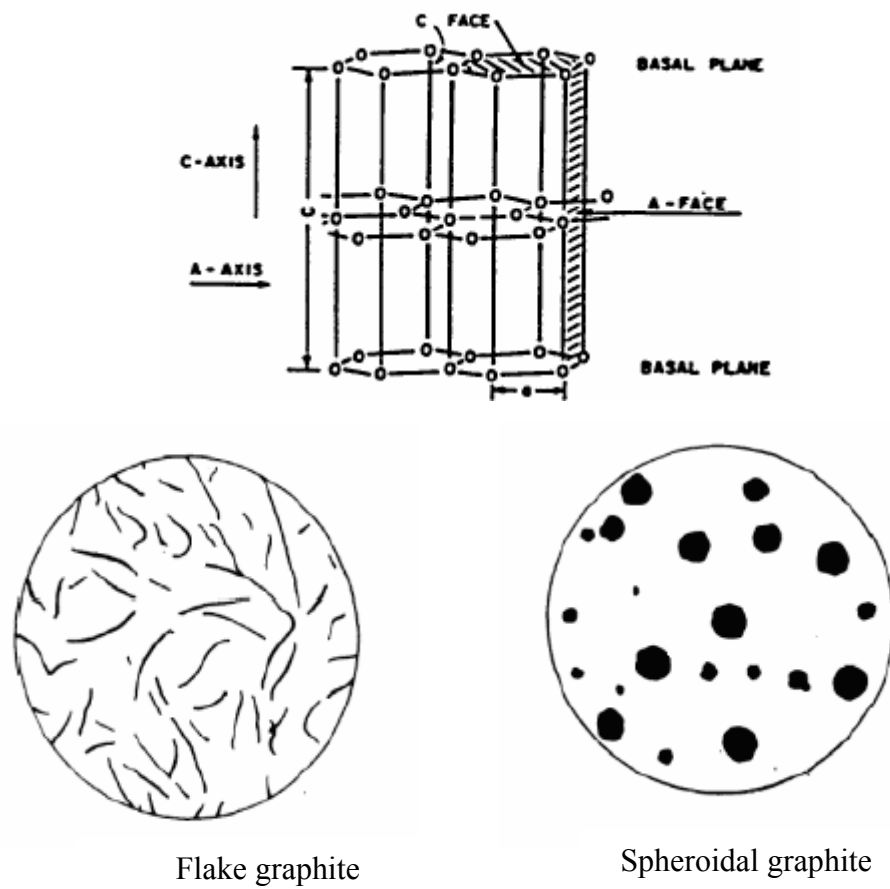


Figure. 2.3. The hexagonal graphite crystal structures in cast iron and the formation of the spheroidal and flake growth direction (100).

Spheroidal graphite which forms in ductile iron grows primarily along the c-axis by the addition of carbon atoms to the basal planes (14,15,18,19,33,37,39,100); a-axis growth by the addition of carbon atoms to the prism planes predominates for the flake graphite that forms in gray cast iron (14,15,18,20,37,39,40,100) as shown in Figure2.3.

Graphite flakes are comprised of long sheets of crystals with basal planes oriented along the top and bottom of each sheet (14, 15,100). As carbon atoms are added to the prism planes of graphite crystals, the graphite crystal twists and branches to form the characteristic graphite flake structure shown in Figure2.2. These flakes are interconnected within the eutectic cells that grow from separate nucleation events, with the graphite within each cell being a single crystal (14, 15, 25, 41, 42, 100). Graphite spheroids consist of several columnar graphite crystals radiating from the center of nucleation (18,100). These crystals grow by the addition of carbon atoms to the basal planes which form the surface of the spheroids. (100).

The amount of undercooling below the eutectic temperature which occurs prior to the onset of solidification also greatly influences the graphite shape (100). The greater the cooling rate and the poorer the state of nucleation of the melt, the greater will be the undercooling (14-16, 20, 41, 43,100). The graphite morphologies are listed above in order of the increasing undercooling associated with the formation of each type of graphite. Thus, as the cooling rate and the undercooling are increased for a hypo-eutectic cast iron, a transition in graphite structure from Type A to Type B to Type C graphite will occur (14, 15, 20, 41, 44, 47, 100). Further increases in

cooling rate will cause the cast iron to solidify as the metastable iron carbide-austenite eutectic, and the resultant white iron structure will contain massive iron carbides (13,100).

The flake graphite morphologies grow during coupled eutectic solidification (14, 33, 46, 100). Flake graphite is reported to grow by the addition of carbon atoms to the prism face of the graphite crystal because sulfur and oxygen are adsorbed on the graphite prism face and cause it to act as an atomically rough, nonfaceted interface with the liquid iron (38,100). This reduces the undercooling needed for growth and produces coupled eutectic growth in which graphite is the first phase to nucleate and is the leading phase which grows out into the melt. Subsequently, the austenite nucleates from the melt and grows cooperatively with the graphite (38, 46,100). Cooperative growth with graphite growing on a nonfaceted interface with only small undercooling is promoted by adsorption of oxygen and sulfur from the melt onto the graphite (47,100).

Spheroidal graphite is produced in commercial ductile iron by the addition of elements which deoxidize and desulfurize the melt (13-17, 33,100). It has also been produced experimentally in high purity, very low sulfur content, iron-carbon-silicon alloys which were solidified rapidly (41, 48-51,100). Sulfur and oxygen are removed from the prism face by the addition of nodularizing elements. This results in changing the interface between the graphite crystal and the liquid iron to an atomically smooth or faceted prism face, causing spiral growth to occur on the close-packed, basal plane. This produces a spheroidal graphite structure and results in slower growth with more undercooling. The undercooling occurs because the

basal plane has a faceted interface with liquid iron; although graphite growth is enhanced compared to secondary nucleation conditions by defect controlled spiral growth (38,100).

The graphite spheroids form in a divorced eutectic reaction and are isolated in the melt during solidification (18, 41, 51-53,100). It forms in ductile iron that is slowly cooled or slightly under-treated with the additions used to deoxidize and desulfurize the melt (17, 54-58,100).

Compacted graphite is produced commercially by the addition to the melt of subversive trace elements, such as titanium, in combination with elements which deoxidize and desulfurize the melt (118,119,124). It has also formed in undertreated ductile iron (59, 60) and from high nitrogen gray iron melts (61-63). Compacted graphite forms at an undercooling intermediate between that of flake and spheroidal graphite (21, 64). As the cooling rate and the undercooling (20), or the amount of addition to deoxidize and desulfurize the melt (17, 21) is increased, a transition in graphite morphology from compacted to vermicular to spheroidal will take place. Further increases in undercooling will result in solidification by the metastable iron carbide- austenite eutectic (100). Currently, the growth habit of compacted graphite is not established. Although it is not universally accepted (20, 56, 100), it has been proposed (66,100) that the compacted graphite structure grows primarily in the a-axis direction by the attachment of carbon atoms to the prism faces. Basal plane growth occurs simultaneously, but at a slower velocity, accounting for the rounded, blunted flake ends. It has also been suggested that



compacted graphite initially grows by flake-like growth in which carbon atoms are added to the prism plane, but the growth then changes to spiral, defect controlled growth which produces the blunted, rounded shape characteristic of compacted graphite (67,100). The interconnected graphite morphology (66,100) coupled with its intermediate undercooling, suggests that compacted graphite forms by a type of coupled eutectic growth. Results of a recent investigation have indicated that compacted graphite solidified as a weakly cooperative eutectic (67,100).

As previously indicated, graphite growth is greatly influenced by the presence of small amounts of certain elements in the melt. Free sulfur and oxygen adsorb on the prism face and cause the formation of a nonfaceted interface with the liquid iron (38,100). The prism face is then highly mobile and carbon atoms are primarily added to this face. This promotes coupled eutectic growth and the formation of graphite flakes (33, 38, 47, 68, 69,100). The removal of the free oxygen and sulfur by the addition of nodularizing elements causes the prism face to be faceted. Growth then proceeds by the addition of carbon atoms to the closer packed, faceted basal plane, which is enhanced by defect controlled spiral growth (38,100). Elements other than oxygen and sulfur may also have a subversive effect on graphite growth from magnesium treated melts and can promote the formation of graphite shapes other than spheroids. The subversive effect of these elements, which include sulfur (21,39,52,74,75,100), oxygen (15,33,46,68,69,100), titanium (21,43,70,71,100), arsenic (21,33,44,100), tin (21,33,70,71,100), antimony (15,21,42,44,70,71,100), lead (15, 21,33,44,70,71,100), bismuth (21,33, 44,70,100), zirconium (33, 71,100), tellerium (33,44,100), and aluminium (21,33,70,71,100) are

known to increase with atomic weight, binding energy to graphite, and concentration, and to decrease as the solubility of the element in iron increases (33,100). The maximum permissible amounts of the subversive elements in ductile iron have been proposed by various investigators and are listed in Table 2.1 (33,100).

Table 2.1 Maximum permissible amounts of subversive elements treated with Mg-Ce additions and with Mg additions in ductile iron (39,100)

Elements	Treated with Mg-Ce additions (wt %)	Treated with Mg additions (wt %)	
Bi	0.003	0.005	0.006-0.01
Pb	0.009	0.010	0.014
Sb	0.026	0.010	0.015
Te	-	0.050	-
Sn	0.130	-	-
As	0.080	-	-
Se	-	0.050	-
Ti	0.040	0.080	0.150
Cu	-	0.400	-
Al	0.300	-	0.500

The following equation attempts to quantify the influence of the subversive elements on the graphite structure in magnesium treated melts and an alloy parameter  $K_2$  is defined as follows:

$$K_2 = \frac{4.4(\%Ti) + 2.0(\%As) + 2.3(Sn) + 5.0(\%Sb) + 2.90(\%Pb) + 3.70(\%Bi) + 1.6(\%Al)}{\%Mg} \quad (2.1)$$

The parameter  $K_2$  is above 47.5 for gray iron, below 8.5 for ductile iron, and intermediate value for compacted graphite iron (21,100). It is pointed out that the accuracy of this formula is limited because it does not include the influence of sulfur, oxygen, and cerium, the latter of which is important because it combines with subversive elements and removes them from solution in the melt (15, 46, 72, 100).

Subversive elements have been hypothesized to influence graphite growth either by concentrating at the solidification front and serving as a barrier to the diffusion of carbon atoms, or by modifying the kinetics of carbon atom attachment to the graphite faces (15, 33, 73, 74, 100).

Several reviews have been written (15, 33, 75, 76, 100) that summarize the hypotheses which attempt to rationalize the various graphite morphologies. These hypotheses can be divided into two categories: one based on thermodynamic considerations pertaining to the changes in surface/interfacial energy, and the other based on kinetic considerations pertaining to differences in the atom attachment kinetics on the different crystallographic faces. Among these theories are the following (100):

1. Graphite spheroids form as a result of an attempt to minimize the graphite-melt interfacial area (48,100).

2. Spheroid formation depends on the absence of certain surface-active elements which alter the relative interfacial energies of the crystallographic faces of graphite (77-83,100). Graphite, regardless of its morphology, grows by the addition of carbon atoms to the crystallographic plane with the lowest interfacial energy with the melt. Surface-active elements typically present in gray iron, such as sulfur and oxygen, provide prism planes with the lowest interfacial energy by being adsorbed onto them, and thereby, promote a-axis growth (79, 100).
3. A high surface tension of the melt is a necessary condition for spheroidal graphite formation (83, 84, 100). The high surface tension is attained by the removal of surface-active elements dissolved in the melt by chemical reactions with nodularizing elements such as magnesium.
4. Spheroidal graphite grows by the extension of basal planes by a screw dislocation mechanism. The adsorption of impurities at the steps of these dislocations promotes the extension of the prism planes, resulting in flake graphite (33, 47, 68, 69, 85-87, 100).
5. Sulfur and oxygen are adsorbed on the prism face of the graphite crystal and produce an atomically rough, highly mobile nonfaceted interface with liquid iron. Coupled eutectic growth and an interconnected flake structure is produced. Removal of sulfur and oxygen by nodularizing elements results in the formation of an atomically smooth, faceted prism face. Spiral defect controlled growth occurs on the closer packed basal planes and spheroidal graphite is produced (38, 100).

The first three hypotheses are thermodynamic arguments, while the fourth and fifth are based on kinetics. It has been shown (88, 100) that the thermodynamic arguments are not valid for graphite particles greater than one micron; the average graphite spheroid in ductile iron is ten microns in size. Therefore, these theories, if at all applicable, are probably operative only for graphite nodules less than one micron in diameter (100).

The hypo-theses based on atom attachment kinetics appear to have more validity. Crystal growth theory indicates that high energy, high index faces will grow the fastest initially (89, 100) and that the crystal will be bounded by the low index, low energy faces that grow by step sources. The particular growth mechanism that provides the maximum rate of decrease of free energy per unit volume will be the one preferred. A screw dislocation on the basal plane, apparently, provides the necessary requirements (38, 90, 100).

The presence of the screw dislocation increases the mobility of the faceted basal plane and carbon atoms are added preferentially to the basal plane in melts free of impurities such as sulfur and oxygen. Impurities promote the formation of a non-faceted prism plane; hence the growth rate of the graphite in the direction of the prism pole is substantially greater than that in the direction of the basal pole (100). The proposed interaction between the step sources and impurities are in substantial agreement with the fundamental knowledge of crystal defect-impurity interactions (91-97, 100), and are consistent with the large influence of trace elements in the melt on graphite morphology.

### 2.3 Thermodynamic Considerations of Cast Irons

The sulfur and oxygen dissolved in Fe-C-Si alloys promote the growth of flake graphite (47, 68, 69, 100, 104). The virtually complete removal of sulfur and oxygen by treatment with magnesium and rare-earth containing ferro-alloys produces spheroidal graphite. Thus, it is important to determine if excess sulfur and oxygen were present in the treated iron, or if the addition of magnesium and rare-earth elements neutralized the effect of the sulfur and oxygen by chemical combination to form oxides and sulfides (100, 104).

The thermodynamics of the reactions that form sulfides and oxides during treatment of molten iron with magnesium and rare-earths indicate that the rare-earth elements will react first to form an oxysulfide of the following composition:  $RE_2 O_2 S$ . Because the oxygen content of molten Fe-C-Si alloys is very low, approximately 0.0005 to 0.008%, the amount of  $RE_2 O_2 S$  that forms is insignificant. The next reaction product to form is a rare-earth sulfide. Several investigators have established that  $RE_2 S_2$  is the most stable sulfide formed in molten iron after treatment with rare-earths. If excess sulfur is still present, then the sulfur will react with magnesium to form MgS. Therefore, the following reaction sequence occurs (100, 104):



As previously indicated, the amount of  $\text{RE}_2\text{O}_3$  S formed is insignificant because of the low oxygen content present in Fe-C-Si alloys. Therefore, reactions two and three were used to determine the following equation for the excess sulfur,  $\Delta S$ :

$$\Delta S = \text{final \%S} - 0.34(\%\text{RE}) - 1.33(\%\text{Mg}) \quad 2.5$$

Two assumptions were made in determining the above formula for  $\Delta S$ : 1) The total rare-earth content of the iron was equal to twice the cerium content of the iron because the rare-earth content of most ferro-alloys is equal to twice the cerium content (72,100,104), and 2). The atomic weight of all the rare-earths is equal to 140, which is the atomic weight of cerium. This formula effectively normalizes the magnesium and rare-earth contents of the iron with respect to the sulfur content by considering the stoichiometry of the sulfides which form during treatment. A positive value of  $\Delta S$  signified the presence of excess sulfur, while a negative value of  $\Delta S$  denotes excess magnesium and/or rare-earth elements. It is pointed out; however, that free sulfur can exist despite a negative  $\Delta S$  value. This free sulfur is the amount that remains dissolved in the molten iron and is in equilibrium with the sulfides that have formed. The more negative the  $\Delta S$  value is, the further the reaction to form sulfides will be driven to completion, and the less free sulfur will exist in the melt. The free sulfur is important because it is free to influence the growth of graphite in cast iron melts. The excess sulfur,  $\Delta S$ , was used to determine the relationship among graphite structures, sulfur, magnesium, rare-earths and the denodularizing additions (100,104). It has been also concluded that the recommended range for oxygen activity for the three types of graphite iron, flake,



compacted and ductile iron are -220 to -130, -320 to -240 and -425 to -350 mV or respectively at eutectic temperature ranging from 1110 to 1160 °C which equal to 0.0058 to 0.0250, 0.0011 to 0.0042 and 0.0002 to 0.0007 ppm at 1160 °C (102).

## **2.4 Overview of Thermal Analysis**

In the production of cast iron, thermal analysis application has been instrumental in the prediction of microstructure characteristics, chemical composition and mechanical properties of cast iron, either gray or ductile. Thermal analysis ability to detect events associated with solidification characteristics of the iron has been largely utilized as an on-line quality control tool for cast iron foundries. While on the one hand the values of critical temperatures are generally accepted as an important quality control tool, M. D. Chaudhari et al [5], on the other hand the cooling curve shape is also applied to cast iron characterization on a more qualitative basis, Ryntz and Janovvak (6, 103).

In the last decade, statistically based models were developed not only to typify critical temperature dependence on chemical composition but also to predict mechanical properties, metal penetration, shrinkage, chill tendencies and eutectic cell count based on the iron chemistry, Levi et al (7). From the early works by Humphreys (8), nominally carbon, silicon and phosphorus effects on the arrest temperatures were studied by means of cooling curves. In that investigation, the liquidus temperature is correlated to a linear combination of carbon, silicon and phosphorus contents for hyper-, hypo- and eutectic alloys. Since then many authors

(9, 10, 11, 12) have developed different models in an attempt to interpret cooling curves based on statistical analysis of the correlation between critical temperatures, e.g. liquidus arrest temperatures, eutectic temperatures, etc. and the iron chemical composition. However, there is a major problem inherent to this method: unaccounted variables concerning production methods, charge materials, etc. result in models applicable only to particular foundries or even production lines. (103)

An additional obstacle is the lack of a standard thermal analysis method that would allow a *vis a vis* comparison among experiments in different foundries. Indeed, different thermocouple cup types produce different sets of critical temperatures due to their dissimilar heat conduction properties. As a consequence, a model elaborated with a given cup type may not be appropriate for analyzing data acquired with a different cup type. Hence, further development is needed in order to adjust statistical models to a more general application either in terms of different processing methods or thermal analysis procedures.

Moreover, the large amount of data collected during laboratory and industrial trials will allow for a more thorough investigation of the statistical handling of those data. Indeed, a more careful statistical analysis including mainly non-linear estimation of the parameters would be of importance in order to produce a more efficient data reduction and iron characterization.

In addition, not only the analyzed temperatures are being used as relevant microstructural indices but also different undercooling differences were proposed as

indicators of microstructural features. Therefore, thermal analysis can be able to provide a better characterization of an iron melt on the foundry floor. (103)

## **2.5 Tensile Property of Compacted Graphite Iron.**

The mechanical properties of compacted graphite cast irons have been reported as being intermediate between those of high grade gray irons and nodular irons of similar matrix structures (98, 105). Tensile and yield strengths of compacted graphite irons are equal to, or exceed, those of high strength gray irons and may approach those of ductile irons. Since the graphite particles are compacted and have rounded ends, a higher strength than that of flake graphite iron is expected, and because of interconnection of graphite, compacted graphite iron is not as strong as ductile iron (105).

Even though the range of strengths varies depending upon chemical composition, nodularity and section thickness, it is reported (98, 105) that tensile strengths are 45,000-75,000 psi at elongations of 1-6%. Higher strengths are associated with the amount of pearlite promoting elements, higher nodularity and thinner sections due to rapid solidification preventing carbon diffusion to form graphite, then leaving a ferrite matrix (105).

## **2.6 Thermal Conductivity**

The thermal conductivity of all cast irons appears to be controlled by the form,

amount and distribution of graphite contained in compacted graphite irons enhances its thermal conductivity when compared with ductile irons (104). Table 2.2 presents some published thermal conductivity data for cast irons (98, 104) with different graphite structure. The conductivity of compacted graphite irons was generally lower than that of flake graphite. However for near-eutectic composition, the conductivity was comparable to that of low carbon equivalent, high strength gray cast irons, increased carbon equivalent, flake length, or ferrite content of matrix in compacted graphite irons with a given nodularity increased the thermal conductivity of metal (104).

Table 2.2. Thermal conductivity values for various cast irons (98)

Property	Gray Cast Iron	CG Cast Iron	Ductile Cast Iron
Thermal Conductivity (Cal/cm sec <sup>0</sup> C )	0.105-0.135	0.08-0.12	0.075-0.09

Other studies (106, 107, 108, 109), gave typical values of thermal conductivity of different gray and ductile iron grades via temperatures, Tables 2.2 and 2.3 represent these values for increasing temperatures.

For gray irons, thermal conductivity decreases with temperature. This trend is observed in many reports (106, 107, 108, 109), although there is no discussion on the cause of this behavior.

Table 2.3 Results of thermal conductivity for different grades of gray Irons (108).

Temperature ( <sup>0</sup> C)	Thermal conductivity (W/K.m)					
	GJL 150	GJL 200	GJL 250	GJL 300	GJL 350	GJL 400
100	52,5	50,8	48,8	47,4	45,7	44,0
200	51,5	49,8	47,8	46,4	44,7	43,0
300	50,5	48,8	46,8	45,4	43,7	42,0
400	49,5	47,8	45,8	44,4	42,7	41,0
500	48,5	46,8	44,8	43,4	41,7	40,0

Table 2.4 Results of thermal conductivity for ductile irons (110)

	GGG-35.3	GGG-40	GGG-50	GGG-60	GGG-70	4 Si-Mo
100 °C	40.2	38.5	36.0	32.9	29.8	25.1
200 °C	43.3	41.5	38.8	35.4	32.0	27.2
300 °C	41.5	39.8	37.4	34.2	31.0	28.1
400 °C	38.8	37.4	35.3	32.8	30.3	28.6
500 °C	36.0	35.0	33.5	31.6	29.8	28.9

## 2.6 Multiple Regression Analysis

In the field of cast iron, multiple regression analysis was used to investigate the relation between thermal parameters and chilling tendency, the results of a previous investigation were reanalyzed using more comprehensive statistical method, the reason of that was to provide a foundry men with a strong, accurate and uncomplicated regression model (111,112), one that can anticipate a give base iron chilling tendency on the foundry floor based primarily on thermal analysis parameters (112).

## **CHAPTER 3**

### **EXPERIMENTAL PROCEDURE**

#### **3.1 WORK PLAN**

##### **3.1.1 Effect of Treatment Agents**

The treatment agents either FeSiMgCe mish metal or FeSiMg were used by treating the molten iron base metal with plunger treatment technique at 1450-1500 °C. The composition of the agent materials are

##### **FeSiMgCe mish metal**

%Mg: 5                      %Si : 45      %Ce :2.5      %Fe :balance

##### **FeSiMg**

%Mg: 5                      %Si : 45                                      %Fe :balance

##### **3.1.2. Effect of Mg/S Ratio**

In order to investigate the effect of Mg/S ratio on the graphite morphology and to optimize a suitable Mg/S ratio at which compacted graphite dominates in the matrix, Mg/S ratio was changed in the range 2/3 to 7/1 with each treatment agent, and its effects on the graphite morphology were investigated for each ratio value.

### **3.1.3. Effect of Section Thickness**

For this purpose, a standard stepped blocks in a dimension of 50mm x 160mm with thickness starts from 5mm and increases to 40 mm as shown in figure 3.1 was produced in green sand molds. The percentage of graphite morphology at every section was investigated and the optimum composition was identified based on the formation and percentage of compacted graphite and within all section thickness.

### **3.1.4. Effect of Oxygen Activity**

For being an important factor affecting the final graphite morphology, the oxygen activity level which is suitable for production of compacted graphite iron was identified.

### **3.1.5 Thermal Analysis**

The solidification temperatures of the successful chemical composition heats were determined to be used as a reference during the production process. These critical temperatures are liquids temperature, solids temperature, lower and higher eutectic temperature, under cooling and recalescence.

## **3.2. Characterization of the Cast Iron Alloys Produced.**

The examinations and investigations of the effect of the type of treatment agents, the Mg/S ratio and the section thickness on the compacted graphite morphology were investigated based on the following:

### **3.2.1 Metallographic Examination**

Specimens were prepared by grinding and polishing. Percentage of graphite morphologies were calculated due to simple quantitative approach on photographs. At most 20% nodularity was accepted.

### **3.2.2 Tensile Testing.**

Specimens were tested by means of tensile testing. Both tensile and fracture strength in the range of 405-620 MPa for pearlitic iron matrix or 250-380 MPa for ferritic iron matrix were obtained.

### **3.2.3 Electrical and Thermal Conductivity Measurements.**

For being the distinct characteristic of compacted graphite iron, thermal conductivity changes were tested by using of suitable set up because of the direct proportion between the thermal conductivity and electrical conductivity, moreover electrical conductivity measurements seems to be more practical to carry out, So for this purpose specimens were machined to a standard dimensions and resistivity were measured at high temperature as a means to determine the electrical conductivity changes.

### **3.3 Regression Analysis.**

In order to correlate the Mg/S ratio, the oxygen activity, undercooling, fracture strength and thermal conductivity for all heats (in which 80% of compacted graphite



was observed) multiple regression analysis was performed.

A step block casting in green sand with 5, 10, 20, 40, mm thick steps as illustrated in Figure 3.1 were used to produce compacted graphite iron alloys to perform physical, mechanical and metallographic investigations. The tensile test bar with a dimension shown in Figure 3.2 and standard spectrometer analysis forms were produced with different chemical compositions on the base of different Mg/S ratios.

In this study, Sorel and steel scrap were use as charge material, either FeSiMgCe misch metal or FeMgSi were used as an agent material and Cu was used as an alloying element to control the pearlitic matrix.

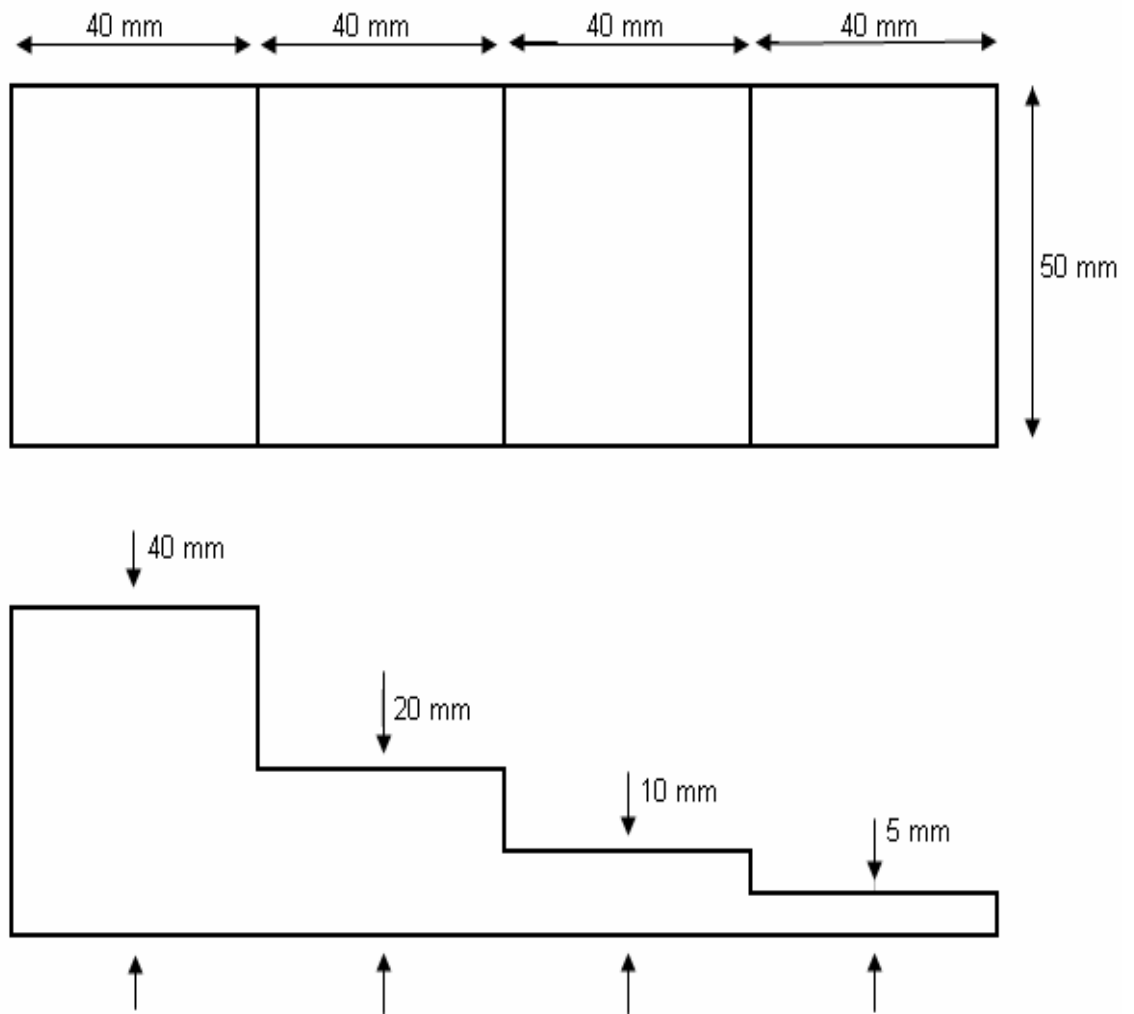


Figure 3.1 Step block with 5, 10, 20 and 40 mm thick steps

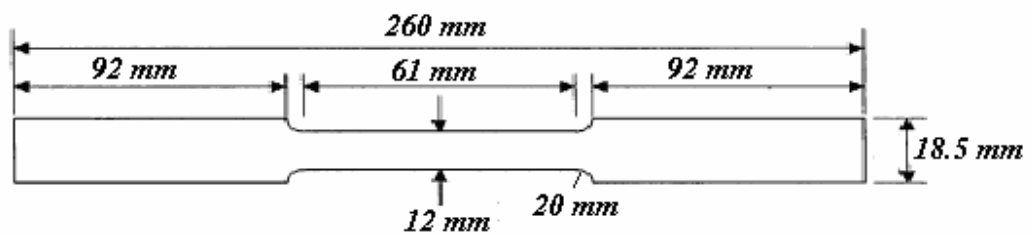


Figure 3.2 Dimensions of the cast tensile test bar machined

### 3.4 Charge Calculation

The main ingredients of the alloy charge used for induction furnace heats were Sorel and steel scrap in the proper proportions to bring about the desired carbon content of the heats. About 17 Kgs of charge was prepared at every heat. The silicon content of the base iron was adjusted by the additions of 75% ferrosilicon taking into account the expected silicon pick-up during post inoculation in addition to the expected silicon recovery rate. All compacted graphite cast iron heats were treated with Denodul FeSiMgCe misch metal or FeSiMg, and post inoculated with a 0.5% of 75% ferrosilicon before delivery. A typical charge calculation is shown in Table 3.1 through Table 3.3

Table 3.1. Aimed values of carbon equivalent, total carbon and silicon

Aimed carbon equivalent	4.13 to 4.47 %
Aimed total carbon	3.30 to 3.90 %
Aimed Silicon	2.00 to 2.70 %

From 12521 gm of Sorel, 549 gm of steel, 90 gm of FeSi, 380 gm of FeSiMg as treatment material and 160 gm of Copper with 30 – 33 % Mg recovery we can get the following tabulated values Table 3.2 and 3.3

Table 3.2 .Calculated values of silicon, Mg/S ratio and copper

Carbon	Silicon	Mg/S ratio	Copper
3.90%	2.40%	4.4	1.16%

Table 3.3. Example for a charge used in experiments

Materials	Amount.( gm )	T.C (%)	Si (%)	Mg (%)	S (%)
Sorel	9000	3.311	0.5698	0.00385	0.00931
Steel	533	0.011	0.0008	-	0.0008
Denodul	316	-	0.1125	0.01375	-
FeSi	78		1.36	-	-
Post inoculant	0.5% of total weight		0.375	-	-
Cu	123		-	-	0.497
Total	10.10	3.172	2.4181	-0.0324	0.507117

Based on the above example, a suitable Excel computer program was used to calculate the required charge quantity containing different ratio of Mg/S.

### 3.5 Melting Procedure

Once the charge materials, Sorel and steel scrap, were prepared and calculated, they were placed in induction furnace. After having molten metal, alloying materials such as Cu and FeSi were added to the furnace. In the stage of spheroidizing treatment, FeSiMgCe Misch metal or FeSiMg metal was added by plunging method with the plunger ladle shown in Figure 3.3.

The treatment was made at temperatures of 1450-1500 °C. Post inoculation was accomplished by adding 75% foundry grade ferrosilicon (lump size is between 1-2 mm) on top of the molten metal in the ladle. The post inoculation time was hold in all castings. Holding time, post inoculation temperature and pouring temperature were recorded as shown in Table 3.1.

In order to mark which specimen belongs to which particular casting, codes were given to the samples. The sample codes are shown in Table 3.2.

### **3.6 Metallographic Examinations**

#### **3.6.1 Sample Preparation and Optical Microscopy Studies**

The metallographic specimens were taken from each section of stepped block. Specimens were prepared by using 120, 220, 320, 400, 500, 600, 800, and, 1200 mesh of abrasive emery papers and polished by the use of METASERV universal polisher equipment as shown in Figure 3.4.

#### **3.6.2 Image Analyzer Study**

The specimens were examined by optical microscope which is shown in Figure 3.5, and the prepared metallographic specimens were also examined by using CLEMEX Image Analyzer System which is shown in Figure 3.6. By this system, the % of graphite area was determined on the polished surface of the specimen and total graphite area % was determined form different regions of the specimens. According to the results, average graphite area was calculated in terms of total area for each type of graphite cast iron.

Table 3.4. Treatment details

Code No	Treatment Method	Treatment Time (Sec.).	Treatment Temp. °C	Holding time after treatments (Sec.)	Pouring Temp. °C.
1A	Plunger	300	1450	70	1425
4A	Plunger	480	1455.6	100	1467.1
5A	Plunger	330	1463.3	78	1435.3
8A	Plunger	420	1450	90	1400
4B	Plunger	360	1450	60	1400
5B	Plunger	300	1465	75	1452.6
6B*	Plunger	a ) 540	1450	60	1430
		b ) 840	1450	60	1420
7B	Plunger	420	1460	90	1425
8B	Plunger	360	1467.1	90	1425
6B	Plunger	400	1472	90	1473

### 3.6.3 Chemical Analysis

The chemical analysis of the specimens was carried out in ICF and in ERKUNT A.Ş laboratories. OBFL spectrometer in Erkunt was used for chemical analysis which is

shown in Figure 3.7, and the results were taken based on the average of four different positions within the same specimen.

Table. 3.5. Descriptions of codes

Code	Descriptions
1	Mg/S ratio is 0.50
2	Mg/S ratio is 0.70
3	Mg/S ratio is 1.00
4	Mg/S ratio is 2.00
5	Mg/S ratio is 3.00
6	Mg/S ratio is 4.60
7	Mg/S ratio is 5.30
8	Mg/S ratio is 6.50
A	Trail made by using FeSiMg Ce mish metal as a Treatments agent
B	Trail made by using FeSiMg as a Treatments agent
d	5 mm section thickness
e	10 mm section thickness
f	20 mm section thickness
g	40 mm section thickness

Example: 1Bg is a sample taken from 40 mm section thickness of the trial of FeSiMg treatments in which the ratio of Mg/S is 0.50.

### 3.7 Oxygen Activity Measurements

The measurement of active oxygen was done on by Celox Foundry device manufactured by Heraeus Electro-Nite Company shown in Figure 3.8. This device with a sensor is used for measurements of active oxygen. It is carried out based on the use of electro-chemical cell in combination with a thermocouple working with the principle of Nernst's law:

$$\log a(o) = 8.62 - \frac{13580 - 10.08(E + 24)}{T} \quad 3.1$$

Where T is the bath temperature in  $^{\circ}\text{K}$ , E is the EMF in mV and a (o) is the oxygen activity given in ppm.



Figure 3.3 Plunger method used for CG iron production





Figure3.4. METASERV universal polishers



Figure3.5. Optical microscope



Figure 3.6. CLEMEX image analyzer system.



Figure 3.7. OBFL spectrometer.

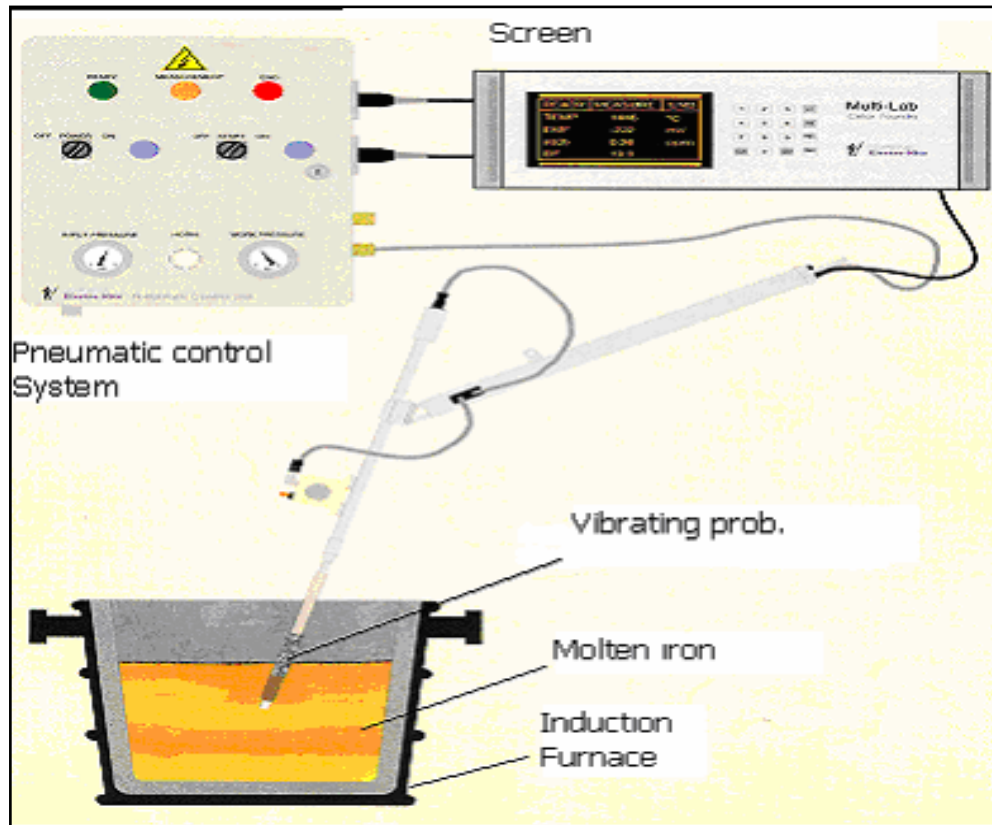


Figure 3.8 Heraeus Electro-Nite Celox foundry device with vibrating lance

### 3.8 Thermal Analysis

Thermal analysis is the process of determining the temperatures at which the phase transformation and a change in the atomic arrangement takes place by observing the critical temperature such as eutectic temperatures ( $T_E$ ), temperature of eutectic undercooling ( $TEU$ ), solidus temperatures ( $TS$ ). Undercooling which is the difference between eutectic temperatures and temperature of eutectic undercooling and recalescence which is the difference between the solidus temperatures and temperatures of eutectic undercooling. These critical temperatures are shown in Figure 3.9.

### 3.9 Tensile Strength Measurements

The as cast tensile test bars were first machined into the dimensions as shown in Figure 3.2 in order to get ready for tensile test, then the bars are subjected to tensile test by using ALSA universal testing machine which is shown in Figure 3.10.

### 3.10 Thermal Conductivity Measurements

As a distinguishable characteristic of compacted graphite iron, thermal conductivity changes with each heat and with temperature gradients ranging from room temperatures to 500 °C were measured. This measurement was done in the manner of measuring electrical resistivity of specimen machined to the dimension shown in

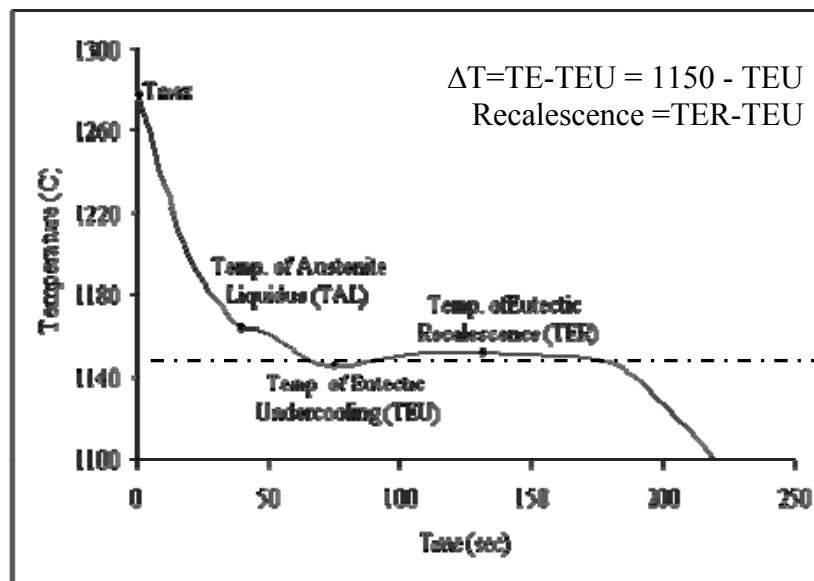


Figure 3.9 Schematic of cast iron cooling curve



Figure 3.10 ALSA universal testing machine used for tensile test

The two point probe resistivity measurement technique shown in Figure 3.12 was used for high temperature measurements. It consists of 30 cm long and 1.2 cm diameter alumina tube. Figure 3.13 shows the scheme of the specimen fixing mechanism used in high temperature resistivity measurements.

This tube has a window close to the bottom as the main part for charging the specimen. Alumina insulation spaghetti at the bottom of the tube was fixed by alumina cement. Insulation spaghetti which was able to move up and down was attached to the open end by using a special mechanism made from brass as shown in Figure 3.13. Two Pt-Pt/13% Rh thermocouples were passed through the spaghettis and all these wires were collected at the open end.

Samples whose resistivity to be measured were placed between these two lines of thermocouples and a pressure was applied to get better contacts. With that mechanism, it was possible to measure resistivity of specimens simply by pumping 1 A constant current through the Pt-Pt/13% Rh wires and detecting the potential drop in the specimen by means of voltmeter device. The specimen was held at each temperature measurements for 1 hour to get equilibrium.

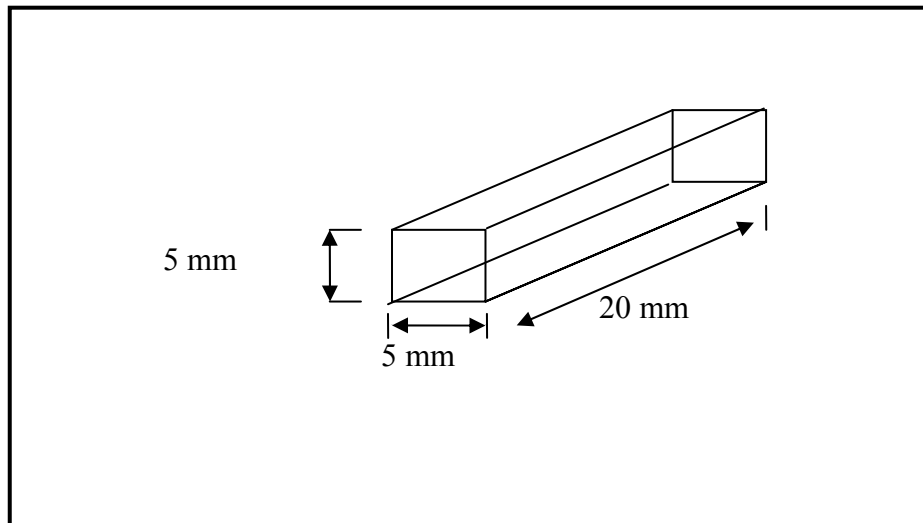


Figure 3.11 The dimensions of the electrical resistivity specimen

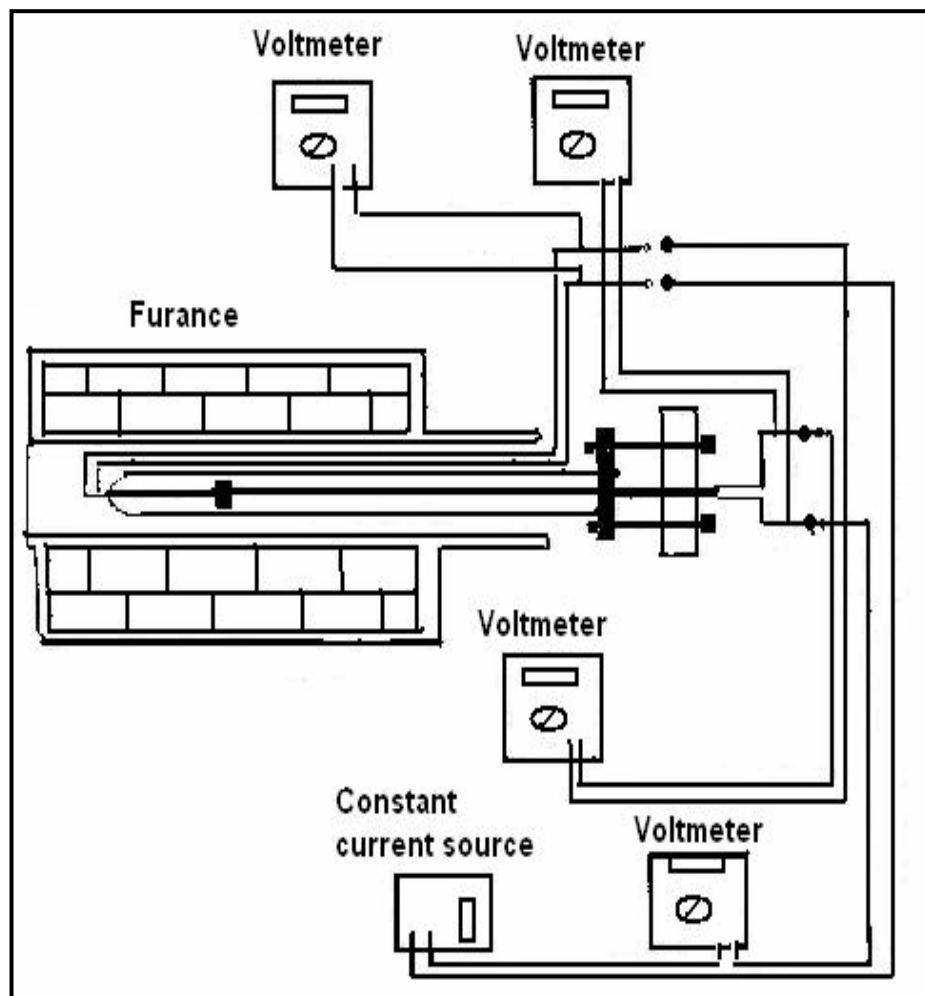


Figure 3.12 The setup used for electrical resistance measurements (101)

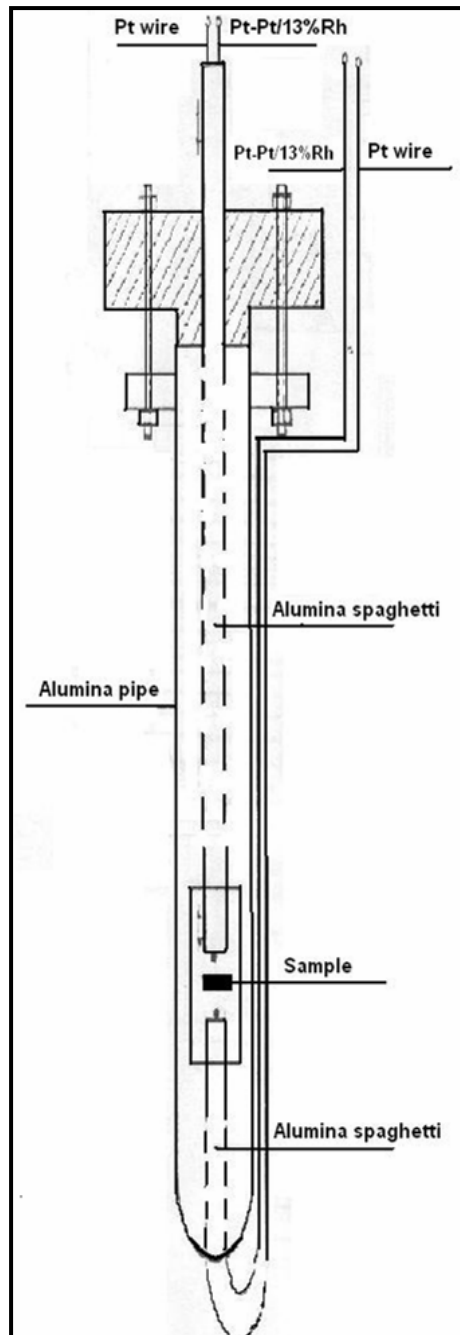


Figure 3.13. The sketch of the specimen fixing mechanism used in high temperature resistivity measurements (101).

As it's well known, the free electrons are primarily responsible for the electrical and thermal conductivity of metals and alloys; therefore, the Wiedemann-Franz-Loranz



Law can be applied to relate the thermal conductivity to the electrical resistivity.

(106) as

$$\frac{\lambda \rho_e}{T} = \frac{\pi^2 K^2}{3 e^2} = L_0 \quad 3.1$$

Where  $\lambda$  is the thermal conductivity, T is the absolute temperature,  $\rho_e$  is the electrical resistivity, K is the Boltzman constant and e is the electron charge. The constant

$$L_0 = \frac{\pi^2 K^2}{3 e^2} = 2.445 \times 10^{-8} \text{ } w\Omega K^{-2} \quad 3.2$$

The electrical resistance R and electrical resistivity  $\rho_e$  are related and given by the formula

$$R = \frac{\rho_e L}{A} \quad 3.3$$

Where L and A are the length and the cross-section area of specimen respectively. Therefore, the thermal conductivity is

$$\lambda = \frac{2.445 \times 10^{-8} \times T \times L}{R \times A} \quad 3.4$$

### 3.11 Multiple Regression Analysis

The multiple regression formula is defined as follows:

$$\hat{y} = \hat{a} + \sum_{i=1}^k \hat{b}_i x_i \quad 3.5$$

Where:

y = dependent variable

k = number of independent variables

$x_i$  =  $i$  th independent variables, where  $I = 1 \dots k$

$\hat{a}$  = estimated intercept term.

$\hat{b}_i$  = estimated slope coefficient associated with variable  $x$ .

Since the actual computations of multiple regression coefficients can be rather complex, the formulas and results are correlated and then they are discussed.

The individual steps to yield the formulas from data are not incredibly difficult, but as the number of independent variables increases, the number of steps increases very quickly. As a result these computations can become difficult to carry out by hand. The large number of steps required makes manual calculations time-consuming and prone to error. Fortunately, today there are numerous computer software programs available to aid us in performing these calculations.

In this study, Microsoft Excel software program was used to perform multiple regressions. The dependent variable is either the fracture strength or the thermal conductivity and the independent variables are the Mg/S ratio, undercooling and oxygen activity.

## **CHAPTER 4**

### **EXPERIMENTAL RESULTS**

#### **4.1 The Effect of Mg/S ratio and the Cooling Rate on the Microstructures of Heats, Treated with FeSiMg-Cermish Metal or Treated with FeSiMg**

The technique employed for producing compacted graphite iron is the plunger method, and the treatment materials used are FeSiMg cermish and FeSiMg. The standard stepped blocks were cast and a wide range of graphite morphologies were observed.

In order to investigate the effect of Mg/S ratio on these morphologies and to find the appropriate Mg/S ratio at which compacted graphite dominates in the matrix without the effect of section change, eleven heats were prepared in an induction furnace having capacity of approximately 17 kg.

At lower Mg/S ratio which was defined by E. Selçuk and Yaşar (80) as spheroidizing potential, Mg/S ratio equal 0.5, 1A heat with the chemical composition shown in the Table. 4.1 was obtained..

Table 4.1. The chemical composition of heat 1A

	%Si	%C	%Mg	%Cu	%S	%P	%CerMM
Analyzed	-	-	-	-	-	-	-
Calculated	2.330	3.839	0.022	1.061	0.0111	0.009	0.0306

In this heat, the graphite growth mode was lamellar growth. At thin sections type E flake graphite was observed. As section gets thicker, A type was observed. This is due to low Mg/S ratio. Figures 4.1 through 4.4 show the microstructures of sections varying from 5 mm to 40 mm.

As Mg/S increases, Mg/S being 2.0, heat 4A was obtained with the chemical composition shown in the Table. 4.2. In this heat, the graphite morphology was

Table 4.2. The analyzed and the calculated chemical composition of heat 4A

	%Si	%C	%Mg	%Cu	%S	%P	%CerMM
Analyzed	2.03	2.45	0.009	0.96	0.004	0.03	0.019
Calculated	1.699	3.839	0.022	1.061	0.0111	0.009	0.0306

again in the form of flake graphite. Figures 4.5, 4.6, 4.7 and 4.8 show the microphotographs of sections varying from 5 mm to 40 mm; this is reflecting the fact

that the Mg/S ratio was not sufficient to obtain the compacted graphite.

A 4B heat was made with the chemical composition shown in Table. 4.3. In this heat, although all the treatment material was changed, the shape of graphite morphology was also in the form of flake graphite.

Table 4.3 The chemical composition of 4B heat

	%Si	%C	%Mg	%Cu	%S	%P	%CerMM
Analyzed	2.20	3.99	0.11	0.98	0.005	0.035	
Calculated	2.226	3.943	0.023	1.143	0.0113	0.0005	0

Figures 4.9, 4.10, 4.11 and 4.12 show the microphotographs of sections varying from 5 mm to 40 mm at unetched condition.

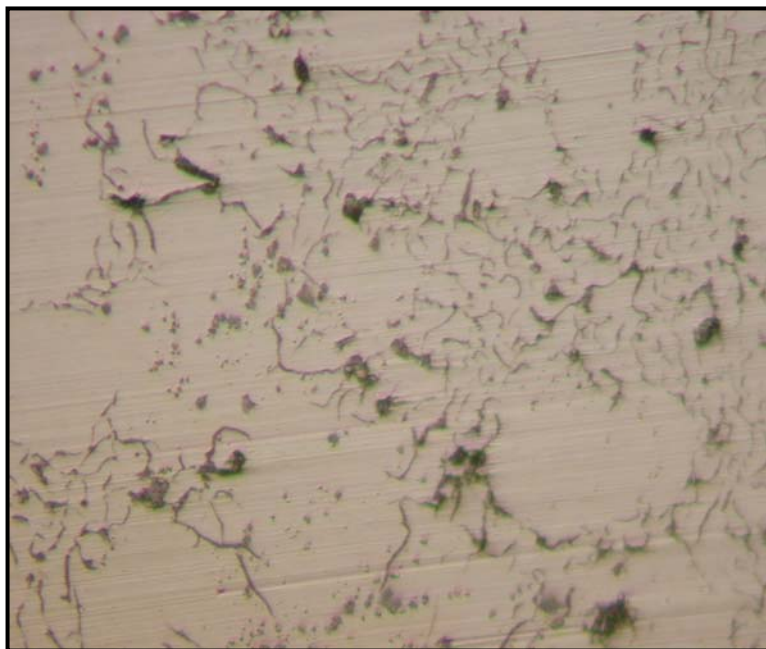


Figure 4.1 Microstructure of specimen, with 1Ad code, Treated with FeSiMg-Cermish metal, Mg/S: 0.5, Section size: 5mm, E type FG, Magnification  $\times 100$ ,

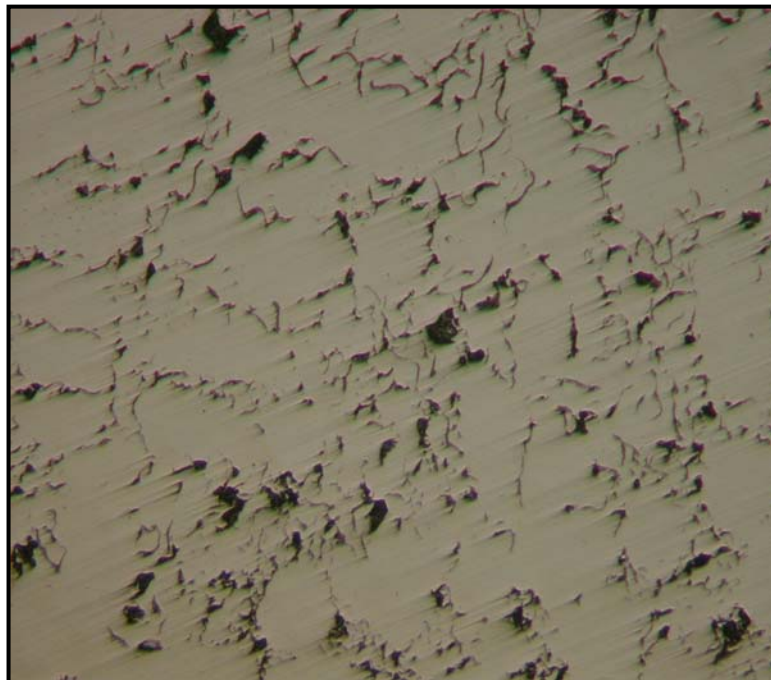


Figure 4.2 Microstructure of specimen, with 1Ae code, Treated with FeSiMg-Cermish metal, Mg/S: 0.5, Section size: 10 mm, E type FG, Magnification  $\times 100$ ,



Figure 4.3 Microstructure of specimen, with 1Af code, Treated with FeSiMg-Cermish metal, Mg/S: 0.5, Section size: 20 mm, A type FG, Magnification  $\times 100$ ,

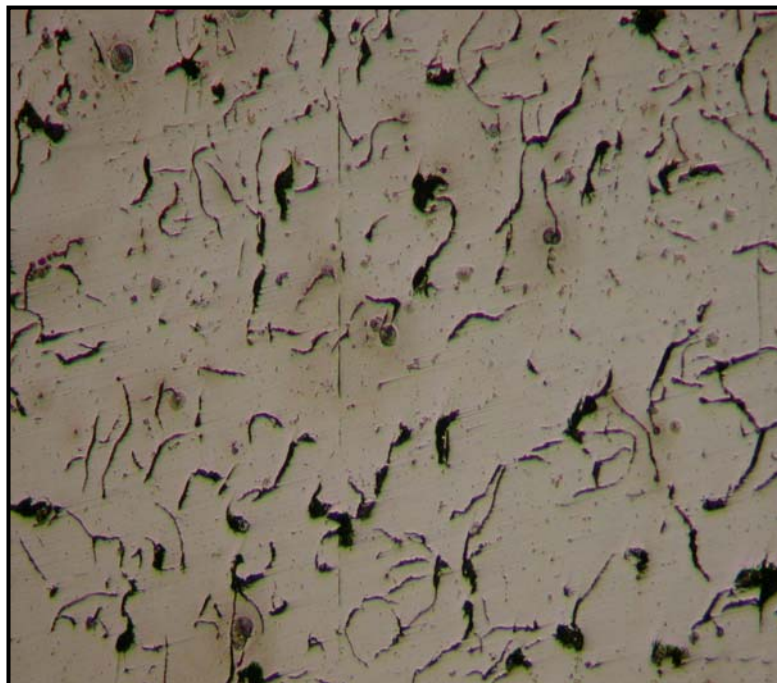


Figure 4.4 Microstructure of specimen, with 1Ag code, Treated with FeSiMg-Cermish metal, Mg/S: 0.5, Section size: 40 mm, A type FG, Magnification  $\times 100$

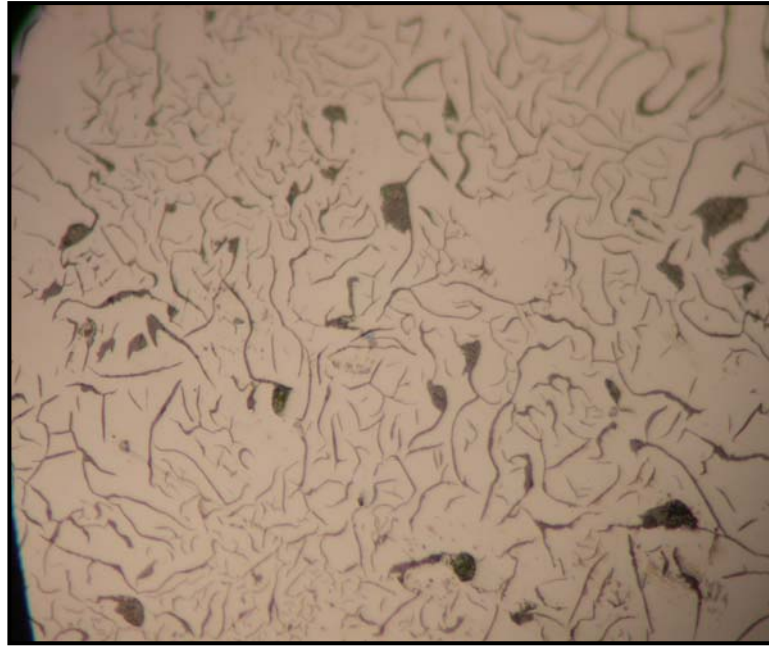


Figure 4.5 Microstructure of specimen, with 4Ad code, Treated with FeSiMg-Cermish metal, Mg/S: 2, Section size: 5mm, Type B and A FG, Magnification  $\times 500$ ,



Figure 4.6 Microstructure of specimen, with 4Ae code, Treated with FeSiMg-Cermish metal, Mg/S: 2, Section size: 10 mm, A type FG, Magnification  $\times 500$ ,



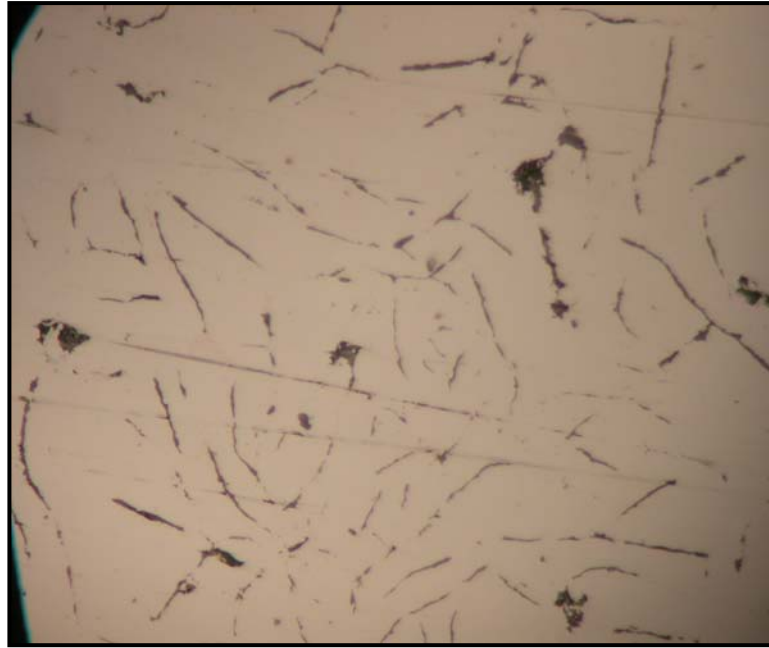


Figure 4.7 Microstructure of specimen, with 4Af code, Treated with FeSiMg-Cermish metal, Mg/S: 0.2, Section size: 20 mm, A type FG, Magnification  $\times 500$ ,



Figure 4.8 Microstructure of specimen, with 4Ag code, Treated with FeSiMg-Cermish metal, Mg/S: 2, Section size: 20 mm, A type FG, Magnification  $\times 500$ ,



Figure 4.9 Microstructure of specimen, with 4Bd code, Treated with FeSiMg, Mg/S:  
2, Section size: 5 mm, A type FG, Magnification  $\times 500$ ,

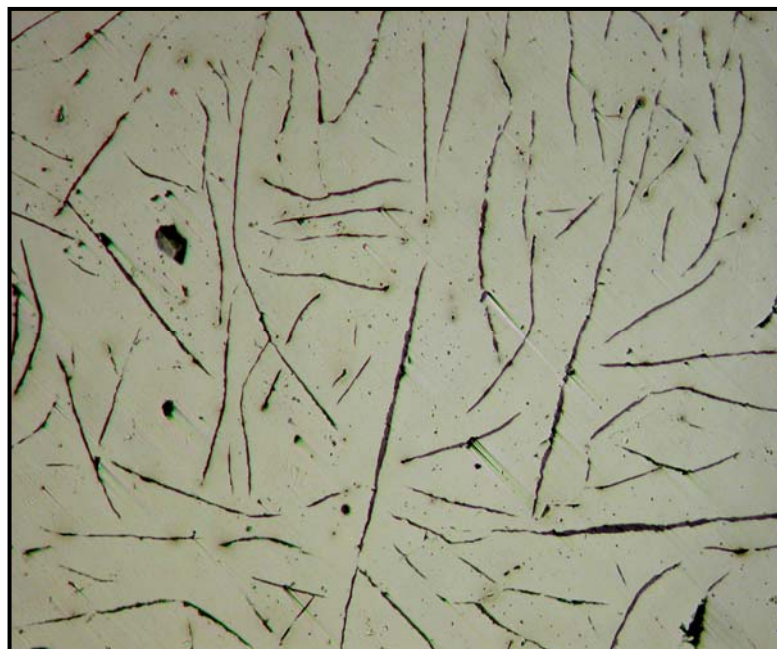


Figure 4.10 Microstructure of specimen, with 4Be code, Treated with FeSiMg, Mg/S:  
2, Section size: 10 mm, A type FG, Magnification  $\times 500$ ,

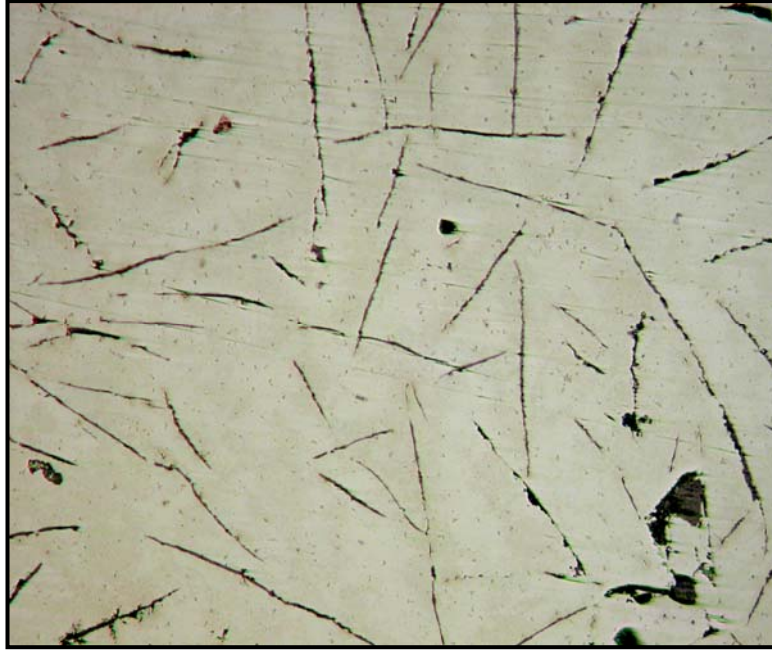


Figure 4.11 Microstructure of specimen, with 4Bf code, Treated with FeSiMg, Mg/S: 2, Section size: 20 mm, A type FG, Magnification  $\times 500$ ,

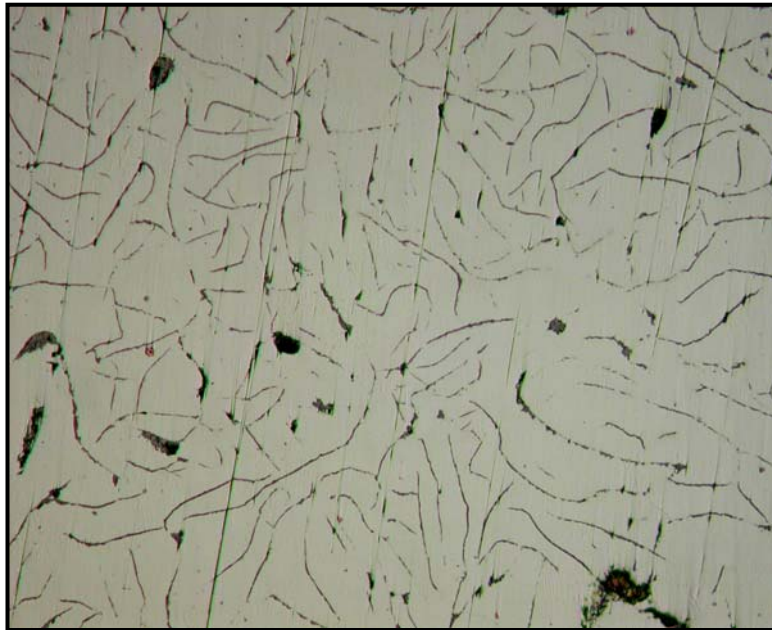


Figure 4.12 Microstructure of specimen, with 4Bg code, Treated with FeSiMg, Mg/S:2, Section size: 40 mm, A type FG, Magnification  $\times 500$ ,



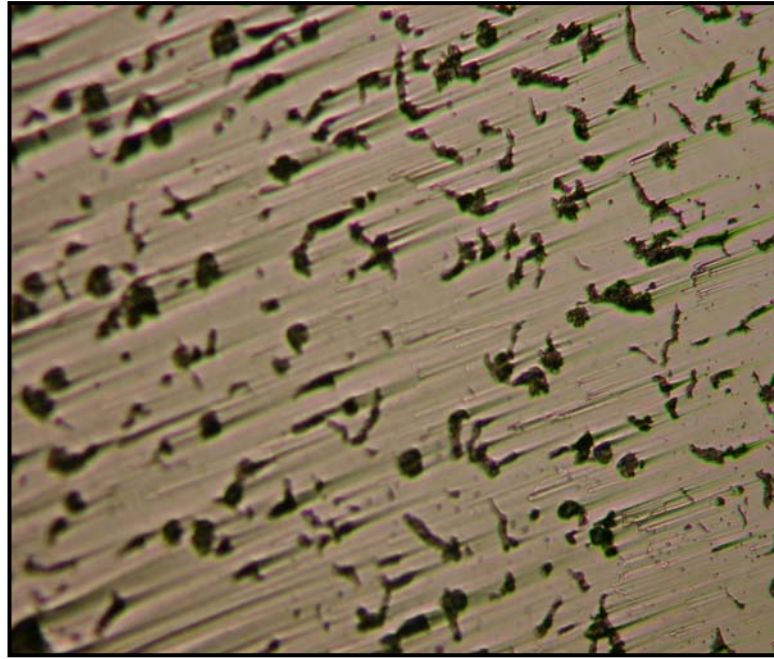


Figure 4.13 Microstructure of specimen, with 5Ad code, Treated with FeSiMg-Cermish metal, Mg/S:3, Section size: 5mm, 60.7% CG, Magnification  $\times 100$ ,

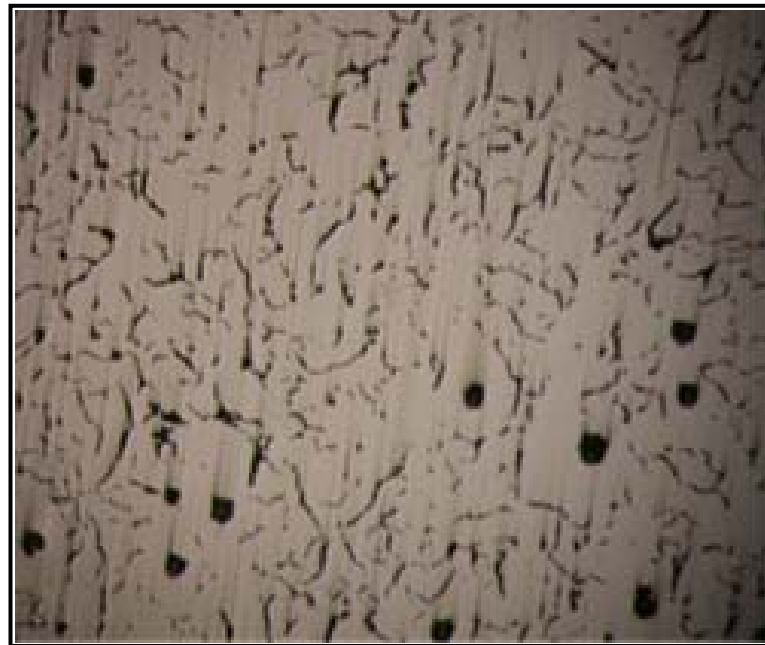


Figure 4.14 Microstructure of specimen, with 5Ae code, Treated with FeSiMg-Cermish metal, Mg/S: 3, Section size: 10mm, 98.2.7% CG, Magnification  $\times 100$ ,

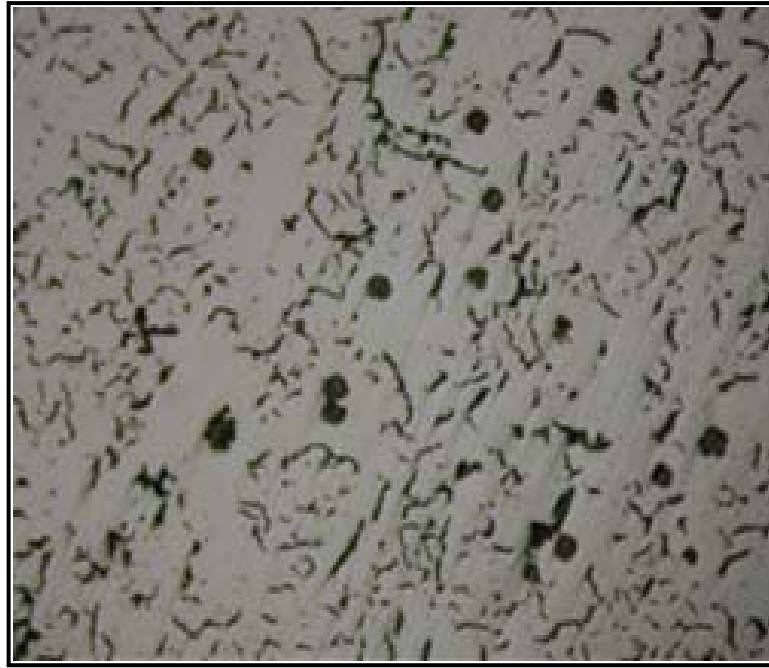


Figure 4.15 Microstructure of specimen, with 5Af code, Treated with FeSiMg-Cermish metal, Mg/S: 3, Section size: 20mm, 97.4% CG, Magnification  $\times 100$ ,

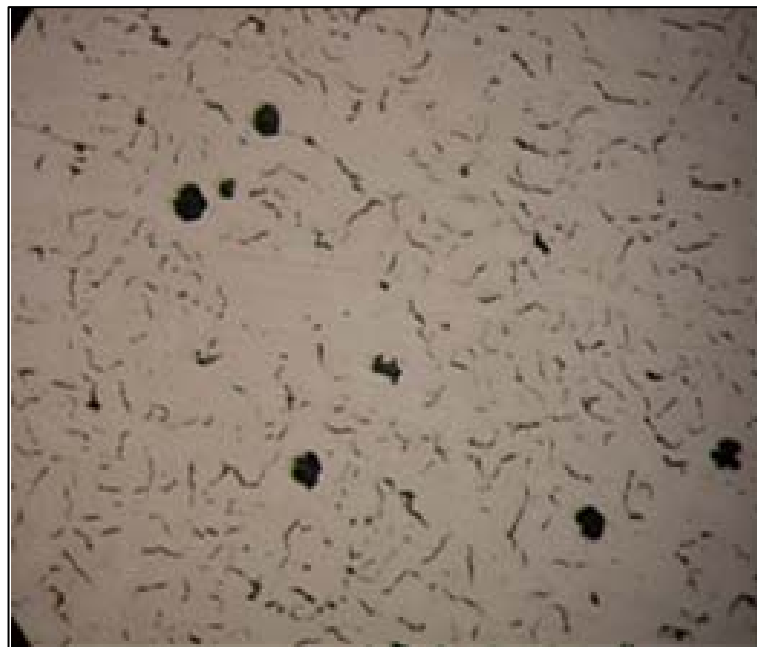


Figure 4.16 Microstructure of specimen, with 5Ag code, Treated with FeSiMg-Cermish metal, Mg/S: 3, Section size: 40mm, 99.1% CG, Magnification  $\times 100$ ,

The spheroidizing potential was further increased, and 5A trial was carried out with the chemical composition shown in Table. 4.4. This further increase in spheroidizing

Table 4.4 The chemical composition of heat 5A

	%Si	%C	%Mg	%Cu	%S	%P	%CerMM
Analyzed	2.24	3.631	0.010	0.881	0.003	0.029	0.032
Calculated	2.01	3.82	0.033	0.813	0.011	0.00090	0.04575

potential gives rise to graphite growth nucleated in the matrix tending to be changed to spheroidal in thin section and compacted in medium and large sections . This is due to the high cooling rate in thin section which resulted in reducing the carbon diffusion and then restricts the growth rate. Figures 4.13 through 4.16 show the microstructures of sections varying from 5 mm to 40 mm.

At higher spheroidizing potential, Mg/S ratio is equal to 3, with the chemical composition shown in Table. 4.5. The graphite growth mode was again spheroidal

Table 4.5 The chemical composition of heat 5B

	%Si	%C	%Mg	%Cu	%S	%P	%CerMM
Analyzed	2.12	3.590	0.013	1.09	0.005	0.033	
Calculated	2.512	3.888	0.034	1.261	0.0111	0.00057	0

in thin section and compacted in medium and large sections. Figures 4.17 through 4.20 show the microstructures of sections varying from 5 mm to 40 mm. This means that, under these conditions, compacted graphite iron could be produced in medium and large sections.

The Mg/S ratio was further increased to 4.68 and 6B heat was made with chemical composition shown Table 4.6. In this heat, beside the effect of Mg/S ratio on the

Table 4.6 The chemical composition of heat 6B

	%Si	%C	%Mg	%Cu	%S	%P	%CerMM
Analyzed	2.130	3.51	0.014	0.97	0.003	0.031	
Calculated	2.804	3.760	0.050	1.140	0.0108	0.00097	

graphite morphology, the effect of fading of magnesium on the graphite structures was also investigated. A 2cm section thickness cast was produced with two different treatment times, the first treatment time was 9 minute and the second one was 14 minute. Figure 21 and Figure 22 shows the microstructure of this heat. It's clear that, the graphite morphology was significantly affected by the treatment time.

The treatment material of the previous charge was modified and 6A heat was prepared according to the chemical composition shown in Table 4.7. In this heat, the

Table 4.7. The chemical composition of heat 6A

	%Si	%C	%Mg	%Cu	%S	%P	%CerMM
Analyzed	2.88	3.88	0.012	1.26	0.0003	0.031	0.07486
Calculated	2.654	3.846	0.052	1.221	0.0112	0.00061	0.051

spheroidizing potential, Mg/S ratio equal to 4.648, gives rise to the spheroidal to be dominating in graphite morphology in the smallest section 5 mm. As section gets thicker, the compacted graphite morphology appears in the matrix, short stubby and worm like with round tips. The microstructures of section thickness which are varying from 5 mm to 40 mm are shown in Figures 4.23 through 4.26.

At higher spheroidizing potential, Mg/S ratio being 5.3 and with the chemical composition shown in Table 4.8, 7B heat was made. In this heat the graphite shapes

Table 4.8 The chemical composition of heat 7B

	%Si	%C	%Mg	%Cu	%S	%P	%CerMM
Analyzed	2.22	3.79	0.018	0.85	0.003	0.033	
Calculated	2.65	3.90	0.062	0.89	0.0112	0.0001	

were spheroidal in the thin section and compacted in medium and large sections. Figures 4.27 through 4.30 show the microstructures of sections varying from 5 mm



to 40 mm.

At highest spheroidizing potential, Mg/S ratio reaches to 6.5 and with the chemical composition shown in Table 4.9, 8A heat was attained. The microstructures of this heat are shown in Figure 4.31 through 4.34 for the section size varying from 5 mm to 40 mm. In this heat, the spheroidal graphite shape appears in all sections, however, as section size gets thicker the degenerated nodules are also observed.

Table 4.9 The chemical composition of 8A heat

	%Si	%C	%Mg	%Cu	%S	%P	%CerMM
Analyzed	2.97	3.31	0.019	0.96	0.003	0.037	0.041
Calculated	2.757	3.75	0.066	1.298	0.0108	0.00088	0.0908

Another heat with the highest spheroidizing potential, Mg/S ratio being 6.5 was prepared according to the chemical composition shown in Table 4.10. Figures 4.35, 4.36, 4.37, and 4.38 show the microstructures of the section varying from 5 to 40 mm. In section size 5 mm and 10 mm, there are some spheroidizing, however, in the other sections, section size 20 mm and 40 mm, which are shown in Figure 4.37 and 4.38 respectively, the compacted graphite was observed in high percent in the matrix.

Table 4.10 The chemical composition of 8B heat

	%Si	%C	%Mg	%Cu	%S	%P	%CerMM
Analyzed	2.71	3.55	0.020	0.98	0.003	0.037	
Calculated	2.835	3.782	0.071	1.134	0.0109	0.00071	

In sum, according to the analysis of the metallographic examination of the specimens having graphite morphology obtained by treating the molten iron either with FeSiMg-Cermish metal or FeSiMg at different Mg/S ratio, it could be observed that the graphite morphology is not effected as section changes from 10 mm to 40 mm and at Mg/S ratio between 3.0 to 5.30 and with 5-7 min treatment reaction time, also by using either FeSiMg-Cermish metal or FeSiMg as a treatment material, It is possible to produce compacted graphite having section thickness between 10 mm and 40 mm.

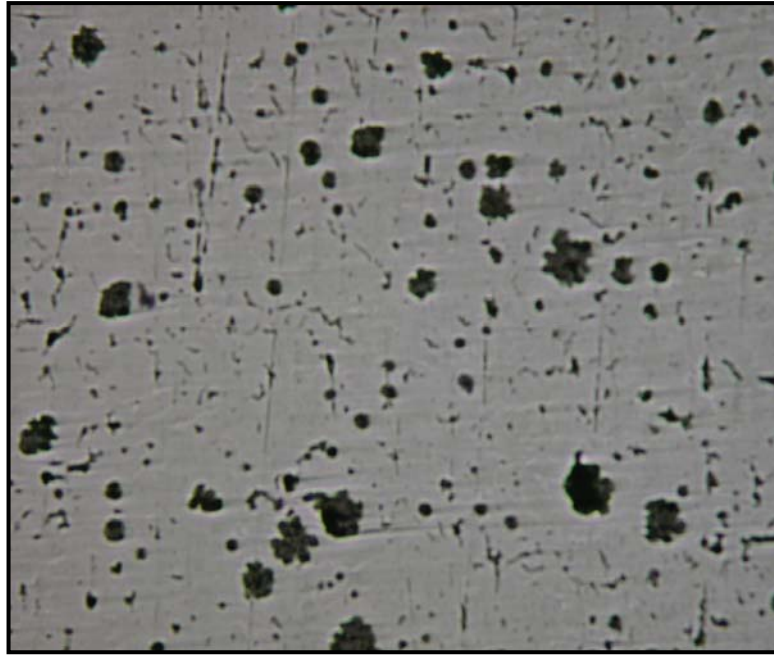


Figure 4.17 Microstructure of specimen, with 5Bd code, Treated with FeSiMg, Mg/S: 3, Section size: 5mm, 76% CG Magnification  $\times 100$ , Unetched

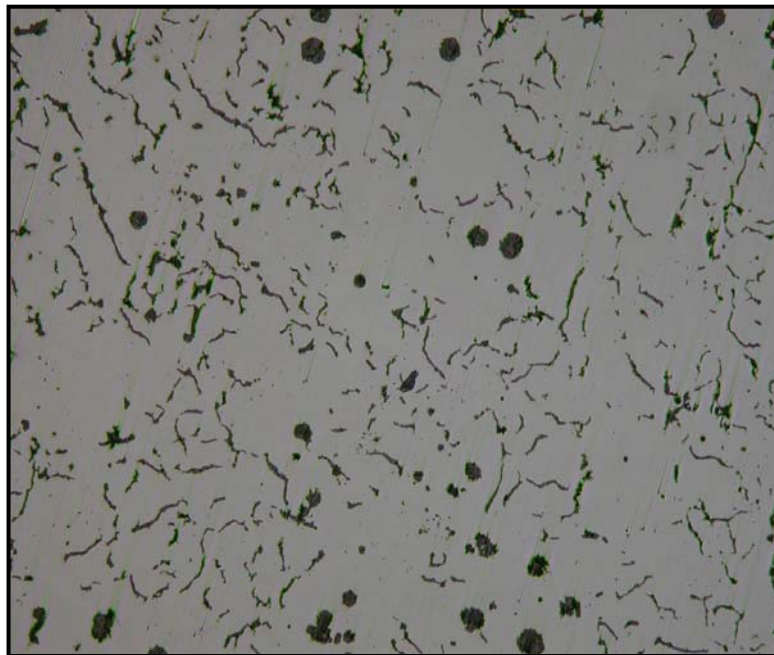


Figure 4.18 Microstructure of specimen, with 5Be code, Treated with FeSiMg, Mg/S: 3, Section size: 10mm, 95.2% CG Magnification  $\times 100$ ,



Figure 4.19 Microstructure of specimen, with 5Bf code, Treated with FeSiMg, Mg/S: 3, Section size: 20mm, 99.5% CG Magnification  $\times 100$ ,

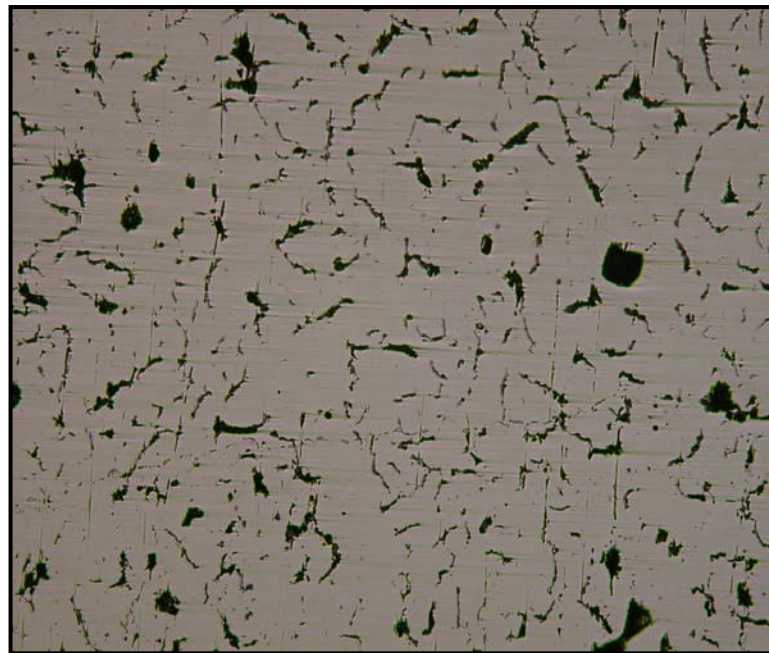


Figure 4.20 Microstructure of specimen, with 5Bg code, Treated with FeSiMg, Mg/S: 3, Section size: 40mm, 98.9% CG Magnification  $\times 100$ ,



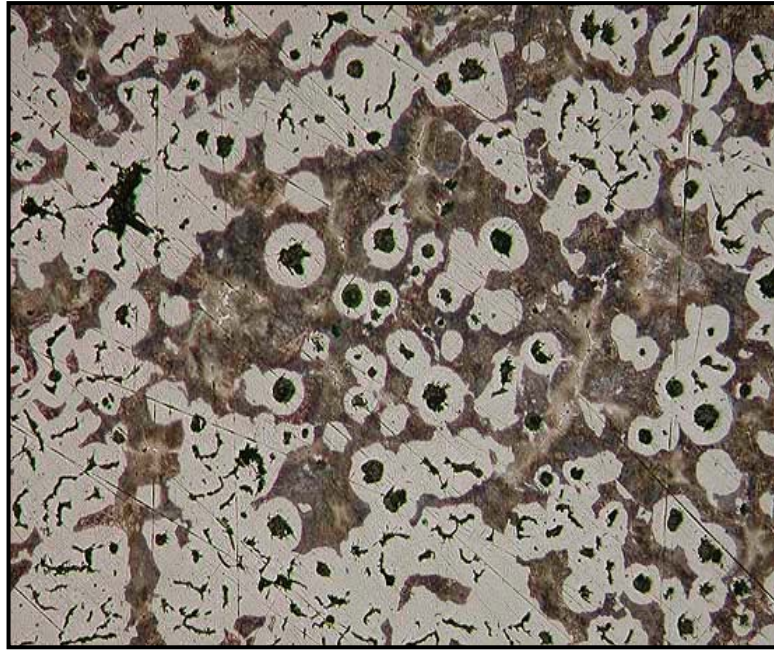


Figure 4.21. Microstructure of specimen with 6Bf code. Treated with FeSiMg, Mg/S: 4.6, Section size: 20mm, 98.7% CG Magnification  $\times 100$  and 9 minute treatment time, 2% Nital etch

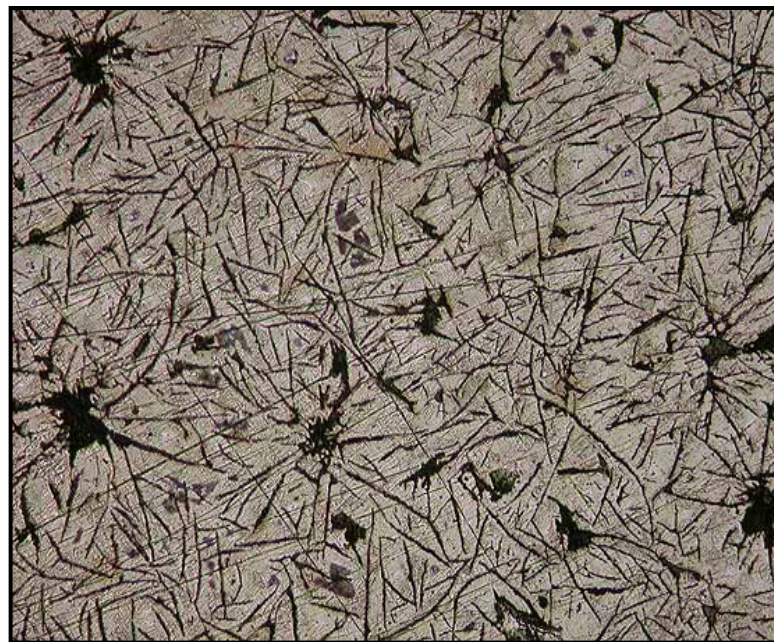


Figure 4.22. Microstructure of specimen with 6Bf code, Treated with FeSiMg, Mg/S:4.6, Section size: 20 mm, 100% Type A FG, Magnification  $\times 100$  and 14 minute treatment time , 2% Nital etch

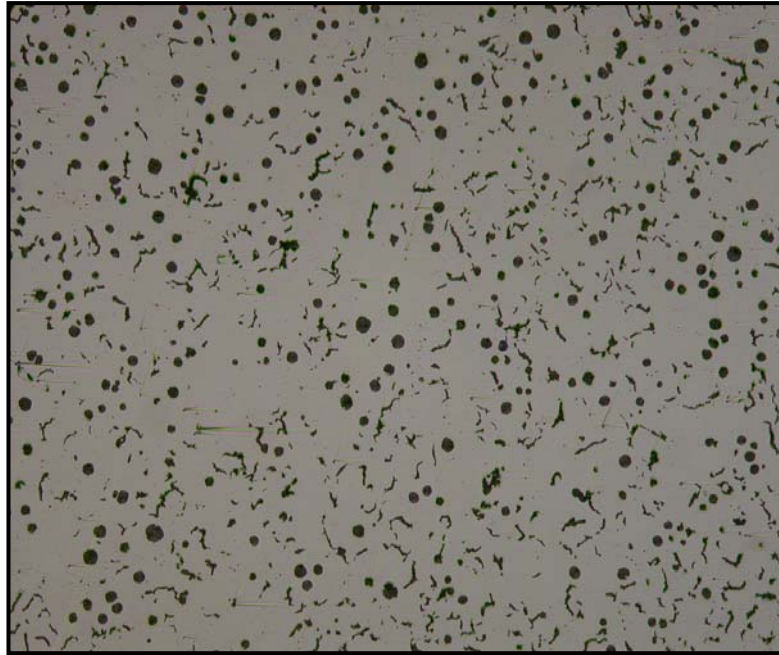


Figure 4.23 Microstructure of specimen, with 6Ad code, Treated with FeSiMg-Cermish metal, Mg/S: 4.6, Section size: 5mm, 40.6% CG, Magnification  $\times 100$ ,

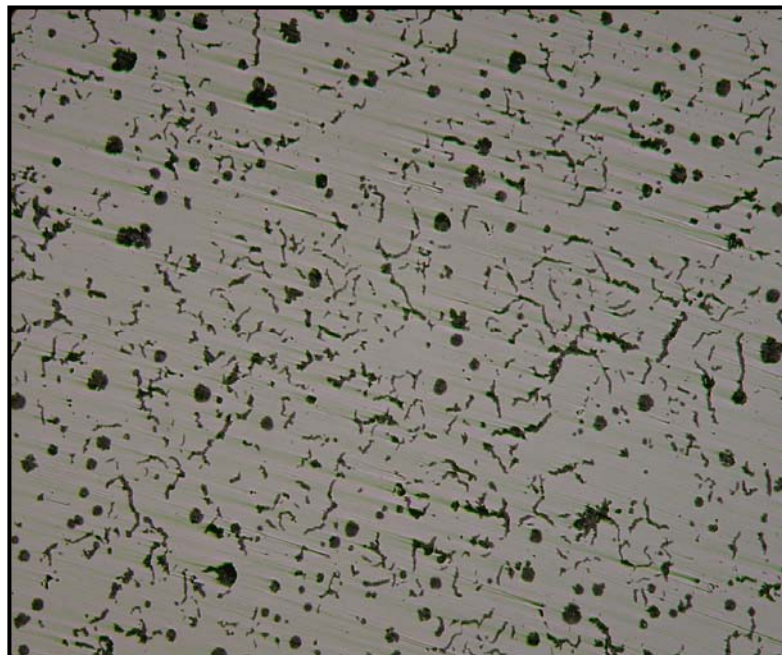


Figure 4.24 Microstructure of specimen, with 6Ae code, Treated with FeSiMg-Cermish metal, Mg/S: 4.6, Section size: 10 mm, 67.6% CG Magnification  $\times 100$ ,



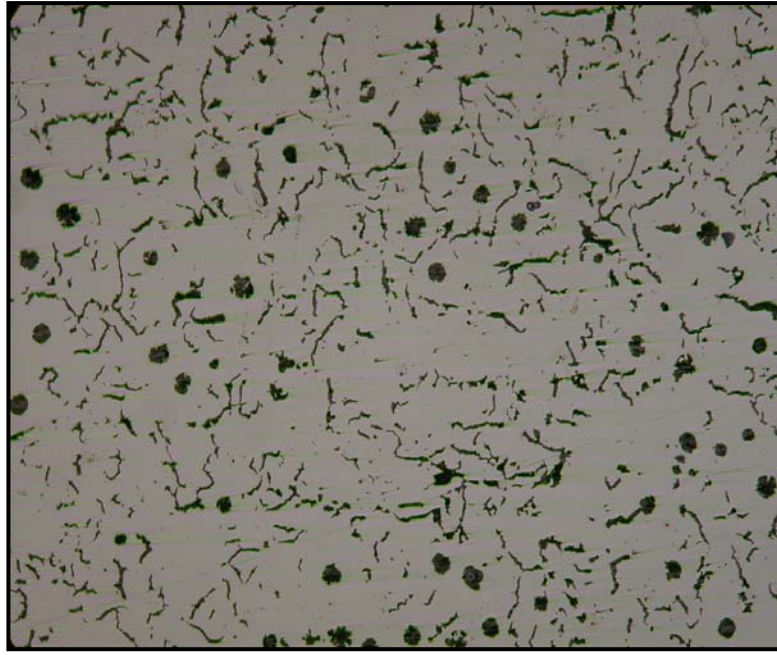


Figure 4.25 Microstructure of specimen, with 6Af code, Treated with FeSiMg-Cermish metal, Mg/S: 4.6, Section size: 20 mm, 80 % CG Magnification  $\times 100$ ,

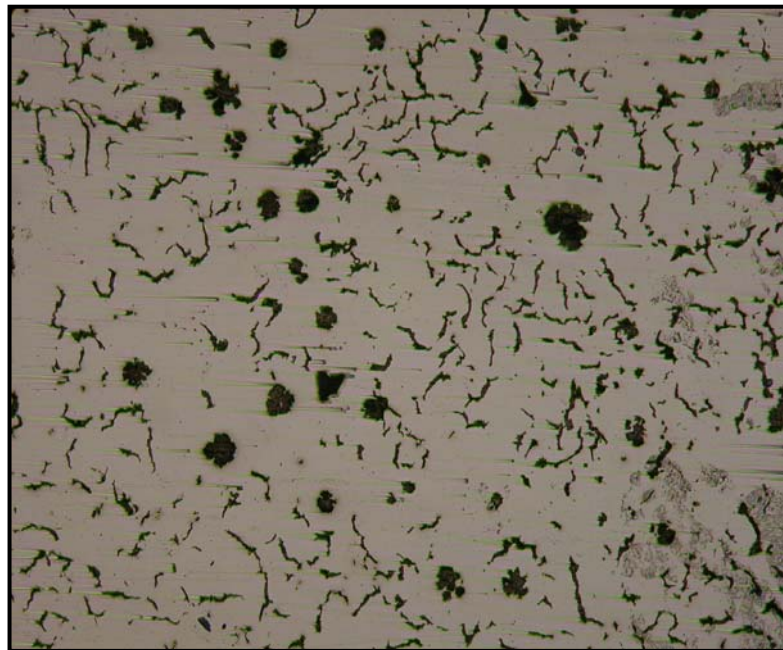


Figure 4.26 Microstructure of specimen, with 6Ag code, Treated with FeSiMg-Cermish metal, Mg/S: 4.6, Section size: 40 mm, 95 % CG, Magnification  $\times 100$ ,

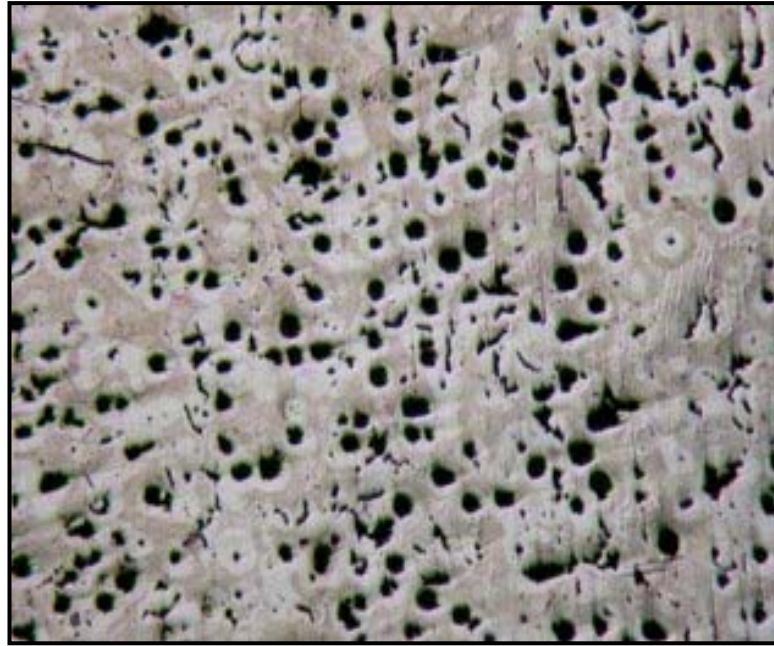


Figure 4.27 Microstructure of specimen, with 7Bd code, Treated with FeSiMg, Mg/S: 5.3, Section size: 5mm, 6.5 % CG, Magnification  $\times 100$ ,

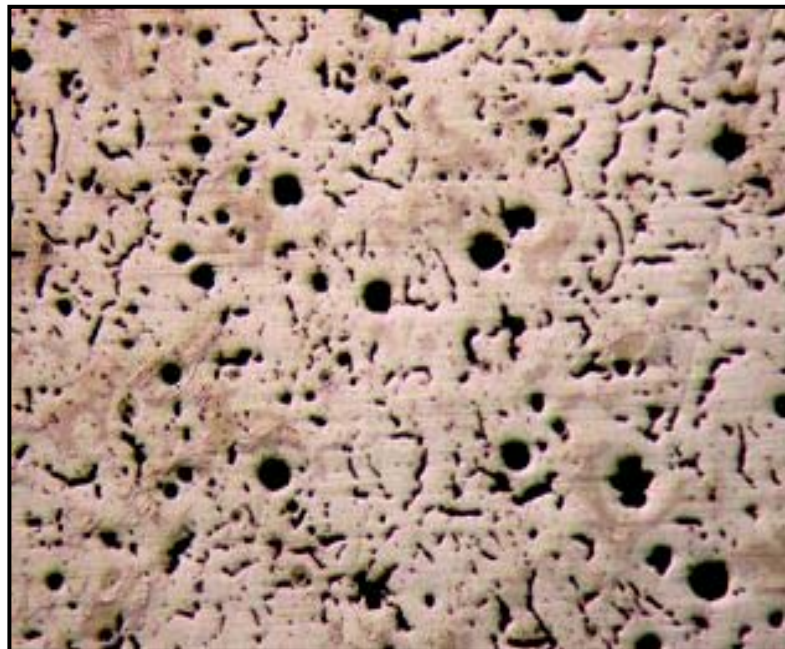


Figure 4.28 Microstructure of specimen, with 7Be code, Treated with FeSiMg, Mg/S: 5.3, Section size: 10 mm, 94.5% CG Magnification  $\times 100$ ,





Figure 4.29 Microstructure of specimen, with 7Bf code, Treated with FeSiMg, Mg/S:5.3, Section size: 20 mm, 98.6 % CG, Magnification  $\times 100$ ,

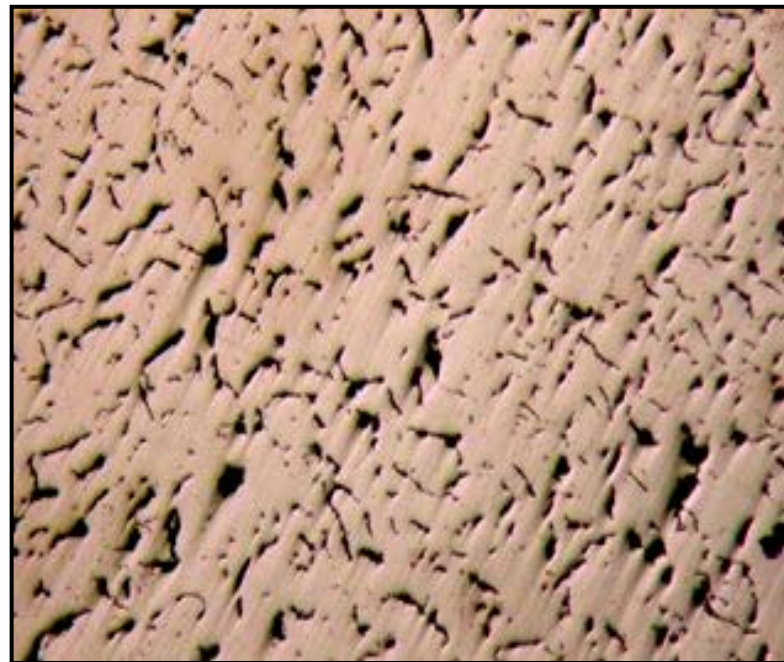


Figure 4.30 Microstructure of specimen, with 7Bg code, Treated with FeSiMg, Mg/S:5.3, Section size: 40 mm, 99.2 % CG Magnification  $\times 100$ ,

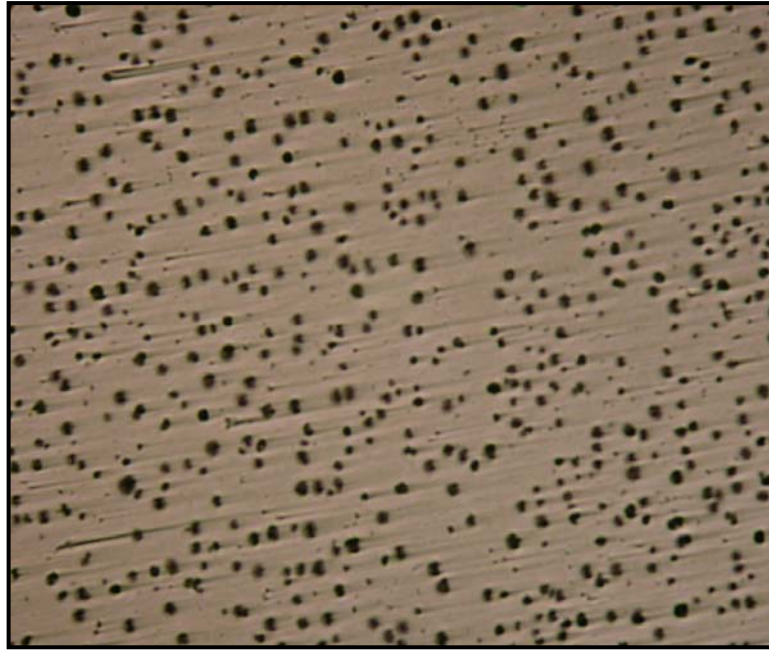


Figure 4.31 Microstructure of specimen, with 8Ad code, Treated with FeSiMg-Cermish metal, Mg/S:6.5, Section size: 5mm, 100% SG, Magnification  $\times 100$ ,

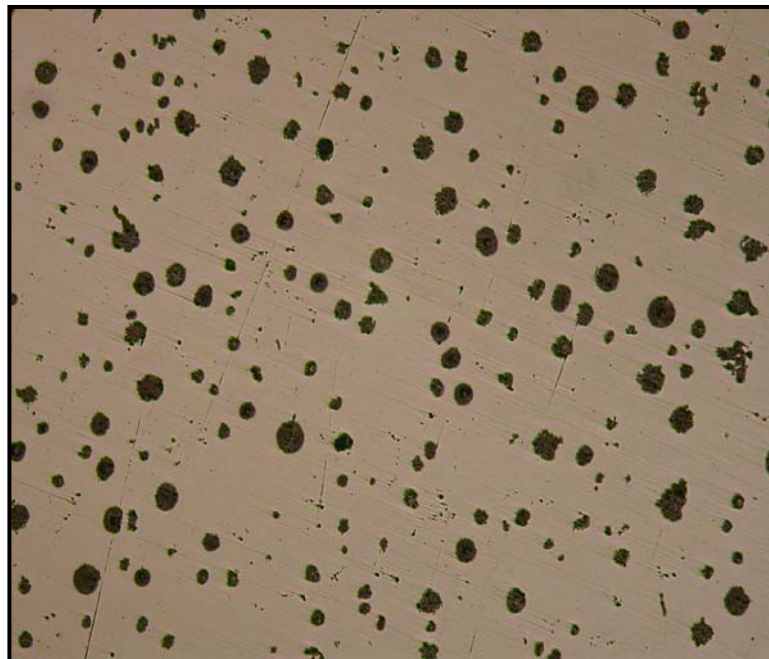


Figure 4.32 Microstructure of specimen, with 8Ae code, Treated with FeSiMg-Cermish metal, Mg/S:6.5, Section size: 10mm, 5.5 % CG, Magnification  $\times 100$ ,

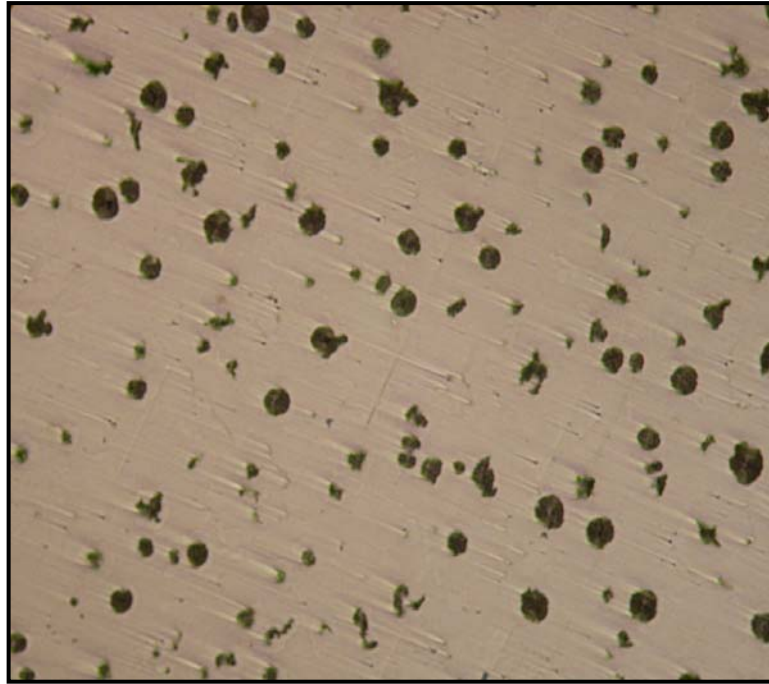


Figure 4.33 Microstructure of specimen, with 8Af code, Treated with FeSiMg-Cermish metal, Mg/S:6.5, Section size: 20 mm, 40 % CG, Magnification  $\times 100$ ,

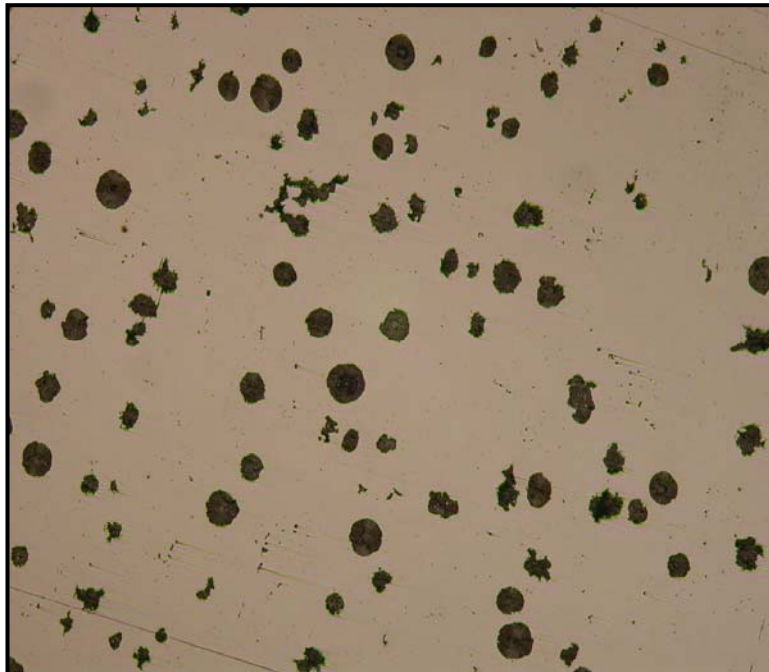


Figure 4.34 Microstructure of specimen, with 8Ag code, Treated with FeSiMg-Cermish metal, Mg/S:6.5, Section size: 40 mm, 50 % CG, Magnification  $\times 100$ ,



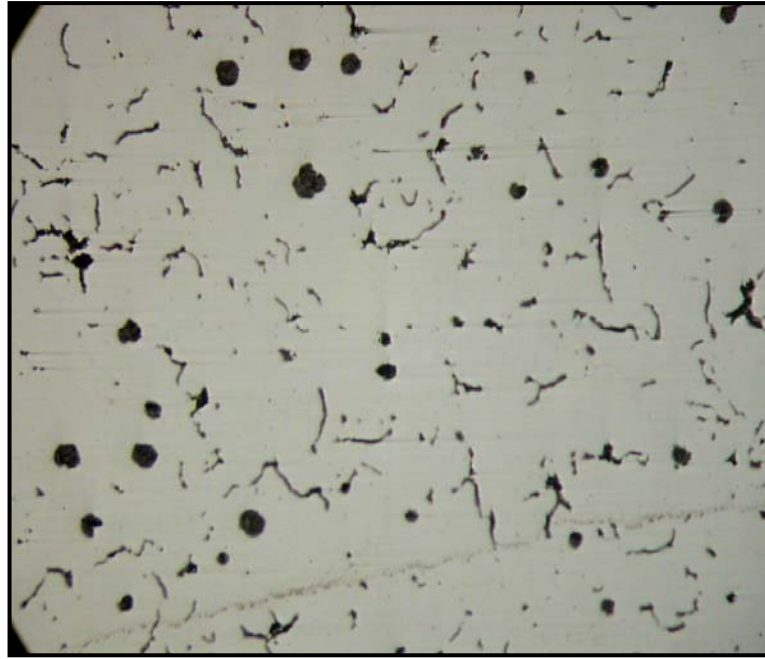


Figure 4.35 Microstructure of specimen, with 8Bd code, Treated with FeSiMg, Mg/S:6.5, Section size: 5mm, 78.9 % CG, Magnification  $\times 100$ ,

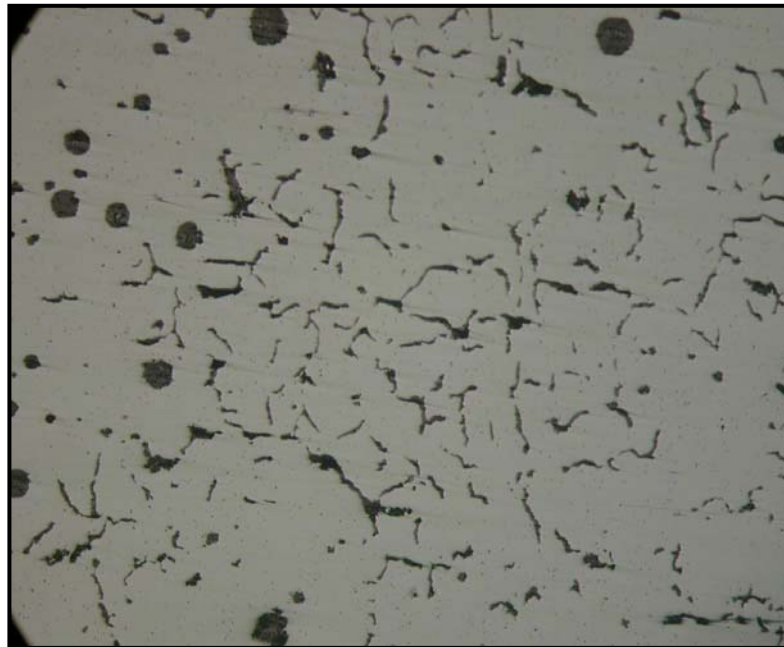


Figure 4.36 Microstructure of specimen, with 8Be code, Treated with FeSiMg, Mg/S:6.5, Section size: 10 mm, 82.7% CG, Magnification  $\times 100$ ,

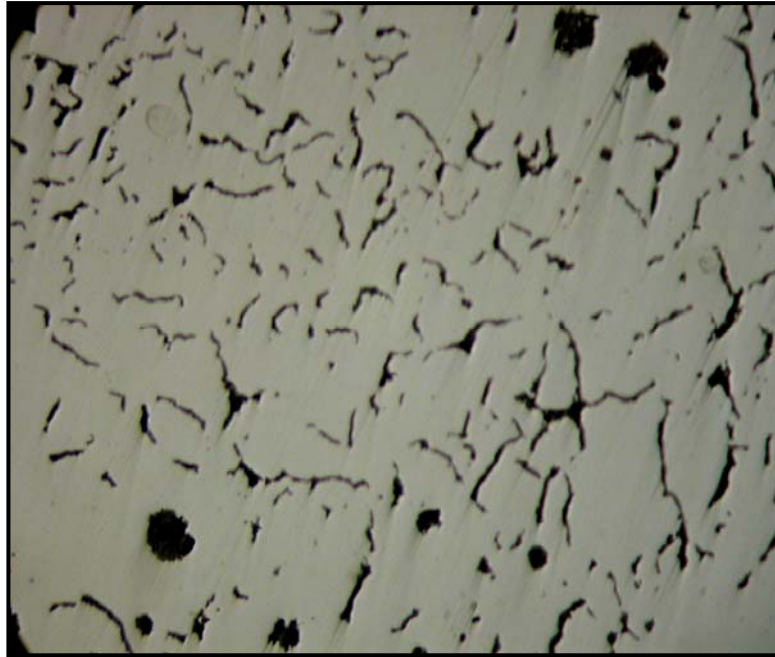


Figure 4.37 Microstructure of specimen, with 8Bf code, Treated with FeSiMg,  
Mg/S:6.5 section size: 20 mm, 96.3 % CG, Magnification  $\times 100$ ,

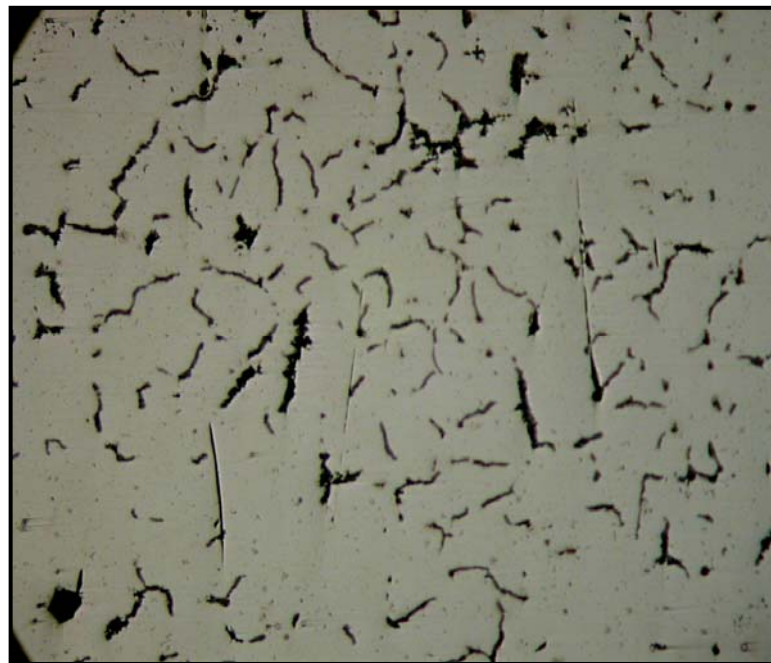


Figure 4.38 Microstructure of specimen, with 8Bg code, Treated with FeSiMg,  
Mg/S:6.5, Section size: 40 mm, 99.7 % CG, Magnification  $\times 100$ ,

## **4.2 The Effect of Oxygen Activity on the Microstructures of Cast Irons Treated with FeSiMg-Cremish Metal and with FeSiMg**

In order to investigate the effect of oxygen activity on the graphite morphology and to find a suitable oxygen activity level at which compacted graphite iron dominates in the matrix and is not sensitive to the section thickness, a stepped-block casting shown in Figure 3.1 has been produced with ten different heats having different Mg/S ratio by treating the base iron with either FeMgSi or with FeSiMg-Cermish metal.

Heat 1A was prepared according to the chemical composition shown in Table. 4.1. The shape of graphite morphology was flake graphite. Type E flake graphite as in the thinner sections, and A type in sections 30 mm to 40 mm .as shown in Figure 4.1 through 4.4

Heat 4A was obtained, in which the ratio of Mg/S is equal to 2, and with the chemical composition shown in the Table.4.2. The oxygen activity for this trial was measured as 0.7756 ppm and the EMF was -183.5 mV. The type of graphite morphology was again flake graphite. Figures 4.5, 4.6, 4.7, and 4.8 show the microphotographs of sections varying from 5 mm to 40 mm; this is reflecting the fact that, the oxygen activity should be reduced more and the Mg percentage to reduce oxygen activity should be increased.

Another heat was made, heat 4B, with the chemical composition shown in Table. 4.3. The oxygen activity was measured as 0.7766 ppm, and the EMF was -183.9 mV. The type of graphite was flake graphite. Figures 4.9, 4.10, 4.11 and 4.12 show the microphotographs of sections varying from 5 mm to 40 mm. This gave us an indication that we have to reduce the oxygen activity more by increasing the spheroidizing elements.

As a result of the previous heats, the spheroidizing potential was increased and heat 5A was prepared made with the chemical composition shown in Table.4.4. This further increase in Mg/S gives rise to graphite shape in the matrix tending to be changed to spheroidal in thin section and compacted in medium and large sections. Figures 4.13 through 4.16 show the microstructures of sections varying from 5 mm to 40 mm. The oxygen activity for this heat was 0.2562 ppm and the EMF was – 245.1 mV which means that this level of oxygen activity is suitable for producing compacted graphite iron in section of 10 mm to 40 mm.

The previous spheroidizing potential was repeated, and heat 5B with the chemical composition shown in Table 4.5. Figures 4.17 through 4.20 show the microstructures of sections varying from 5 mm to 40 mm.

The graphite growth mode was again spheroidal in thin section and compacted in medium and large sections. The oxygen activity for this trial was measured as 0.3903 ppm and the EMF was -235.3 mV. This means that, with this level of oxygen activity we can also produce compacted graphite iron at medium and large section by using FeSiMg as treatment material.

Heat 6B is a special heat performed to specify the required level of oxygen activity to produce compacted graphite iron and to also investigate the effect of treatment time on that final graphite shape. The oxygen activity of the molten metal of this heat was further reduced to 0.2396 ppm or and with EMF -255.9 mV by the chemical composition shown Table 4.6. A 20 mm thick casting was produced with two different treatment times, the first treatment time was 9 minute and the second one was 14 minute, the microstructure of this heats are shown in Figure 4.21 and Figure 4.22 respectively .

It's clear that, this level of oxygen activity is suitable for producing compacted graphite iron at 20 mm section thickness at 9 minute treatment time, but it not suitable for if the treatment time is increased to 14 minute, therefore, the treatment time should be considered to evaluate the suitable oxygen activity for producing compacted graphite iron.

Heat 6A was obtained, in which the ratio of Mg/S is equal to 4.6, and with the chemical composition shown in the Table.4.7. In this experiment, the oxygen activity was 0.082 ppm and the EMF was -319.3 mV. Figures 4.23, 4.24, 4.25, and 4.26 show the microphotographs of sections varying from 5 mm to 40 mm. Compacted graphite dominates in the medium and large thickness section, however, in the thinnest section spheroidal graphite is still appears .



At higher reduction of oxygen activity, the oxygen activity being 0.1975 ppm and the EMF being -266.8 mV, heat 7B was attained with the chemical composition shown in Table 4.8. the graphite type was spheroidal in thin section and compacted in medium and large sections. Figures 4.27 through 4.30 show the microstructures of sections varying from 5 mm to 40 mm. It means that, this level of oxygen activity could be included to the suitable level for producing compacted graphite iron in medium and large section.

Having the chemical composition shown in Table 4.8, heat 8A was carried out which results in reducing the oxygen to 0.0596 ppm or 3373.4 mV EMF. In this heat the spheroidal graphite shape dominates in all sections. Figures 4.31 through 4.34 show the microstructures of sections varying from 5 mm to 40 mm. This means that, this level of oxygen activity is not suitable to produce compacted graphite shape in small or in large sections.

Heat 8B was carried out, with the composition shown in Table 4.10, by using FeSiMg as a treatment material, the oxygen activity was reduced to 0.2396 ppm or to -278 mV EMF. The graphite shapes which were attained at section size varying from 5 mm to 40 mm are shown in Figure 4.35 through 4.38.

In the small section, 5 mm, the spheroid graphite still appears, however in the other sections, the compacted graphite irons dominates in the matrix. This means that by this level of oxygen activity is suitable to produce compacted graphite morphology in medium and large section size.

Two different treatments material were used, FeSiMg-Cermish metal and FeSiMg, it was observed that, using FeSiMg-Cermish metal as a treatment material to produce compacted graphite iron reduces the oxygen activity more than FeSiMg .

The reason for that is due to existence of both Mg and Ce as nodulizing elements in FeSiMg-Cermish, while in the FeSiMg only Mg is acting as nodulizing element. Figure 4.39 shows the influence of the type of treatment material on the oxygen activity.

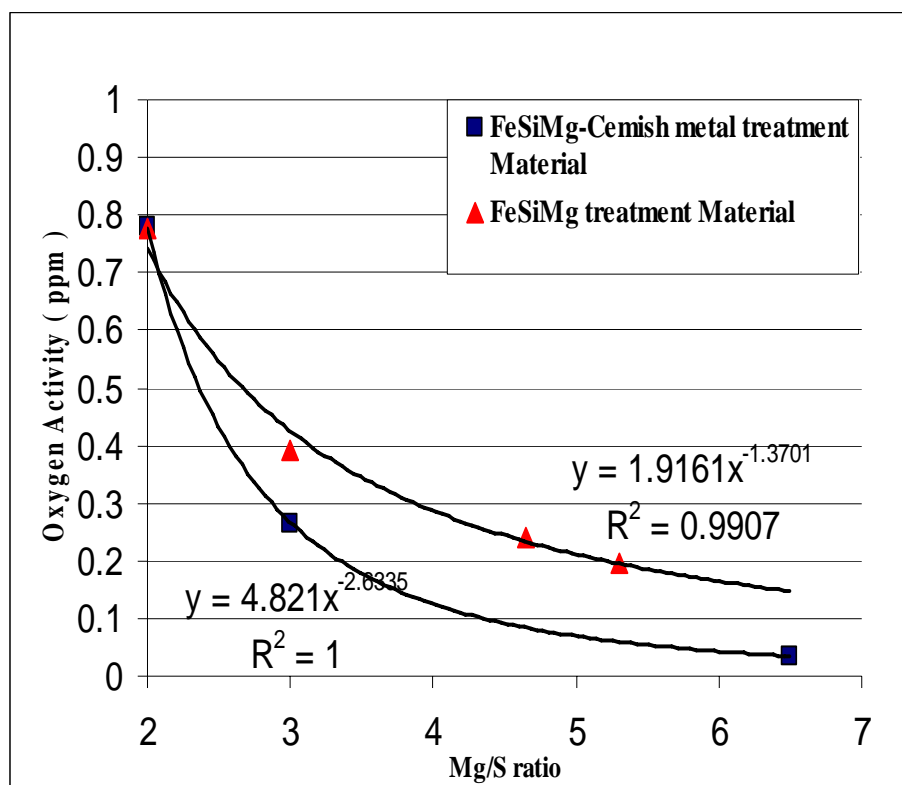


Figure 4.39 The effect of type of treatment material on the oxygen activity

After presenting the results, it could be summed as below:

1. High level of oxygen activity results in producing flake graphite and low level results in ductile iron. The level of oxygen activity required to produce compacted graphite iron is in between that ratio of flake graphite and ductile iron.

In this study, the range of this level of oxygen activity is from 0. 2030 ppm to 0.0203 ppm and other chemical composition should be in the following range of 3.0-4.0 %C, 2.0-2.8%Si, 0.018% max. S.

2. Oxygen activity level necessary to produce compacted irons is very critical and is difficult to be controlled; the reason is that, this level is highly sensitive to the liquid alloy temperature. Increasing the melt temperature will increase the oxygen level.

3. Measuring the oxygen activity is an essential method to evaluate cast iron melts and to increase the reliability of the compacted graphite cast iron production process.

4. The treatment material which contained more nodulizing elements results in reduction of oxygen activity more than that which contain less nodulizing elements, therefore the type of treatment material is also an important variable affecting the formation of the graphite shape

### 4.3 The Relationship between Microstructure and Cooling Curves

The solidification of compacted graphite iron is a function of many factors, such as, the solidification rate, (section size of casting), chemical composition of the base materials, and the amount of nodulizing elements (105). In this section, by using Multi-Lab Quik-Cup device, the cooling curves obtained during solidification were investigated and the critical temperatures were analyzed.

Heat 1A was prepared with the chemical composition shown in the Table. 4.1. In this heat, the graphite growth was in the form of lamellar graphite in thin section, and type E flake graphite was observed in the thinner section, and as section gets thicker, in sections 30 mm to 40 mm, A type was observed, as shown in Figure 4.1 through 4.4. The cooling curve of this heat is shown in Figure 4.38. The under cooling,  $\Delta T$ , of this heat was  $-6^{\circ}\text{C}$  with a recalescence of  $8.5^{\circ}\text{C}$ .

In the heat 4A, the cooling curve shown in Figure 4.41, the undercooling  $\Delta T$  and the recalescence were equal to  $-2.4$  and  $8.6^{\circ}\text{C}$  respectively with by the chemical composition shown in the Table. 4.2. The type of graphite morphology was again in the form of flake graphite iron. Figures 4.5, 4.6, 4.7, and 4.8 show the microphotographs of sections varying from 5 mm to 40 mm; this is reflecting the fact that, neither  $\Delta T$  nor recalescence is suitable for production of compacted graphite iron.

Another heat was made, heat 4B, with the chemical composition shown in Table. 4.3. The cooling curve for this heat is shown in Figure 4.42, it's  $\Delta T$  was  $-9.6^{\circ}\text{C}$ , and the recalescence was  $5.4^{\circ}\text{C}$ . In this heat, the type of graphite was type A flake graphite. Figures 4.9, 4.10, 4.11 and 4.12 show the microphotographs of sections varying from 5 mm to 40 mm. This gave us an indication that we have to increase  $\Delta T$  more by increasing the spheroidizing elements.

As a result of the pervious heat, the undercooling was increased by increasing the spheroidizing potential, and heat 5A was made with the chemical composition shown in Table. 4.4. Both the undercooling and recalescence were reduced to  $+6^{\circ}\text{C}$ , and  $7.5^{\circ}\text{C}$  respectively. Figure 4.43 shows the cooling curve of this heat, this further reduction of under cooling gives rise of graphite in the matrix tending to be changed to spheroidal in thin section and compacted in medium and large sections. Figures 4.13 through 4.16 show the microstructures of sections varying from 5 mm to 40 mm. This means that, these values of  $\Delta T$  and recalescence are suitable for producing compacted graphite iron in the 10 mm section thickness to 40 mm.

Heat 5B with the chemical composition shown in Table 4.5 and with the previous spheroidizing potential was repeated. The graphite shape was again spheroidal in thin section and compacted in medium and large sections. Figure 4.13 through 4.16 show the graphite morphology for the section size varying from 20 mm to 40 mm and Figure 4.44 shows the cooling curve of this heat.  $\Delta T$  and recalescence were calculated,  $\Delta T$  was  $+4.5^{\circ}\text{C}$  and the recalescence was  $8.2^{\circ}\text{C}$ , this means that, under the other working conditions and by this value of  $\Delta T$  and recalescence we can also

produce compacted graphite iron at medium and large sections by using FeSiMg as treatment material.

Heat 6B with the chemical composition shown Table 4.6 was carried out. A 20 mm thick casting was produced with two different treatment times, the first treatment time was 9 min and the second one was 14 min, the microstructure of this heat are shown in Figure 4.17 and Figure 4.18 respectively, and their cooling curve are shown in Figure 4.45 and Figure 4.46 respectively. The undercooling  $\Delta T$  and the recalescence for the solidified molten metal were further reduced to  $+4.8^{\circ}\text{C}$  and  $6.8^{\circ}\text{C}$  for the 9 minute treatment time; on the other hand, these values were increased to  $-12.0^{\circ}\text{C}$  and  $8^{\circ}\text{C}$  for the 14 minute treatment time. This means that, the treatment time has a significant effect on the value of undercooling and then effects the graphite morphology, therefore, under this condition of Mg/S ratio being 4.64, treatment time being 9 minute,  $\Delta T$  being  $+4.8^{\circ}\text{C}$  and recalescence being  $6.8^{\circ}\text{C}$ , the compacted graphite iron could be produced at 20mm section thickness.

Another heat, heat 6A, was carried out with the chemical composition shown in Table 4.7. Figures 4.23 through 4.26 show the microstructure of the sections varying from 5 mm to 40 mm; the cooling curve for this heat is shown in figure 4.47. The undercooling of this heat was  $+7.9^{\circ}\text{C}$  and the recalescence was  $6.9^{\circ}\text{C}$ , considering all the other condition together with this value of undercooling, the analysis of the graphite morphology gives rise to the spheroidal to be the dominate phase in graphite morphology in the smallest section, 5 mm.

However, as section gets thicker, the compacted graphite morphology increases in the matrix, short stubby and worm like with round tips, which again means that, under these conditions compacted graphite could be produced in medium and large sections.

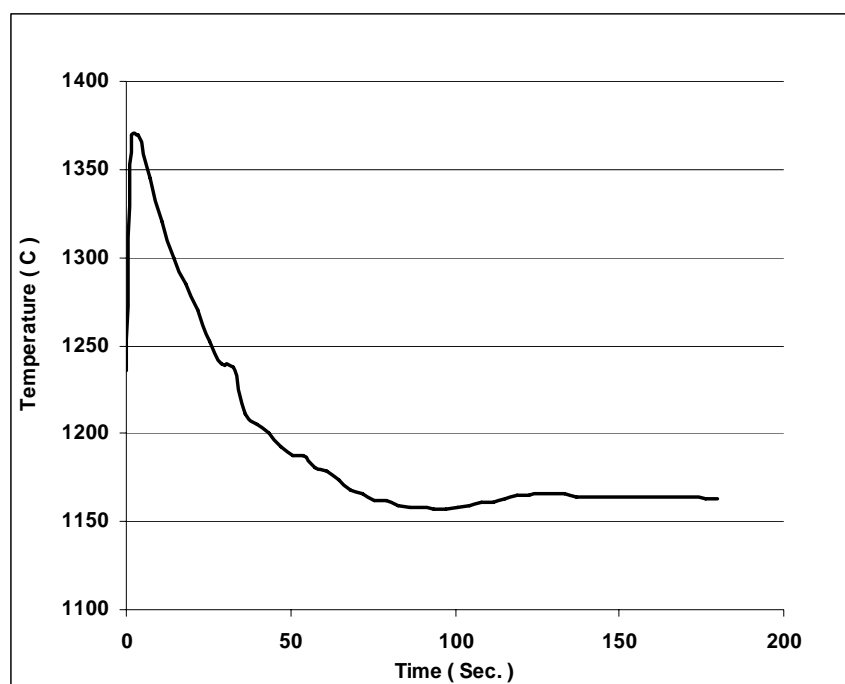


Figure 4.40 Cooling curve of heat 1A, Treated with FeSiMg-Cermish metal, Mg/S:

0.5,  $\Delta T$ : 8  $^{\circ}\text{C}$ , recalescence: 8.5

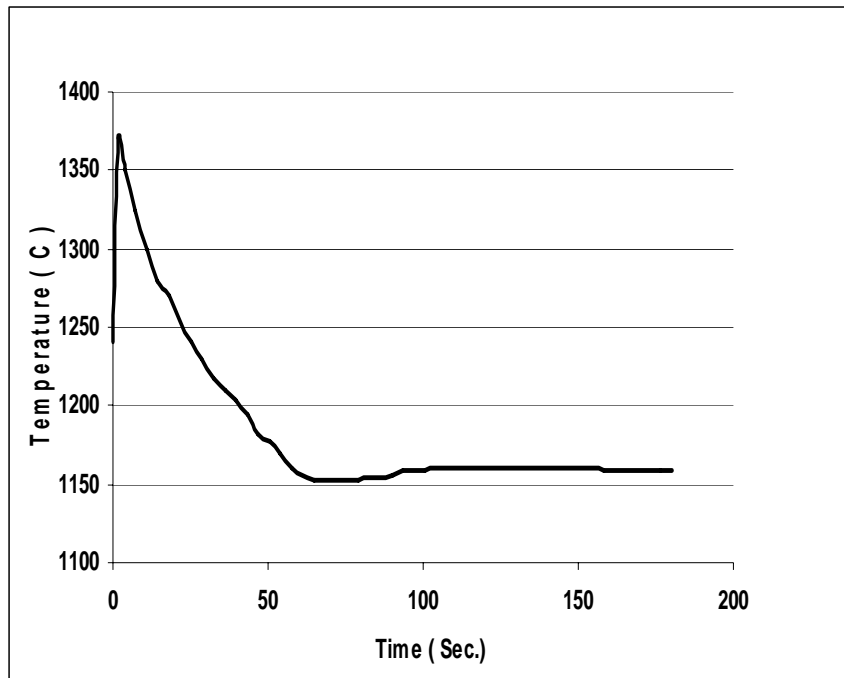


Figure 4.41 Cooling curve of heat 4A, Treated with FeSiMg-Cermish metal, Mg/S:  
0.5,  $\Delta T$ : 8 °C, recalescence: 8.5

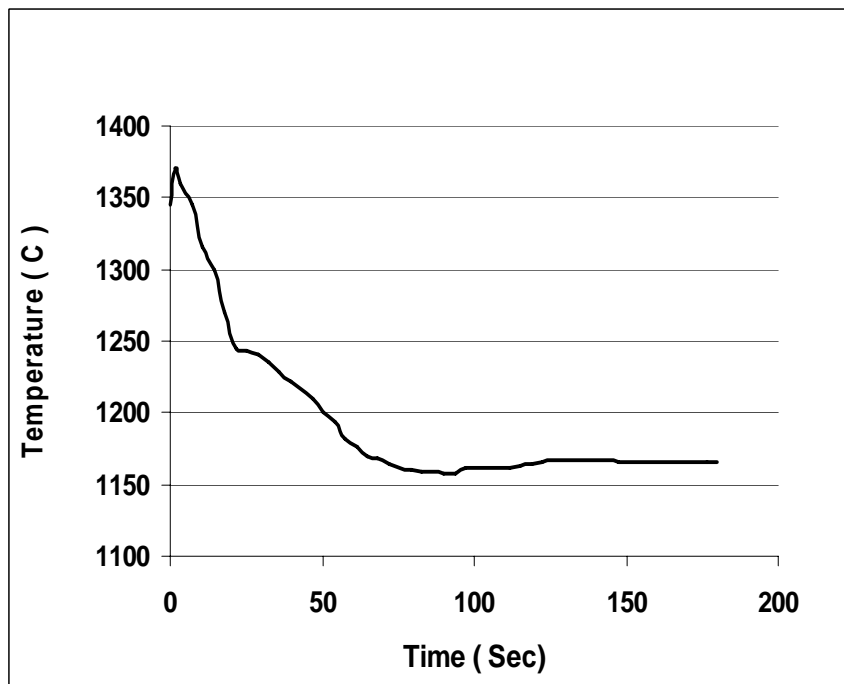


Figure 4.42 Cooling curve of heat 4B, Treated with FeSiMg, Mg/S: 2,  $\Delta T$ : 8 °C,  
recalescence: 9 °C



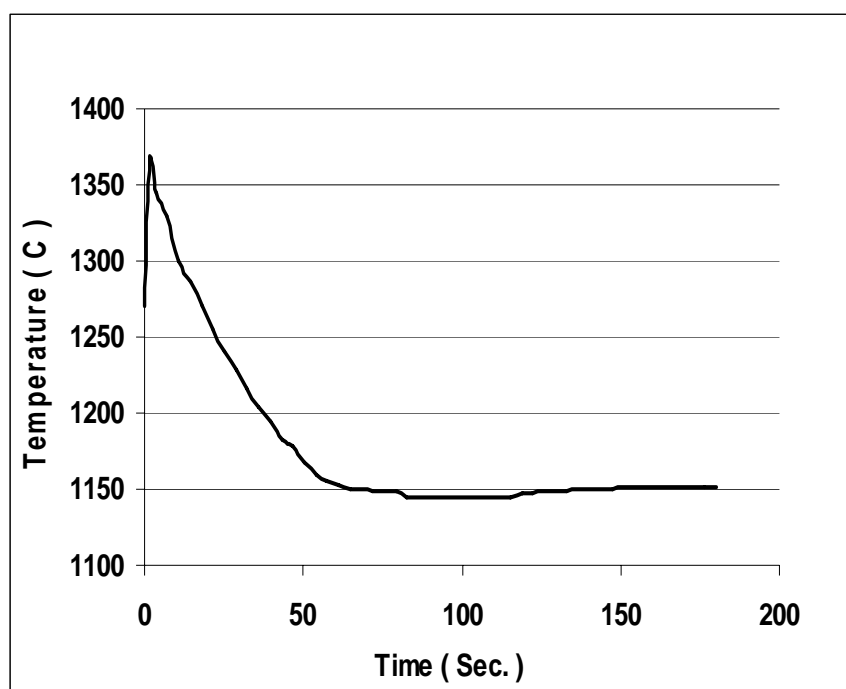


Figure 4.43 Cooling curve of heat 5A, Treated with FeSiMg-Cermish metal, Mg/S: 3,  $\Delta T$ :6  $^{\circ}\text{C}$ , recalescence: 8.5  $^{\circ}\text{C}$

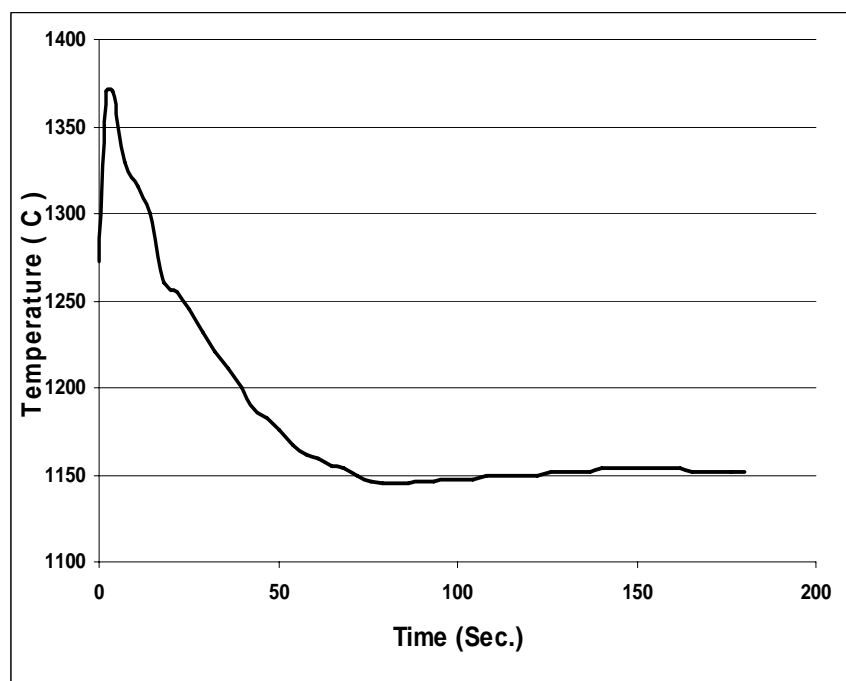


Figure 4.44 Cooling curve of heat 5B, Treated with FeSiMg, Mg/S: 3,  $\Delta T$ :4.5  $^{\circ}\text{C}$ , recalescence: 8  $^{\circ}\text{C}$

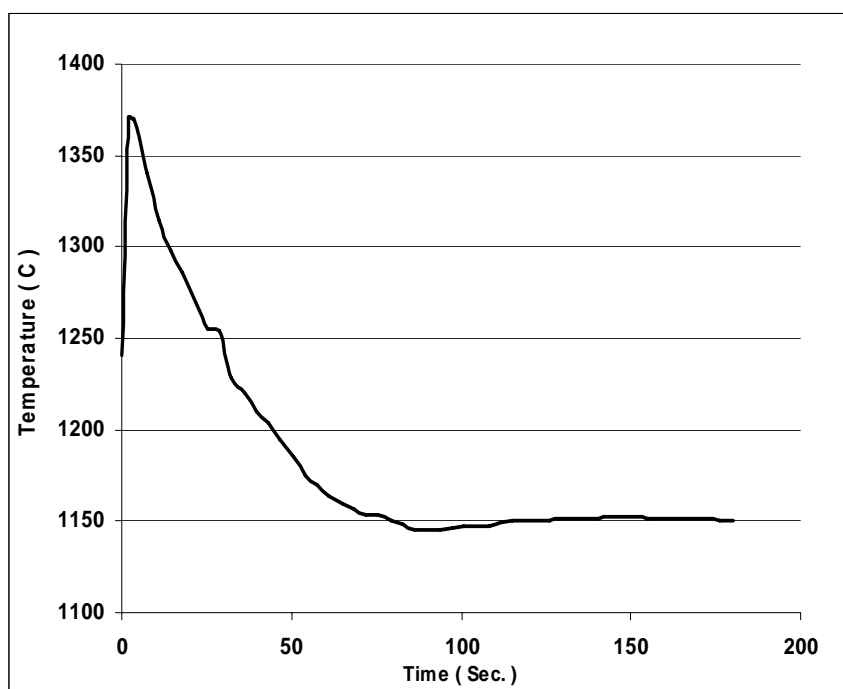


Figure 4.45. Cooling curve of heat 6B with 9 min. treatment time, Treated with FeSiMg, Mg/S: 4.46,  $\Delta T$ : 4.8  $^{\circ}\text{C}$ , recalescence: 6.8  $^{\circ}\text{C}$

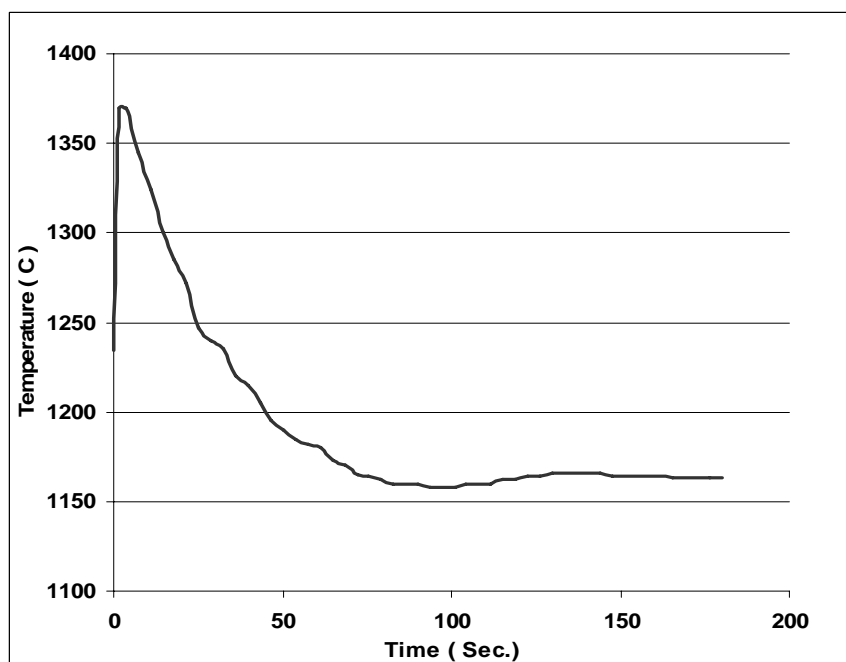


Figure 4.46. Cooling curve of heat 6B with 14 min. treatment time, Treated with FeSiMg, Mg/S: 4.46,  $\Delta T$ : -10  $^{\circ}\text{C}$ , recalescence: 8  $^{\circ}\text{C}$

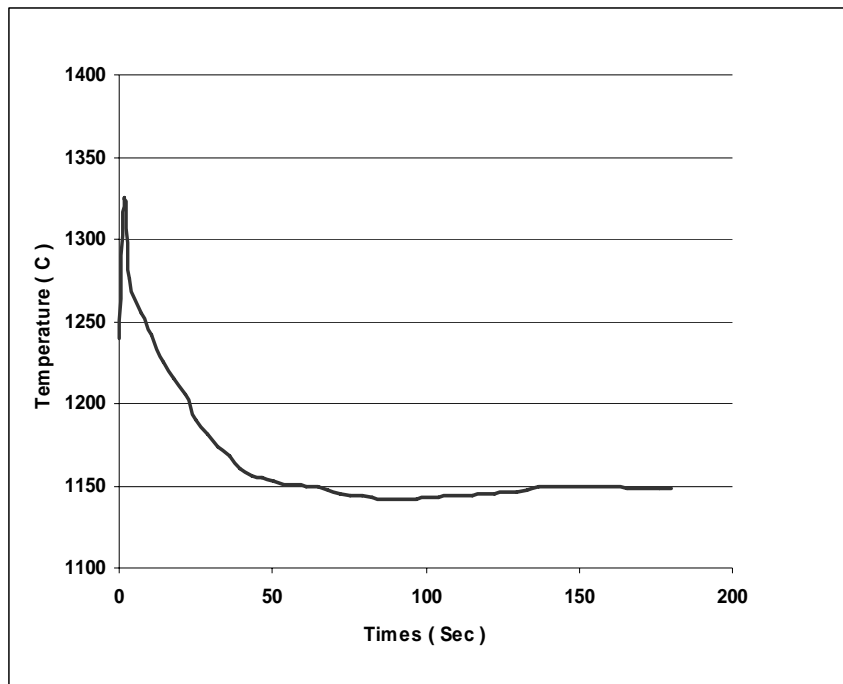


Figure 4.47 Cooling curve of heat 6A, Treated with FeSiMg-Cermish metal, Mg/S:

4.46,  $\Delta T$ : 7.9 °C, recalescence: 6.9 °C

A higher reduction of undercooling developed out with heat 7B; the chemical composition of this heat is shown in Table 4.7. The graphite form was spheroidal in thin section and compacted in medium and large sections. Figures 4.19 through 4.22 show the microstructures of sections varying from 5 mm to 40 mm, and Figure 4.48 shows the cooling curve of this heat. The value of under cooling and the recalescence of this heat were measured,  $\Delta T$  was +5 °C and the recalescence was 6 °C. It could be concluded that, these value of under cooling and recalescence are optimum values for the foundry men to produce compacted graphite iron in medium and large section.

By using the chemical composition shown in Table 4.8, heat 8A was carried out, the results show that, the value of  $\Delta T$  is further reduced to  $+16^{\circ}\text{C}$  and the recalescence was also reduced to  $4.5^{\circ}\text{C}$ . Figure 4.49 shows the cooling curve of this heat and Figures 4.23 through 4.26 show its microstructures of sections varying from 5 mm to 40 mm. In this heat, the spheroidal graphite form dominates in all sections. This means that this level of  $\Delta T$  and the recalescence are not suitable to produce compacted graphite iron.

Heat 8B was done with the chemical composition shown in Table 4.10, Mg/S ratio being 6.5, Figure 4.48 shows the cooling curve for this heat,  $\Delta T$ , the under cooling equal to  $+5.3^{\circ}\text{C}$  and the value of recalescence equal to  $6.7^{\circ}\text{C}$ , and Figures 4.35, 4.36, 4.37, and 4.38 show the microstructures of the section varying from 5 mm to 40 mm. In section size 5 mm and section size 10 mm, there is spheroidal graphite in the matrix, however, in the other sections, 20 and 40 mm which are shown in Figure 4.37 and 4.38 respectively the compacted graphite dominates in the iron matrix.

It is clear from the previous calculation of  $\Delta T$  and the investigation of microstructure that, there is strong relation between the undercooling of the solidified molten iron and the graphite morphology of the cast iron, the negative value of undercooling, will lead to flake graphite formation, on the other hand., higher value of undercooling, higher than or equal to  $+16.0^{\circ}\text{C}$ , by using of FeSiMg-Cermish metal, will result in ductile iron formation. The level of  $\Delta T$  to produce compacted graphite iron should be in between of those of flake graphite iron and those of ductile iron.

Also from the cooling curves, it can be seen that, the recalescence is increasing as the nodularity is decreasing. Also, when FeMgSi or FeMgSi-Cemish metal was used as a treatment material, the recalescence was increased as the nodularity decreased. Figure 4.49 and 4.50 show how the recalescence is increased when the Mg/S ratio is decreased.

In sum, the analysis of these cooling curves and the microstructures for each group are shown in Table 4.11. The variation of the undercooling of each type of graphite could be explained based on the mechanism of compacted graphite formation, it was concluded that, at low level of Mg/S ratio, the presence of free oxygen and sulfur in the melt produces a nonfaceted graphite face. The nonfaceted prism is highly mobile and the carbon atoms are added primarily to this face without much undercooling. On the other hand high level of Mg/S ratio ties up the free oxygen and sulfur which causes the formations of faceted prism, and high undercooling is required for the carbon atoms to be added to this face. Compacted graphite can be considered as a transition product between flakes and spheroid. In addition, there is a strong correlation between the microstructures of the step blocks specimens with both the undercooling and the recalescence in the cooling curves.

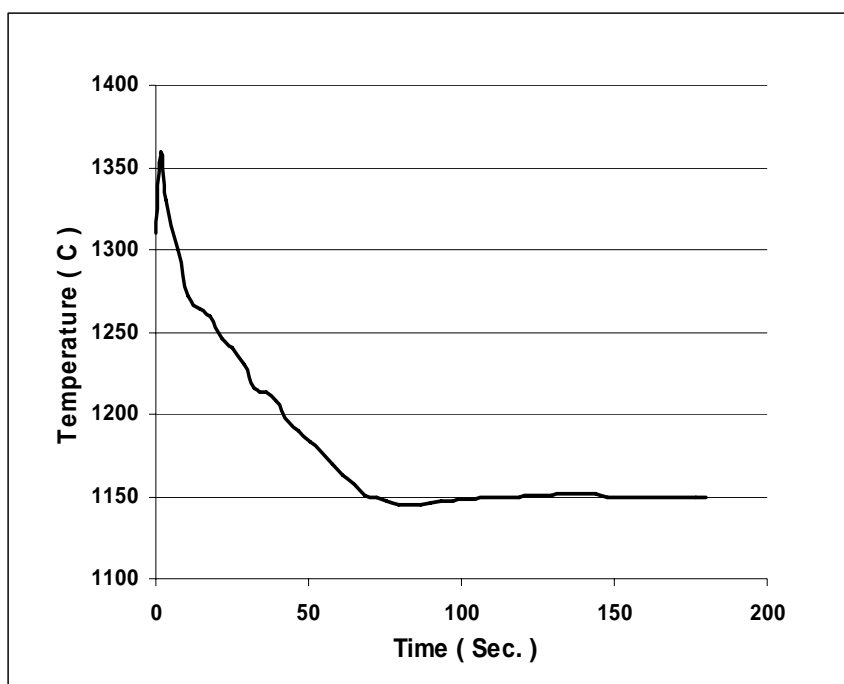


Figure 4.48 Cooling curve of heat 7B, Treated with FeSiMg, Mg/S: 5.30,  $\Delta T$ : 5 °C, recalescence: 7 °C

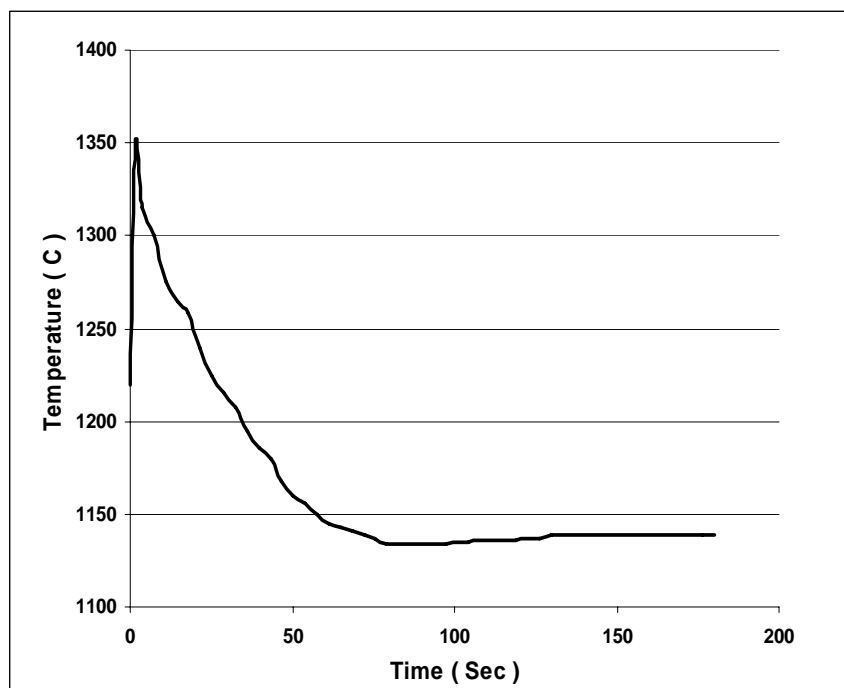


Figure 4.49 Cooling curve of heat 8A, Treated with FeSiMg-Cermish metal, Mg/S: 6.30,  $\Delta T$ : 16 °C, recalescence: 4.5 °C

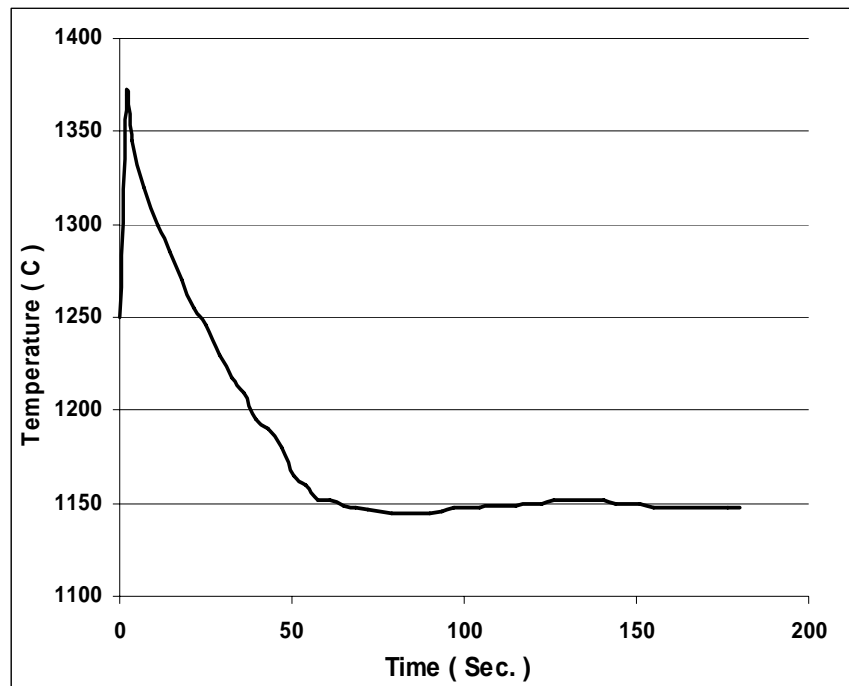


Figure 4.50 Cooling curve of heat 8B, Treated with FeSiMg, Mg/S: 6.3,  $\Delta T$ : 5.30 °C,  
recalcsence: 6.7 °C

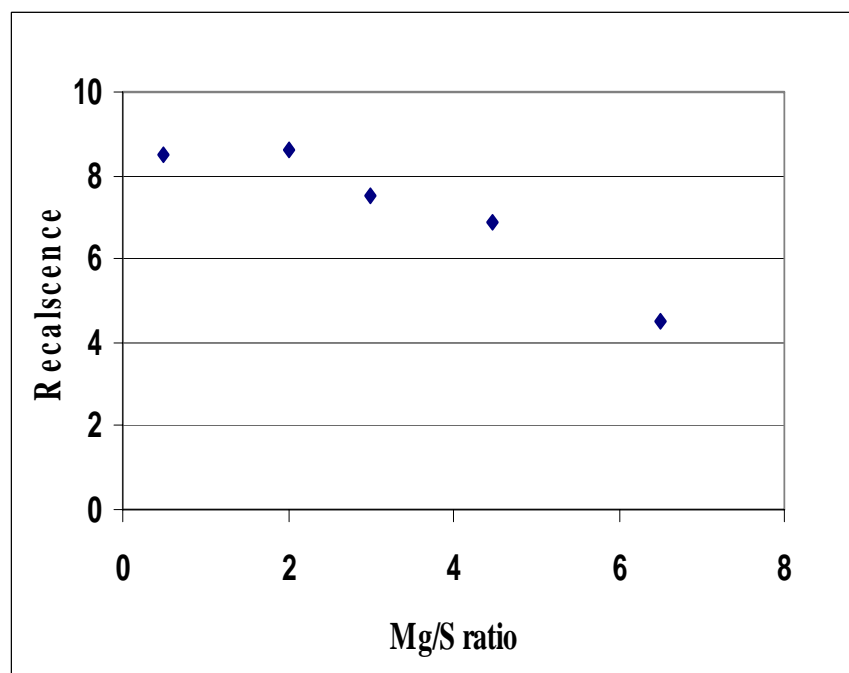


Figure 4.51. The effect Mg/S ratio of group A treatment material on the recalcsence

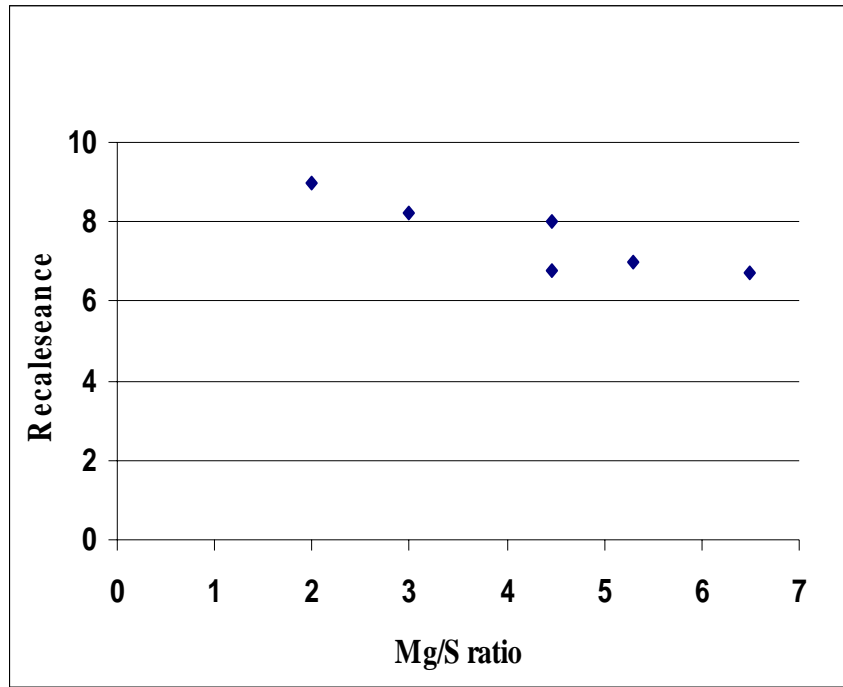


Figure 4.52. The effect of Mg/S ratio of group B treatment material on the recalescence

Table 4 .11 Heat code, recalescence, undercooling and graphite form

Heat Code	Recalescence	$\Delta T$	Graphite form
1A	8.5	-8	FGI
4A	6.9	-2.4	FGI
4B	9	-8	FGI
5A	7.5	6	SGI and CGI
5B	8.2	4.5	SGI and CGI
6B1	6.9	4.8	CGI
6B2	8	-10	FGI
6A	6.9	7.9	SGI and CGI
7B	7	5	SGI and CGI
8A	4.5	16	SGI
8B	6.7	5.3	SGI and CGI



In sum, the larger the undercooling,  $\Delta T$  being greater than or equal to +16 °C, the higher the chance to get spheroidal graphite iron, on the other hand, the smaller the under cooling,  $\Delta T$  being positive, the higher possibility to get flake graphite.

The undercooling for compacted graphite iron has a value between those of spheroidal and flake graphite i.e., the  $\Delta T$  range is +4.5 to +8 °C. Decreasing recalescence is a good indication of the nodularity.

The type of treatment material being used is also has an effect on the behavior of the cooling curve, i.e. the treatment material which contains more spheroidizing elements can increase the undercooling more than materials containing few spheroidizing elements Moreover, it was observed that, using FeSiMg-Cermish results in reducing the under cooling more than FeSiMg treatment alloy.

#### **4.4 The Effect of Graphite Morphology and Iron Matrix on the Tensile Strength**

Due to the fact that the combined effect of graphite morphology and matrix structure on tensile strength is one of the most important variables for engineering applications of compacted graphite iron, therefore, the effect of graphite morphology and matrix structure on the tensile properties is discussed below.

For all heats the tensile test bars were produced and tensile tests were preformed. The alloying elements which are affecting the graphite morphology, such as magnesium sulfur and copper, were considered to investigate their on tensile strength. In all heats the iron matrix was controlled by the addition of copper to get pearlitic matrix.

Table 4.12 shows effect of Mg/S ratio and hence the graphite morphology on tensile strength of the heat treated alloys either by FeSiMgCermish metal or FeSiMg.

It was also observed that, there is direct relation between the Mg/S ratio and the tensile strength, this is due to the effect of Mg/S on the graphite morphology which controls the tensile strength. As it was explained previously, there are specific ranges in which the different types of graphite type could be obtained. Therefore, the range of Mg/S ratio in which the spheroidal shape of graphite is presented shows the highest value of tensile strength.

Moreover, the type of treatment material is also an important factor affecting the tensile strength. Using treatment material which contains more nodulizing elements in its composition results in higher tensile strength. This is due to the increasing number of the spheroidal graphite in the matrix where the compacted graphite is dominant.

In the highest ratio of Mg/S, Mg/S being 6.5, there was significance difference in the tensile strength, that's due to the difference in the graphite morphology which was completely spheroidizing in the cases of using FeSiMg-Cermish metal and compacted graphite in the case of using only FeSiMg as treatment material. Figure 4.52 shows the relationships between the Mg/S ration and the tensile strength for each type of treatment material.

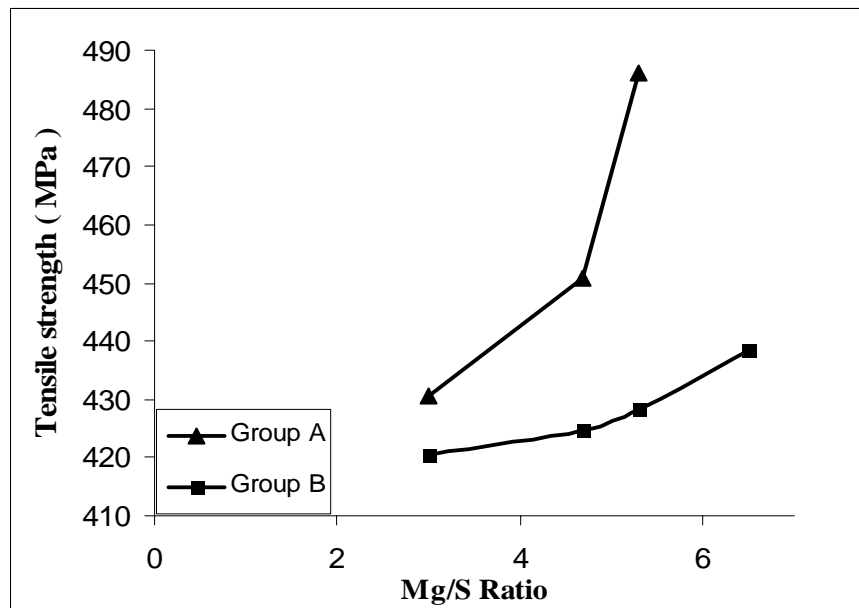


Figure 4.53 The relationship between the Mg/S ration and the tensile strength for each type of treatment material

Table 4.12 Tensile test and matrix structures results

Trial code	UTS(MPa)	Matrix structures
1A	-	-
4A	123.9	-
5A	430.4	Pearlitic
6A	450.7	Pearlitic
8A	797.8	Pearlitic
4B	111.2	-
5B	420.5	Pearlitic
6B	424.6	Pearlitic
7B	428.2	Pearlitic
8B	Pearlitic	

It was observed that, flake graphite showed the lowest tensile strength value, this is due to the needle shape in which the stress concentration is the highest among the other types of the graphite. The value of tensile strength was the highest in ductile iron, this because of the sphere shape of graphite in which the stress concentration is in the lowest value. Compacted graphite iron showed an intermediate value of tensile strength between those of flake and ductile iron.

#### **4.5 Electrical Resistance and Thermal Conductivity Measurements at Elevated Temperatures**

With the purpose of attainment of high temperature strength and high thermal conductivity, the essential property for the exhaust manifolds, the producers continue with their effort in the development of material in which those properties are achieved simultaneously. First, ductile iron was the choice for the manifolds. However, this type of cast iron requires tighter control in the foundry to minimize the production defects such as casting cold shuts, misruns and undesirable carbide formation. Therefore, compacted graphite iron was a suitable alternative while it did not show localized distortion. Thus, the worldwide production of compacted graphite cast iron has been significantly increased to be used in the production of automotive parts such as, exhaust manifold, break drums and discs.

Thermal conductivity is a structure sensitive and varies with graphite shape and temperature. Therefore, in order to qualify the effects of these factors on the thermal conductivity, the samples from heats 4A, 6A and 8A, in which the graphite shapes

are flake, compacted and ductile respectively, has been selected for the analysis, based on measuring the electrical resistance against temperature.

As it was stated previously in chapter three, the temperature range is from room temperature to 500 °C. The 500 °C temperatures was selected because it has some significance in that, the surface temperature of components like piston rings and exhaust manifolds are expected to be around 500 °C.

The measured electrical resistance against temperature for the specimens of 4A, 6A and 8A is presented in Table 4.13 through 4.15 and Figures 4.52, 4.53 and Figure 4.54 show the thermal conductivity estimated by Wiedemann – Franze – Lorange law.

Table 4.13. The electrical resistance of 4Ad, e, f and g.

Temperature ( K )	Electrical Resistance $\times 10^{-3}$ of 1Ad ( $\Omega$ )	Electrical Resistance $\times 10^{-3}$ of 1Ae ( $\Omega$ )	Electrical Resistance $\times 10^{-3}$ of 1Af ( $\Omega$ )	Electrical Resistance $\times 10^{-3}$ of 1Ag ( $\Omega$ )
298	0.119	0.121	0.123	0.125
323	0.128	0.13	0.135	0.136
373	0.154	0.152	0.156	0.158
423	0.173	0.176	0.176	0.180
473	0.193	0.197	0.199	0.204
523	0.216	0.218	0.221	0.223
573	0.238	0.241	0.246	0.251
623	0.258	0.264	0.266	0.272
673	0.281	0.286	0.289	0.295
723	0.296	0.304	0.312	0.316
773	0.322	0.328	0.334	0.338

Table 4.14. The electrical resistance of 6Ad, e, f and g.

Temperature ( K )	Electrical Resistance $\times 10^{-3}$ of 2Ad ( $\Omega$ )	Electrical Resistance $\times 10^{-3}$ of 2Ae ( $\Omega$ )	Electrical Resistance $\times 10^{-3}$ of 2Af ( $\Omega$ )	Electrical Resistance $\times 10^{-3}$ of 2Ag ( $\Omega$ )
298	0.199	0.171	0.168	0.161
323	0.215	0.185	0.181	0.175
373	0.235	0.211	0.209	0.200
423	0,28	0.241	0.234	0.229
473	0.311	0.266	0.264	0.255
523	0.333	0.292	0.289	0.280
573	0.373	0.319	0.316	0.306
623	0.408	0.348	0.341	0.335
673	0.428	0.371	0.366	0.360
723	0.457	0.400	0.392	0.384
773	0.516	0.425	0.422	0.410

Table 4.15 .The electrical resistance of 8Ad, e, f and g.

Temperature ( K )	Electrical Resistance $\times 10^{-3}$ of 3Ad ( $\Omega$ )	Electrical Resistance $\times 10^{-3}$ of 3Ae ( $\Omega$ )	Electrical Resistance $\times 10^{-3}$ of 3Af ( $\Omega$ )	Electrical Resistance $\times 10^{-3}$ of 3Ag ( $\Omega$ )
298				
323	0. 204	0. 203	0, 201	0. 195
373	0. 234	0. 233	0, 23	0. 222
423	0. 264	0. 266	0. 257	0. 253
473	0. 294	0. 292	0. 289	0. 279
523	0. 321	0. 321	0. 316	0. 308
573	0. 355	0. 351	0. 347	0. 338
623	0. 383	0. 375	0. 377	0. 365
673	0. 414	0. 41	0. 404	0. 395
723	0. 441	0. 438	0. 430	0. 422
773	0. 467	0. 461	0. 457	0. 447

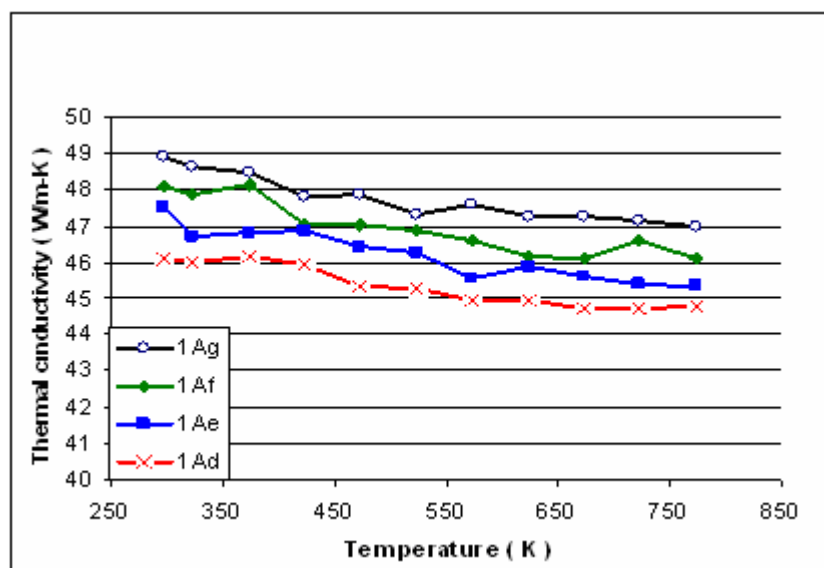


Figure 4.54 Variation of thermal conductivity of 4Ad, e, f and g with temperature

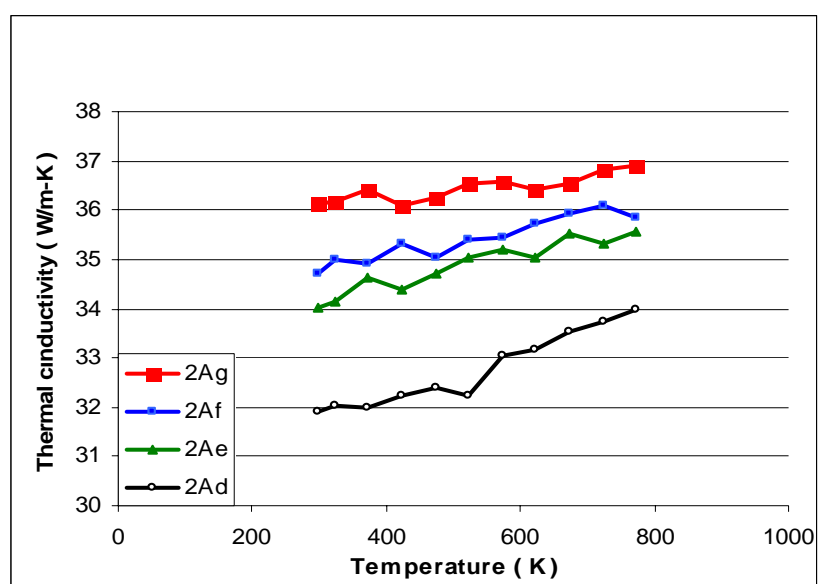


Figure 4.55 Variation of thermal conductivity of 6Ad, e, f and g with temperature

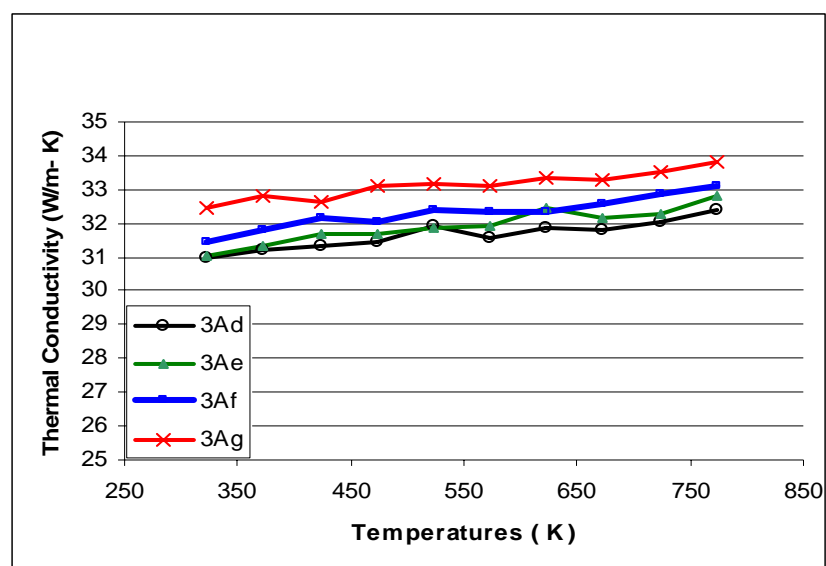


Figure 4.56 Variation of thermal conductivity of 3Ad, e, f and g with temperature

After presenting the results, it is seen that there is a good agreement between these results with the results reported in the literatures (107,108,109,110), Moreover; graphite crystallizes in a hexagonal structure. It exhibits anisotropic thermal properties; the thermal property parallel to the basal sheet is 100 times more than that perpendicular to the basal sheet (0.6 vs 0.006 cal.cm /C.cm s, respectively). Flake graphite is characterized by the predominance of growth on the prism faces, where as spheroidal graphite characterized by spiral growth on the basal face. Compacted graphite can be considered as a transition product between flakes and spheroid. However, the small variations can be attributed to the contact problem between the samples and the thermocouples. This contact is becoming weak especially at high temperatures resulting in increasing the electrical resistance and then decreasing the thermal conductivity, consequently the following points



could be concluded.

1. The flake cast iron has the highest thermal conductivity followed by compacted cast iron; ductile cast iron exhibits the lowest thermal conductivity.
2. Avoiding high nodularity in compacted graphite iron is critical and crucial, especially in the application in which the thermal conductivity plays an effective role.
3. The existence of flake graphite within the compacted graphite cast iron affects the thermal conductivity positively.

#### 4.6 Regression Analysis

The multiple regression analysis models is simply a correlation between the main characteristics of compacted graphite, the tensile strength and thermal conductivity, with the main production processes variables required to produce compacted graphite iron, the Mg/S ratio, undercooling, and oxygen activity. Table 4.16 shows those variables with the corresponding properties.

Table 4.16 Thermal conductivity, tensile strength, Mg/S ratio, undercooling and oxygen activity required to produce compacted graphite cast iron.

Thermal conductivity (W/m K)	Tensile strength (MPa)	Mg/S Ratio	Undercooling °C-	Oxygen activity ( ppm )
37.4	430.4	3	-6	0.2667
35.06	450.7	4.64	-7.9	0.0827
39.87	420.5	3	-4.5	0.3963
36.8	424.6	4.64	-4.8	0.2396
39.43	428.2	5.3	-5	0.1975
38.55	438.2	6.5	-5.3	0.148

In this study, the excel software with 95% confidence level was employed for this analyzing both characteristics with their variables.

#### 4.6.1. Multiple Regression Model for Tensile strength

From the over all analysis of regression study, the following model was attained to predict the tensile strength based on the Mg/S ratio, undercooling and oxygen activity.

$$\sigma_f = 312.97 + 7.34 \text{ Mg/S} + 12.37 \Delta T + 76.08 \underline{Q} \quad (4.1)$$

Where  $\sigma_f$  is tensile strength in (MPa), Mg/S is the magnesium to sulfur ration,  $\Delta T$  is Undercooling (in  $^{\circ}\text{C}$ ) and  $\underline{Q}$  is oxygen activity (in ppm). The detailed parameters list is given in Table 4.17 and Table 4.18 displays the predicted tensile strength obtained from the estimated parameters.

Table 4.17 Linear regression parameters estimated for tensile strength

	Coefficients
Intercept	312.97
Mg/S ratio	7.34
$\Delta T$ Undercooling	12.37
Oxygen activity	76.08

Table 4.18 The predicted tensile strength obtained from the estimated parameters.

Observation	Predicted tensile strength (MPa)
1	429.56
2	451.12
3	420.85
4	424.68
5	428.80
6	437.56

From table 4.17 and 4.18, we observed that, the intercept is 312.97. This means the tensile strength when all the independent variables are equal to zero. Multiple R was 0.99 which means that, this model is good in representing between the tensile strength and the variables

#### 4.6.2. Multiple Regression Model for Thermal Conductivity

The regression model obtained for the prediction of thermal conductivity is also includes the Mg/S ratio, undercooling and oxygen activity. The detailed parameters are listed in Table 4.20 and the model was found as

$$\lambda = 22.50 + 1.496 \text{ Mg/S} + 0.45 \Delta T + 27.37 \underline{Q} \quad (4.2)$$

where  $\lambda$  is thermal conductivity (W/m K), Mg/S is the magnesium to sulfur ratio,  $\Delta T$

is undercooling (in  $^{\circ}\text{K}$ ) and  $\underline{Q}$  is oxygen activity (in ppm). Table 4.20 displays the predicted thermal conductivity obtained from the estimated parameters. From tables 4.19 and 4.20 we observed that, the intercept is 22.50. This means the thermal analysis when all the independent variables are equal to zero. Multiple R is 0.87 which means that there is also a good linear fitting between the thermal conductivity and its variables.

Table 4.19 Linear regression parameters estimated for thermal conductivity

	Coefficients
Intercept	22.50
Mg/S ratio	1.496
$\Delta T$ Undercooling	0.45
Oxygen activity)	27.73

Table 4.20 The predicted thermal conductivity obtained from the estimated parameters.

Observation	Predicted thermal conductivity (W/m.k)
1	37.00398
2	35.27908
3	39.87477
4	38.1749
5	38.10046
6	38.6768

## **CHAPTER 5**

### **CONCLUSIONS AND SCOPE OF FUTURE WORK**

#### **5.1 CONCLUSIONS**

In this study FeMgSiCe mish metal and FeMgSi were used to produce compacted graphite cast iron with different Mg/S ratio. A plunger treatment technique was implemented and the effect of section sensitivity on graphite morphology of vermicular/ compacted graphite cast iron was investigated.

Based upon experimental results and discussions of the production of compacted graphite iron process it could be concluded that, this process has narrow processing windows and its very sensitive to Mg/S ratio, section sensitivity or cooling rate, undercooling, oxygen activity and treatment time. Therefore, the following points are concluded

1. Lower ratio of Mg/S results in producing flake graphite and higher ratio results in ductile iron. The ratio of Mg/S required to produce compacted graphite iron is in between that ratio of flake graphite and ductile iron. In this study, this ratio was 3 to 5.30 considering the other variables such as treatment reaction and oxygen activity.

2. Graphite morphology is not much affected by section sensitivity at section higher than 1 cm, therefore to produce compacted graphite iron in thin sections like exhaust manifolds thickness (1 cm) it is not better to use compactizing alloys such as FeSiMg or FeSiMg-Cermish metal, however, FeSiMg; or FeSiMg Cermish metal could be successfully used to produce compacted graphite irons for heavy and medium section.

3. A strong correlation exists between the graphite morphology and the cooling curves. This relationship can be summarized as follows:

- a). When  $\Delta T$  is equal to  $+16^{\circ}\text{C}$ , ductile irons can be produce
- b). When  $\Delta T$  is negative, the flake iron is expected
- c). The values of  $\Delta T$  to produce compacted graphite iron are in between those which are required for ductile iron and flake iron. The range of these values is in between  $+4.4^{\circ}\text{C}$  and  $+7.9^{\circ}\text{C}$

4. The tensile strength property of compacted graphite iron produced either by using FeSiMg or FeSiMg-Cermish metal might be reported as intermediate between the tensile strength of ductile iron and flake iron. Nevertheless, this property could be controlled not only by the graphite morphology but also by alloying element.

5. It was found that the oxygen activity in the solidifying melt is critical to the formation of compacted graphite. This hypothesis is supported by measuring the oxygen activity of the molten iron and investigating the graphite morphology of the solidified iron. Higher value of oxygen activity produces flake graphite. On the

other hand, lower values of oxygen activity produce ductile iron. Compacted graphite forms at intermediate levels of oxygen activity. The range of this level of oxygen activity is from 0.203 ppm to 0.0203 ppm. Moreover; oxygen activity level necessary to produce compacted irons is very critical and is difficult to be controlled.

6. Due to the fact that both electrical and thermal conductivity are material characteristics and are directly proportional to each other. Measuring the resistivity at high temperatures can give clues about the thermal conductivity at those temperatures. It was observed that increasing the temperatures results in decreasing thermal conductivity and that's due to the graphite separation and formation of cracks in the graphite phase. These statements are in agreement with the results of other researches considering the effect of temperatures on the properties of compacted graphite irons.

7. From the application of multi regression, two models 4.1 and 4.2 were built to represent the relation between the facture strength and the thermal conductivity with the Mg/S ratio, undercooling and oxygen activity which are the most important variable affecting the production of compacted graphite irons. It could be concluded that, these models are good agreement with the relation ship between the tensile strength and thermal conductivity with 99% and 87% respectively.

## **5.2 SCOPE OF THE FUTURE WORK**

1. In all heats which were performed in this study, the compacted graphite iron

was only dominated in the medium and large section thickness, therefore, producing compacted graphite iron in small section thickness is needed to be considered in any further development of the treatment material required to produce compacted graphite iron.

2. The cooling curve features to produce compacted graphite iron, such as undercooling and recalescence, by using treatment material other than FeSiMgCe mish metal and FeSiMg should be considered. In addition the other feature of the casting production process such as oxygen activity should also be investigated.

3. In this work, the behavior of thermal conductivity was investigated at elevated temperatures; and the tensile strength was examined at room temperature, however, due to the increasing demand of compacted graphite material in different region through out the world, the behavior of thermal conductivity and the fracture strength at other temperatures should also be studied.



## REFERENCES

1. R. Elliott. "Cast Iron Technology", Butterworths & Co. Ltd., London, (1988): pp. 20-22.
2. H. H. Cornell and C. R. Loper Jr. AFS Trans., 93, (1985): pp. 435-442.
3. R. W. Monroe and C. E. Bates, in "Foundry Technology: Source Book". P. K. Mikelonis, Ed. American Society for Metals, Materials Park, OH, (1982): pp. 268-291.
4. A. A. Nofal. S. Parent-Simonin and A. S. Rezk, Fonderie-Fondeur d'Aujourd'hui, 83, (1989): pp. 14-24.
5. M. D. Chaudhari. R. W. Heine and C. R. Loper Jr. AFS Trans. 82, (1974): pp. 379-386.
6. E. F. Ryntz. and J. F. Janovvak. AFS Trans.. 78, (1970): pp. 141-144.
7. L. I. Levi. G. I. Kletskin. N. L. Sobol and Y. A. Kitaev, Russian Casting Production. (1). (1970): pp. 59-61.
8. J. Humphreys. B.C.I.R.A. Journal. 9. (1961): pp. 609-621.
9. W. Hartung. Giesserei. 57 (24). (1970): pp. 753-756.
10. J van Eegham. G. Devos. J. Plessers and O. Cure. AFS International Cast Metals J. 2 (2). (1977): pp. 57-63.

11. H. Ohlmes. *Giesserei*. 63 (25), (1976): pp. 714-718.
12. M. Booth. *The British Foundryman*, 76 (3). (1983): pp. 35-45.
13. R. W. Heine, C. R. Loper and P. C. Rosenthal, *Principles of Metal Casting*," McGraw-Hill Book Company, New York, New York, 1967.
14. P. F. Weiser, E. C. Bates and J. F. Wallace, *Mechanism of Graphite Formation in Iron-Silicon-Carbon Alloys*, Malleable Founder's Society, Cleveland, Ohio, 1967.
15. J. F. Wallace, "Effects of Minor Elements on the Structure of Cast Irons," *AFS Transactions*, Volume 83, 1975, pp. 363
16. *Iron Castings Handbook*, Iron Castings Society, Inc., Cleveland, Ohio, 1981.
17. J. V. Dawson and E. R. Evans, "Compacted Graphite Irons Produced by Magnesium Additions," *BCIRA Journal of Research and Development*, Volume 22, March, 1974, pp. 136-144.
18. D. D. Double and A. Hellawell, "Growth Structure of Various Forms of Graphite," *The Metallurgy of Cast Iron*, Georgi Publishing Co., St. Saphorin, Switzerland, 1975, pp. 509-537.
19. N. Tsutsumi and M. Imamura, "Proposal of the Classification of Spheroidal Graphite Form in Spheroidal Graphite Cast Iron," *Report of the Casting Research Laboratory, Waseda University*, No. 29, November, 1978, pp. 15-23.
20. P. C. Liu and C. R. Loper, "Scanning Electron Microscope Study of the Graphite Morphology in Cast Iron," *Scanning Electron Microscopy*, 1980, pp. 407-418.
21. L. Sofroni, I. Riposan and I. Chira, "Some Considerations on the Crystallization Features of Cast Irons with Intermediary-Shaped Graphite (Vermicular Type)," *The Metallurgy of Cast Iron*, Georgi Publishing Co., St. Saphorin, Switzerland, 1975, pp.

179-195.

22. A. L. Norbury and E. Morgan, "Effect of Melting Conditions on the Microstructure and Mechanical Strengths of Gray Cast Iron Containing Various Amounts of Carbon and Silicon," *Journal of the Iron and Steel Institute*, Volume 121, 1930, pp. 367.

23. A. L. Norbury and E. Morgan, "Effect of Non-Metallic Inclusions on the Graphite in Cast Iron," *Journal of the Iron and Steel Institute*, Volume 134, 1936.

24. W. C. Filkins, et. al, "Gray Iron Inoculation and Inoculants Evaluation," *AFS Transactions*, Volume 70, 1962, p. 893.

25. S. C. Massari and R. W. Lindsey, "Some Factors Influencing the Graphitizing Behaviour of Cast Iron," *AFS Transactions*, Volume 49, 1941.

26. K. M. Muzumdar and J. F. Wallace, "Effect of Sulfur in Cast Iron," *AFS Transactions*, Volume 81, 1973, pp. 412-423.

27. K. M. Muzumdar and J. F. Wallace, "Inoculation-Sulfur Relationship of Cast Iron," *AFS Transactions*, Volume 80, 1972, pp. 317-328.

28. H. Morrogh and W. Williams, "Graphite Formation in Cast Irons," *Journal of the Iron and Steel Institute*, Volume 155, 1974, p. 322.

29. C. R. Loper and N. Takizawa, "Spheroidal Graphite Development in White Cast Irons," *AFS Transactions*, Volume 72, 1964, p. 520.

30. F. B. Rote, E. F. Chajnowski and J. T. Bryce, "Malleable Base Spheroidal Iron," *AFS Transactions*, Volume 64, 1956, p. 197.

31. B. Lux and M. Granges, "The Spatial Structure of Graphite in Pure Fe-C-Si Alloys," *Praktische Metallographic*, Volume 5, 1968, p. 123.

32. J. D. Schobel, "Precipitation of Graphite During the Solidification of Nodular Cast Iron," Recent Research on Cast Iron, Gordon and Breach Publishers, New York, New York, 1968, p. 303.
33. B. Lux, "On the Theory of Nodular Graphite Formation in Cast Iron, Parts I and II," AFS Cast Metals Research Journal, Volume 8, Nos. 1 and 2, March and June, 1972, pp. 25-38 and pp. 49-65.
34. W. Oldfield, "Solidification of Hypoeutectic Gray Cast Irons," BCIRA Journal of Research and Development, Volume 8, 1960, p. 177.
35. E. Scheil and J. D. Schobel, "On the Location of Spheroidal Graphite in Solidified Cast Iron," Giesserei-Techn. Wiss Beih., Volume 13, 1961, p. 203.
36. W. Oldfield, "The Origin of Graphite During Solidification of Cast Iron," Recent Research on Cast Iron, Gordon and Breach Publishers, New York, 1968, p. 281.
37. I. Minkoff and B. Lux, "Graphite Growth from Metallic Solutions," The Metallurgy of Cast Iron, Georgi Publishing Co., St. Saphorin, Switzerland, 1975, p. 473.
38. S. V. Subramanian et al., "Graphite Morphology Control in Cast Iron," Iron and Steel Magazine, March, 1980, pp. 18-25.
39. B. Lux, I. Minkoff, F. Mollard and E. Thury, "Branching of Graphite Crystals Growing from a Metallic Solution," The Metallurgy of Cast Iron, Georgi Publishing Co., St. Saphorin, Switzerland, 1975, pp. 495-508.
40. B. Lux, "Nucleation of Eutectic Graphite in Inoculated Gray Iron by Salt-Like Carbides," Modern Castings, Volume 45, May, 1964, p. 222.
41. G. F. Ruff and J. F. Wallace, "Graphite Configuration in Gray Iron," AFS

Transactions, Volume 85, 1977, pp. 167-170.

42. J. F. Wallace, "Influence of Minor Elements Including Sulfur on the Morphology of Cast Irons," The Metallurgy of Cast Iron, Georgi Publishing Co., St. Saphorin, Switzerland, 1975, pp. 583-602.

43. H.D. Merchant and J. F. Wallace, "Solidification of Gray Iron," AFS Transactions, Volume 69, 1961, pp. 249-258.

44. C. E. Bates and J. F. Wallace, "Effects and Neutralization of Trace Elements in Gray and Ductile Iron," AFS Transactions, Volume 75, 1967, pp. 815-838.

45. C. R. Loper, R. W. Heine and M. D. Chaudhari, "Thermal Analysis for Structure Control," The Metallurgy of Cast Iron, Georgi Publishing Co., St. Saphorin, Switzerland, 1975, pp. 639-657.

46. H. Fredriksson and S. E. Wetterfall, "A Study of Transition From Undercooled to Flake Graphite in Cast Iron," The Metallurgy of Cast Iron, Georgi Publishing Co., St. Saphorin, Switzerland, 1975, pp. 277-293.

47. W. C. Johnson and H. B. Smartt, "The Role of Interphase Boundary Adsorption on the Formation of Spheroidal Graphite in Cast Iron," Metallurgical Transactions, Volume 8A, 1977, p. 553.

48. J. Kevarian, H. F. Taylor and J. Wulff, "Experiments on Spherulitic Formations in Cast Iron," American Foundryman, Volume 23, 1953, pp. 85-91.

49. B. Lux and H. Tannenburger, "Inoculation Effect on Graphite Formation in Pure Fe-C and Fe-C-Si," Modern Castings, Volume 41, March, 1962, p. 57.

50. B. Dhindaw and J. D. Verhoven, "Nodular Graphite Formation in Vacuum Melted High Purity Fe-C-Si Alloys," Metallurgical Transactions, Volume 11A,

June, 1980, pp. 1049-1057.

51. J. P. Sachoda and J. E. Gruzleski, "The Mechanism of Graphite Spheroid Formation in Pure Fe-C-Si Alloys," The Metallurgy of Cast Iron, Georgi Publishing Co., St. Saphonn, Switzerland, 1975, pp. 443-459.
52. W. Oldfield, G. T. Gerring and W. A. Tiller, "Solidification of Spheroidal and Flake Graphite Cast Iron," Joint Conference on the Solidification of Metals, Paper No. B/III/16, ISI Publication 110, 1968, p. 256.
53. B. Lux, F. Mollard and I. Minkoff, "Austenite Envelopes Around Graphite," The Metallurgy of Cast Iron, Georgi Publishing Co., St. Saphorin, Switzerland, 1975, p. 371.
54. P. K. Basutkar, C. R. Loper and C. L. Babu, "Solidification of Heavy Section Ductile Iron Castings," AFS Transactions, Volume 78, 1970, pp. 429-434.
55. R. K. Buhr, "Vermicular Graphite Formation in Cast Iron," Modern Castings, Volume 54, No. 6, December, 1968, pp. 497-503.
56. C. R. Loper and R. W. Heine, "Solidification of Cast Iron with Spheroidal Graphite," ASM Transactions, Volume 56, 1963, pp. 135-152.
57. R. W. Rusman and C. R. Loper, "Heavy Section Ductile Iron as Affected by Certain Processing Variables," AFS Transactions, Volume 75, 1967, pp. 1-9.
58. R. Barton, "Magnesium Content Required to Produce Nodular Graphite Structures Using Base Irons Desulphurized by Various Techniques," BCIRA Journal of Research and Development, Volume 11, 1963, p. 741.
59. H. H. Cornell and C. R. Loper, "Rare-Earth Additions to Blast Furnace Iron for the Production of Large Castings," ASTM Symposium on Ferroalloys, Master Alloys and Other Liquid Metal Additives, May 20-21, 1980, Denver, Colorado.

60. H. Morrogh, "Production of Nodular Graphite Structures in Gray Cast Irons," AFS Transactions, Volume 57, 1949, pp. 72-90.
61. J. V. Dawson, L. Smith and B. Bach, "Some Effects of Nitrogen in Cast Iron," BCIRA Journal of Research and Development, Volume 4, June, 1953, pp. 540-552.
62. F. A. Mountford, "The Influence of Nitrogen on the Strength, Hardness and Structure of Gray Cast Iron," The British Foundryman, Volume 59, April, 1966, p. 141.
63. I. C. H. Hughes, "The Role of Gases in the Structure of Cast Iron," AFS Transactions, Volume 77, 1969, pp. 121-133.
64. L. Bacherud, K. Nilsson and H. Steen, "Study of Nucleation and Growth of Graphite in Magnesium- Treated Cast Iron by Means of Thermal analysis," The Metallurgy of Cast Iron, Georgi Publishing Co., St. Saphorin, Switzerland, 1975, pp. 625-637.
65. P. C. Liu, C. R. Loper, F. Kimura and E. N. Pan, "Observations on the Graphite Morphology of Compacted Graphite Cast Iron," AFS Transactions, Volume 89, 1981, pp. 65-78.
66. B. Luck, Discussion of paper by D. D. Double and A. Hellowell, "Growth Structures of Various Forms of Graphite," The Metallurgy of Cast Iron, Georgi Publishing Co., St. Saphorin, Switzerland, 1975, pp. 527-528.
67. J. Y. Su, C. T. Chow and J. F. Wallace, "Solidification Behavior of Compacted Graphite," To Be Presented at the 1982 AFS Congress.
68. W.C.Johnson and H. B. Smartt, "Confirmation of Impurity Adsorption at Flake-Iron Interfaces in Gray Iron," Scripta-Metallurgia, Volume 9, 1975, pp. 1205-1210.
69. W. C. Johnson, B. V. Kovacs and J. A. Clum, "Interfacial Chemistry in Modified

Nodular Iron, "Scripta-Metallurgia, Volume 8, 1974, pp. 1309- 1316.

70. H. Morrogh, "Influence of Some Residual Elements and Their Neutralization in Magnesium-Treated Nodular Cast Iron," AFS Transactions, Volume 60, 1952, pp. 439-452.

71. R. D. Schellung, "Effect of Certain Elements on the Form of Graphite in Cast Iron," AFS Cast Metals Research Journal, March, 1967, pp. 30-38.

72. M. J. Lalich, "The Influence of Rare-Earth Elements on Magnesium-Treated Ductile Cast Irons," The Metallurgy of Cast Iron, Georgi Publishing Co., St. Saphorin, Switzerland, 1975, pp. 561-581.

73. T. Carlberg and H. Fredriksson, "Influence of Silicon and Aluminum on the Solidification of Cast Iron," Proceedings of the International Conference on the Solidification and Casting of Metals^ Sheffield, England, July, 1977, pp. 115-123.

74. A. Munitz and I. Minkoff, "Instability of Graphite Crystal Growth in Metallic Systems," Proceedings of the International Conference on the Solidification and Casting of Metals, Sheffield, England, July, 1977, 70-73.

75. R. D. Maier and J. F. Wallace, "Literature Search on Controlling the Shape of Temper Carbon Nodules in Malleable Iron," AFS Transactions, Volume 84, 1976, p. 687.

76. H. D. Merchant, "Solidification of Cast Iron: A Review of the Literature," Recent Research on Cast Iron, Gordon and Breach, New York, New York, 1968, p. 1.

77. J. Kevarian and H. Taylor, "Effects of Gaseous and Solid Addition Elements on Surface Tension and Contact Angle (on Graphite) of Various Iron-Carbon Alloys," AFS Transactions, Volume 75, 1957, p. 212.



78. K. Hurfurth, "Investigations into the Influence of Various Additions on the Surface Tension of Cast Iron with the Aim of Finding Relationships Between Surface Tension and the Occurrence of Various Forms of Graphite," *Freiberger Forschungsh*, Volume 105B, 1967, p. 267.
79. R. H. McSwain and C. E. Bates, "Surface and Interfacial Relationships Controlling Graphite Formation in Cast Iron," *The Metallurgy of Cast Iron*, Georgi Publishing Co., St. Saphorin, Switzerland, 1957, p. 423.
80. E. Selcuk, "Solidification of Cast Irons with Spherulitic Graphite," *The Metallurgy of Cast Iron*, Georgi Publishing Co., St. Saphorin, Switzerland, 1975, p. 409.
81. J. C. Sawyer and J. F. Wallace, "Effect of Surface Energy on Graphite Forms in Gray and Ductile Irons," *AFS Cast Metals Research Journal*, Volume 5, No. 2, 1969, p. 83.
82. H. Geilenberg, "A Critical Review of the Crystallization of Graphite From Metallic Solution After the Surface Tension Theory," *Recent Research on Cast Iron*, Gordon and Breach, New York, New York, 1968.
83. G. F. Van Rooyen, "Conditions Necessary for the Nodular Crystallization of Graphite in Cast Iron," *FWP Journal*, April, 1977, p. 7.
84. K. Lohberg and W. Wunder, "Surface Tension of Near Eutectic Iron-Carbon Alloys with and without Magnesium and Additions of Bismuth, Lead, Copper, Titanium and Zirconium and Its Importance for the Formation of Spheroidal Graphite," *Giesserei Techn. Wiss. Beih*, Volume 18, 1966, p. 189.
85. W. Ballroan and B. Lux, "Grain Boundaries in Graphite," *The Metallurgy of Cast Iron*, Georgi Publishing Co., St. Saphorin, Switzerland, 1975, p. 461.
86. I. Minkoff, "Factors Affecting Growth of Spheroidal Graphite," *Modern*

Castings, Volume 41, 1962, p. 18.

87. R. A. Sidorenko, "Dislocation Mechanism of the Growth of Spheroidal Graphite in Iron," *Physics of Metals and Metallography*, Volume 20, 1965, p. 93.

88. F. C. Frank, "Introductory Lecture," *Growth and Perfection of Crystals*, John Wiley and Sons, Inc., New York, New York, 1958, p. 3.

89. H. E. Buckley, *Crystal Growth*, John Wiley and Sons, Inc., New York, New York, 1951.

90. J. W. Cahn, W. B. Hillig and G. W. Sears, "Molecular Mechanisms of Solidification," *Acta Metallurgica*, Volume 12, 1964, p. 1421.

91. N. Cabrera and D. A. Vermilyea, "The Growth of Crystals from Solutions," *Growth and Perfection of Crystals*, R. H. Doremus, B. W. Roberts and D. Turnbull, eds., John Wiley and Sons, Inc., 1958, p. 393.

92. R. LaRaann and I. N. Stranski, "The Effect of Adsorption of Impurities on the Equilibrium and Growth Forms of Crystals," *Growth and Perfection of Crystals*, R. H. Doremus, B. W. Roberts and D. Turnbull, eds., John Wiley and Sons, Inc., 1958, p.427.

93. G. W. Sears, "The Effect of Poisons on Crystal Growth," *Growth and Perfection of Crystals*, R. H. Doremus, B. w. Roberts and D. Turnbull, eds., John Wiley and Sons, Inc., 1958, p. 441.

94. A. A. Chernov, "Theory of Non-Equilibrium Capture of Impurities During Growth of Crystals," *Soviet Physics Doklady*, Volume 5, 1960, p. 470.

95. A. A. Chernov, "The Rate of Spiral Layer Growth of Crystals From Solution and the Molten State," *Soviet Physics Doklady*, Volume 5, 1960, p. 654.

96. A. A. Chernov, "The Spiral Growth of Crystals," Soviet Physics Uspekhi, Volume 4, 1961, p. 116.
97. A. A. Chernov, "Theory of Stability of Face Forms in Crystals," Soviet Physics Crystallography, Volume 16, 1972, p. 734.
98. K.P.Cooper," The Production of Compacted Graphite Cast Iron and the Evaluation of Some of its Properties." M.S thesis, Univ. Of Wisconsin, 1977.
99. G.E. Dieter, "Mechanical Metallurgy" 2nd Edition, Mcgraw-Hill Book Co. 1961.
100. James P. Hrusovsky," Formation, Production and Properties of Compacted Graphite Iron, Ph.D. Thesis, Case Western Reserve University, 1982
101. M.Ali AKBAŞ,"Effect of Ni and Ti Substitution on the Superconducting Properties of YBa<sub>2</sub>Cu<sub>3</sub>O<sub>7-x</sub> System." M.S thesis, METU. , 1991.
102. R.Hummer and A.Buhrig," Development of New sensor for Oxygen Activity Measurements in Cast Iron" Special Issue, Austrian Foundry Institute
103. Oscar Marcelo Suarez,"Thermal Analysis and Microstructure Control of Cast Iron ", Ph.D. Thesis, University of Wisconsin Madison, 2000
104. Gürolhan Yaşar,"Compacted / Vermicular Graphite Production Techniques and The section Sensitivity of Compacted /Vermicular Graphite." M.S thesis, METU. , 1996
105. James P. Hrusovsky," Factors Effecting Graphite Morphology , Matrix Structures and tensile properties of Compacted Graphite Cast Iron, Ph.D. Thesis, Case Western Reserve University, 1982
106. Angus, H. T. Cast Iron: Physical and Engineering Properties. BCIRA, p. 126-134, 1960

107. "Thermal Conductivity of Unalloyed Cast Iron", BCIRA Broadsheet 203, 1981.
108. Gusseisen mit Lamellengraphit – Eigenschaften und Anwendung. Konstruieren + Giessen, Zentrale für Gussverwendung. VDI-Verlag, Düsseldorf, 2000.
109. STEFANESCU, D., "Physical Properties of Cast Iron", In: GOODRICH, G.M., Iron Casting Engineering Handbook, AFS, 2003
110. Gusseisen mit Kugelgraphit, Konstruieren + Giessen. Zentrale für Gussverwendung, VDI-Verlag, Düsseldorf, 1988.
111. E.J.Kubick et al, AFS Trans., 105,(1997):pp.579-586
112. Oscar M. Suarez," Thermal Analysis and Microstructure Control of Cast Iron, Ph.D. Thesis, Wisconsin-Madison University, 2000

## **VITAE**

Mr. Omar Elmabrouk was born in Benghazi – Libya on July 12, 1968. He received his B.Sc. degree in fall 1991 in Industrial Engineering from Garyounis University, Benghazi, Libya. He worked as a maintenance planning engineer in General Electrical Company of Libya from 1993 to 2001.

In spring 2001, he received his M.Sc. from Garyounis University, Benghazi, Libya in Manufacture Engineering, since then he has been a lecturer in the Industrial Engineering Department of Garyounis.

He received a scholarship from his university to study for PhD at METU in Turkey; he has joined his PhD. program in Metallurgy and Materials Engineering Department of the Middle East Technical University in spring 2003-2004.

He published three articles in local conferences in the field of maintenance planning and one article in international conference in the field of metal casting. His main areas of research interest are Production Scheduling, Casting Process, and Metal Cutting.